



UNIVERSITÀ DEGLI STUDI DELL'AQUILA
DEPARTMENT OF PHYSICAL AND CHEMICAL SCIENCES

PhD in Physical and Chemical Sciences

XXXVI cycle

**Lipid-Based Systems: Multifunctional Platforms for Biomedical and
Environmental Applications**

SSD: CHIM/06

PhD Candidate

Elena Allegritti

PhD Program Coordinator

Prof. Massimiliano Aschi

Tutor

Prof. Luisa Giansanti

2022/2023

Abstract

Lipid-based systems have emerged as versatile platforms with remarkable advantages for a broad spectrum of applications in both biomedical and environmental fields.

In biomedical applications, lipid-based systems, including liposomes and lipid mesophases, offer exceptional biocompatibility and biodegradability, making them ideal candidates for drug delivery systems. Their ability to encapsulate a different range of therapeutic agents, including hydrophobic and hydrophilic compounds, facilitates targeted drug delivery, improving therapeutic efficacy while minimizing systemic side effects. Moreover, the lipid-based carriers can be engineered to respond to specific stimuli, enabling controlled release and personalized medicine approaches.

Lipid-based materials exhibit a low environmental impact, aligning with sustainable practices in the environmental field. They are mostly used for delivering remediation agents to contaminated sites, and enhancing the wool and cotton dyeing process.

Over the course of these three years, my focus has been on four main topics: the use of liposomes for the delivery of hydrophilic molecules (levodopa and vancomycin); the development of lipid mesophase-based beads as an innovative platform for sustained release of hydrophilic and hydrophobic molecules; the application of magnetoliposomes for the treatment of polluted textile wastewater; and the application of liposomes in enhancing the wool dyeing process. In each of the five projects, the relationship between the components of the lipid-based formulations and the results obtained was studied to understand which parameters are crucial for the success of the formulations.

In the encapsulation of levodopa within liposomes, four different synthetic surfactants were incorporated into the phospholipid bilayer at two distinct molar ratios. Liposomes intended for effective drug delivery and interaction with cells or biological membranes generally require a positive charge. The selected

surfactants possess either a quaternary ammonium group or a *N*-oxide group, resulting in liposomes with a positively charged surface. All prepared formulations underwent characterization in terms of dimensions, surface charge, morphology, stability, entrapment efficiency, and thermotropic properties. Additionally, their potential for intranasal application was assessed using porcine nasal mucosa. Our results indicated that the combination of the surface charge of the bilayer and lipid bilayer packaging—both influenced by the molecular structure of the surfactant included in the formulation—affected the crossing of the nasal mucosa. A similar study was conducted focusing on encapsulating vancomycin within liposomes. In this case, a positively charged lipid and/or a cholesterol derivative containing a pH-sensitive moiety were incorporated into the lipid bilayer. Following the investigation of the formulations' dimensions, morphology, and thermotropic properties, they were evaluated against both Gram-positive and Gram-negative bacteria. Our findings revealed that the phospholipid alone did not interact with bacterial cells. Instead, the presence of the cationic lipid and the pH-sensitive cholesterol was necessary for the liposomes to exhibit effectiveness against *Staphylococcus aureus*.

Lipid mesophases (LMPs) as a biocompatible and biodegradable material for sustained drug delivery were explored. The hypothesis of this project revolves around leveraging the high surface-to-volume ratio of LMP-based beads to enhance strength, stability, and surface interaction compared to LMP bulk gel. Additionally, the dosage of drugs loaded into the beads is expected to be more easily and rapidly achieved compared to the viscous bulk gel, resulting in effective patient-centric formulations. The beads, in fact, exhibited remarkable uniformity in terms of size and entrapment efficiency. To modulate drug release, antioxidant vitamin E was introduced into the beads, influencing mesophase topologies and controlling drug diffusion coefficients. Four drugs (tofacitinib citrate, bupivacaine, rapamycin and gefitinib) with distinct chemical properties intended for three different pathologies and administration routes were successfully loaded into the

beads, achieving a drug entrapment efficiency exceeding 80%. Importantly, sustained drug release was observed regardless of the drugs' chemical properties, leading to the development of an injectable formulation. This injectable formulation allows for direct administration into the target site, minimizing systemic exposure and thereby reducing adverse effects. The approach presented in this study demonstrates the potential of LMP-based beads for tailored drug delivery systems with broad applications across diverse therapeutic scenarios.

For the first time, then, magnetic core-shell liposomes (ML, nanocomposites comprising lipid bilayers that incorporate magnetic nanoparticles) were used in wastewater remediation: the lipid bilayer create an environment where organic pollutants preferentially partition instead of water, and the manipulation of MLs with an external magnet enables an easy recovery from water. This study aimed to assess the system's potential for water remediation, focusing on MLs ability to remove common pollutants in industrial wastewater. Specifically, alkylphenol ethoxylates (APEOs) were used as the archetype for organic pollutants. Superparamagnetic magnetite nanoparticles and various MLs formulations (neutral, cationic, anionic, asymmetric or not) were prepared using two different methodologies and extensively characterized from a physico-chemical point of view (dimension, morphology, structural composition, magnetic properties, surface area, thermal stability). The nature of their interaction between magnetite nanoparticles and lipids was also investigated through theoretical calculations. Finally, MLs ability in APEO removal was evaluated, as well as the recyclability of the system. MLs demonstrated effectiveness in APEOs removal, with neutral ML exhibiting the highest results (>80%). This study highlights that the structural composition of the magnetic nanoparticles did not affect the coating process. Instead, it emphasizes that the surface charge of MLs is the most crucial parameter for the removal of pollutants from aqueous media.

In the last project various liposome formulations as a means to enhance the sustainability of wool dyeing processes were explored. Specifically, we aimed to

reduce the quantity of dye required for textile processing by half. To evaluate our approach, we compared the color of fabrics dyed by the textile industry with those dyed in our experiment, where liposomes were present alongside only half the usual amount of dye. In this project, we incorporated cationic, anionic, and/or cholesterol in various molar ratios within the phospholipid bilayer to investigate the potential influence of surface charge and fluidity of the lipid bilayer on the dyeing process. Incorporating both red and blue dyes into the characterized liposome formulations allowed us to assess their effectiveness in the dyeing process. Our findings revealed that the red dye-loaded liposomes did not yield satisfactory results. However, the most promising outcomes in terms of fabric coloration were observed with anionic liposomes containing the blue dye. Remarkably, in one instance, we observed no discernible colorimetric differences between the fabric dyed in our laboratory and that dyed by the industry. Under no circumstances did the use of liposomes lead to a complete exhaustion of the dyeing bath. Consequently, MLs were tested to eliminate the remaining dyes from the water environment. These subsequent experiments with MLs reaffirmed the importance of surface charge in influencing pollutant removal: given that both dyes carry a negative charge, only the cationic MLs yielded satisfactory results in terms of dye removal from water.

Summary

Chapter 1: Self-Assembly: from Surfactants to Lipid Nanoparticles.....	1
Chapter 2: Drug Delivery Systems: An Overview.....	21
Chapter 3: Environmental Concerns in Textile Industry.....	31
Chapter 4: Techniques for Comprehensive Characterization.....	48
Chapter 5: Aim of the Work.....	72
Chapter 6: Liposomes as DDSs for Levodopa.....	73
Chapter 7: Liposomes as DDSs for Vancomycin.....	97
Chapter 8: Lipid Mesophases as DDSs.....	116
Chapter 9: Magnetoliposomes for Water Remediation.....	140
Chapter 10: Liposomes in the Process of Wool Dyeing.....	174
Chapter 11: General Conclusion.....	193
Chapter 12: Experimental Procedures.....	194

Chapter 1. Self-Assembly: from Surfactants to Lipid Nanoparticles

1. Self-Assembly of Surfactants

Surfactants, short for surface active agents,¹ constitute an interesting class of molecules with unique structural features and play a crucial role in various chemical and biological systems. They possess a distinctive amphiphilic molecular structure, made up of a hydrophilic headgroup and a hydrophobic tail. They could also exhibit two hydrocarbon chains attached to a polar head (twin surfactants), two hydrophobic tails and two hydrophilic groups (gemini surfactants) linked together or two headgroups joined by a hydrophobic spacer (bolaform surfactants),^{1,2} as depicted in Figure 1.

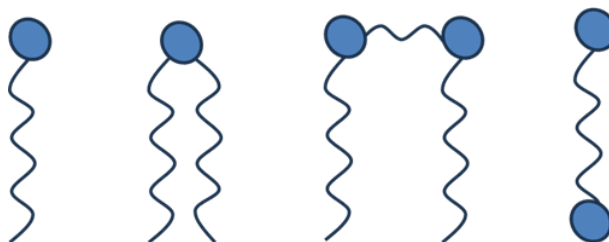


Figure 1. Single tailed, twin, gemini, and bola-form surfactants, respectively.

There are numerous possibilities for variations in the headgroup and tail components: the polar head can be nonionic, cationic, anionic, or zwitterionic. It could be small and compact, bulky or an oligomeric chain. Also the hydrophobic hydrocarbon chain can be differently functionalized and may include straight, branched or ring structures, either saturated or unsaturated.²

Self-assembly is the term used to describe the spontaneous arrangement of molecules into three-dimensional structured and orderly patterns in response to the chemical and physical properties of the solution without the need for external intervention or control.³ It occurs due to the intrinsic properties and interactions of the components, often driven by thermodynamic (minimizing energy, achieving

stability, or reaching a state of thermodynamic equilibrium) and/or kinetic considerations and it is guided by intermolecular interactions, such as Van der Waals forces, hydrogen bonding, electrostatic and/or hydrophobic interactions.³ Studies on the self-assembly of surfactants in water have a long history, starting with the pioneering recognition of the existence of aggregates in soap solution by J. W. McBain in 1913, more than 100 years ago.^{4,5} He noticed that, despite a low osmotic activity, the soap solution had a relatively high conductivity that changed with the concentration. Both these observations led him to think that molecules formed aggregates within the solution. He coined the term micelles to describe them and suggested a lamellar morphology. The proposal of a spherical structure composed of approximately 50 surfactant molecules was made by G. S. Hartley, who suggested that the “aggregates are essentially liquid and since they will tend to present the minimum surface to the water, they will presumably be roughly spherical and of the largest radius consistent with none of the heads being submerged in the paraffin interior”.⁴ The key driving force behind micelles formation is the hydrophobic effect: the lipophilic tails tend to avoid unfavorable interactions with polar water, while the headgroups favorably interact with the solvent.⁶ Despite the weakness of the forces involved in amphiphiles self-assembly, the relevant number of these soft interactions will produce an overall effect that is strong enough to hold different amphiphile molecules together as well as to ensure their stability in solution.⁷

Between 1960 and 1970, C. Tanford pioneered one of the most important models that currently dominate our understanding of surfactant self-assembly focused on the thermodynamic aspects of aggregation of surfactants in water.⁸ According to his model, the formation of the equilibrium aggregates is the outcome of achieving a balance between the interfacial free energy at the micelles-water interface and the repulsive forces originating from the surfactant headgroups, which are also situated at the interface. Tanford also recognized the existence of a critical micelle

concentration (*cmc*): below this concentration, surfactant molecules are predominantly dispersed as individual molecules in solution while, above the *cmc*, the concentration of surfactant molecules exceeds the threshold required for micelle formation.^{4,8,9}

Tanford formulated a quantitative expression (where *K* is the Boltzmann constant and *T* is the temperature) for describing the standard free energy change on aggregation ($\Delta\mu_g^0$) invoking the concept of opposing forces.^{4,9}

$$(\Delta\mu_g^0 / KT) = (\Delta\mu_g^0 / KT)_{\text{tail}} + (\Delta\mu_g^0 / KT)_{\text{int}} + (\Delta\mu_g^0 / KT)_{\text{head}}$$

The first component represents a negative free energy contribution arising from the movement of the surfactant tail from its unfavorable interaction with water to the more favorable hydrocarbon-like environment within the aggregate core. This term is dependent on the surfactant tail but is independent on the aggregate's shape or size. The second element accounts for a positive contribution, addressing the residual contact between the surfactant tails and water at the interface of the aggregate core and water. This is expressed as the product of a contact free energy per unit area (denoted as σ) and the surface area per molecule of the aggregate core (denoted as *a*). The third factor introduces another positive free energy contribution which takes into consideration the repulsive interactions between the headgroups due to their crowding at the aggregate surface. These repulsions can result from steric interactions, relevant to any headgroup type, as well as electrostatic (dipolar or ionic) interactions. As the repulsion intensifies when the headgroups approach each other, Tanford introduced an expression for this free energy contribution, demonstrating an inverse dependence on *a*. Consequently, the proposed standard free energy change per molecule during aggregation, according to Tanford, takes the following form:

$$(\Delta\mu_g^0 / KT) = (\Delta\mu_g^0 / KT)_{\text{tail}} + (\sigma / KT)a + (\alpha / KT)a^{-1}$$

where α is the head group repulsion parameter. In this equation, the first contribution (the tail transfer free energy) is negative. Hence, this contribution is responsible for the aggregation to occur and it affects only the *cmc*. The second contribution (the free energy of residual contact between the aggregate core and water) is positive and decreases in magnitude as the area a decreases. Hence, this contribution promotes the growth of the aggregate. The third contribution (the free energy due to head group repulsions) is also positive and increases in magnitude if the area a decreases. Given that the repulsive forces intensify as the headgroups approach each other, this contribution is responsible for limiting the growth of aggregates to a finite size.

The Tanford model thus offers a clear explanation for the formation of the aggregates, their growth and the mechanism by which they reach a finite, stable size without continuous expansion. Anyway, it could not predict the morphology of self-assembled micelles.

A few years later, in 1976, J. Israelachvili and his colleagues introduced the concept of the critical packing parameter (C_{pp} , Figure 2): it helps predicting the aggregates that will form upon self-assembly of surfactant based on their molecular structure.^{10,11}

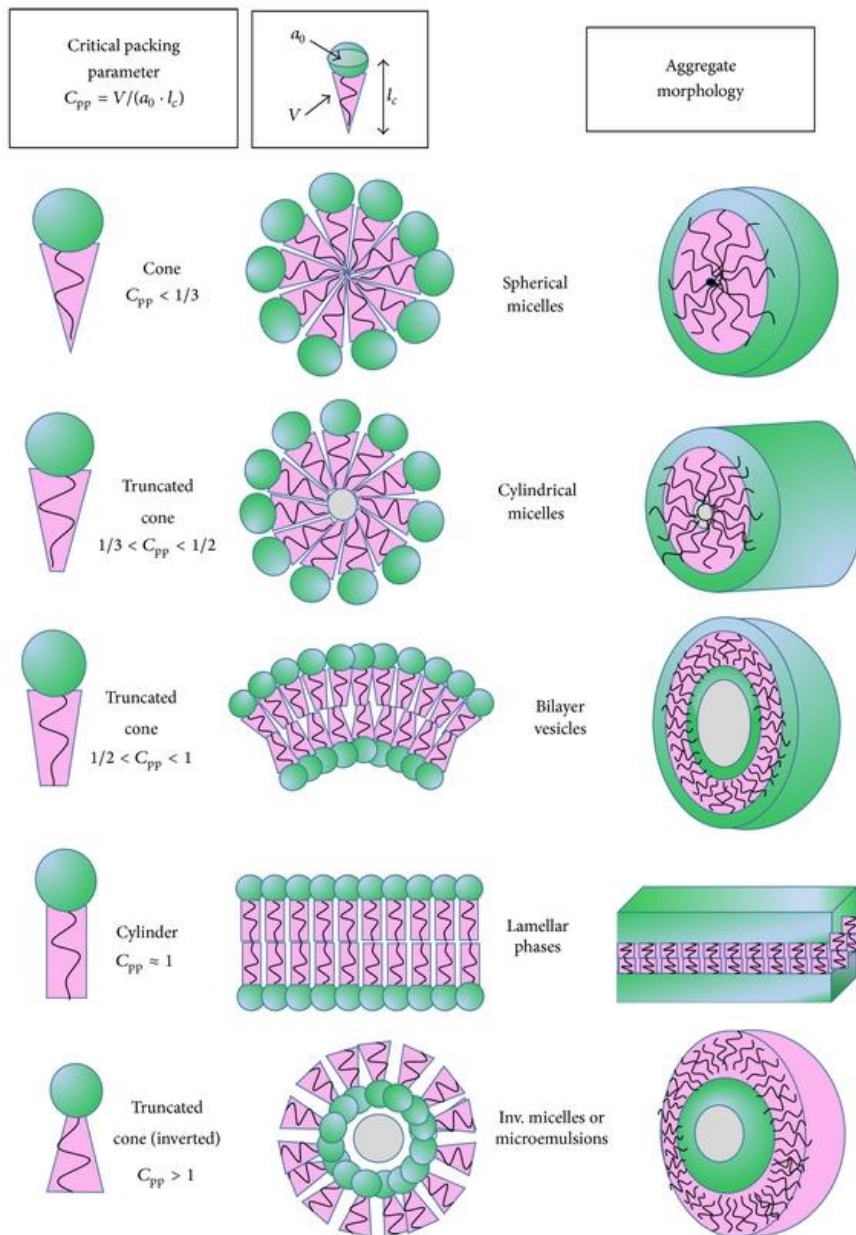


Figure 2. Critical packing parameter used for the prediction of the structure of surfactants self-assembly.

C_{pp} is defined as V_0/a^*L_0 , where V_0 and L_0 represent the volume and the length of the surfactant tail, respectively, and a^* is the area of the surfactant headgroup at the interface of the hydrophobic core-hydrophilic media. In general, when $C_{pp} < 1$, it is anticipated that "oil-in-water" morphologies will be present, indicating the existence of direct liquid crystalline phases where the polar headgroups create a convex interface with the aqueous phase. On the contrary, when $C_{pp} > 1$, a phase inversion takes place, leading to "water-in-oil" morphologies with lipid head surfaces curving toward the water phase. When $C_{pp} = 1$, flat interfaces are observed. More in details, when C_{pp} is less than $1/3$, surfactants tend to form spherical micelles (in this case, the hydrophilic headgroups are well hydrated and the hydrophobic tails are sequestered inside the micelle core). If C_{pp} is between $1/3$ and $1/2$, surfactants are more likely to form cylindrical or rod-like micelles, while if it exceeds $1/2$, surfactants may form lamellar or bilayer structures (the hydrophilic headgroups are well hydrated on both sides of the bilayer, and the hydrophobic tails are sandwiched between them).¹⁰⁻¹³

Temperature alterations are partially comprehensible: as temperature increases, hydrogen bonds are partially disrupted, affecting the hydration of water molecules around the polar heads of lipid molecules and ultimately increasing the parameter due to a reduction in the effective head area.

As indicated by C_{pp} , several forms of the aggregates are possible, depending on the relative dimensions of the polar head groups and non-polar tails of surfactants, as well as their concentration and the characteristics of the aqueous environment. Over the years, various structures beyond micelles, lamellar bilayers and liposomes have been discovered, including, cubic, hexagonal, or inversed micellar phases, and more. In particular, liposomes and lipid mesophases (the two lipid-based aggregates investigated in this thesis) are described below.

1.2 Liposomes

Liposomes (Figure 3A), spherical vesicles composed of one or more lipid bilayers that enclose an aqueous core,¹⁴ made their debut in the early 1960s, when A. D. Bangham and his team conducted pioneering research on phospholipids at the Babraham Institute in Cambridge, UK.^{15,16} In particular, they were investigating the behavior of lecithin and other components in water. When transmission electron microscopes became available, the high-resolution images they took showed that lipids form water-filled vesicles, resembling cells, which Bangham called liposomes (Figure 3B and 3C).^{17,18}

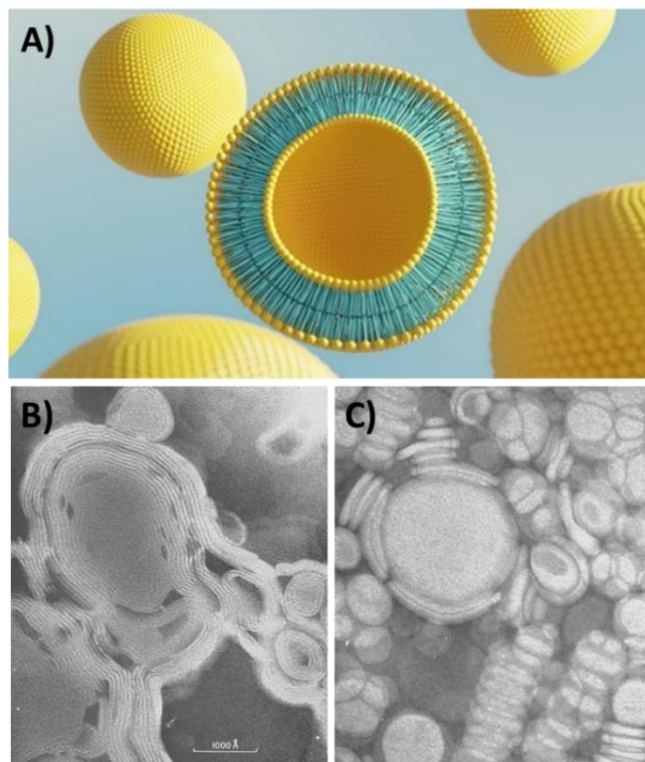


Figure 3. A) A schematic representation of liposomes; B) liposomes composed of lecithin and C) liposomes composed of lecithin and cholesterol observed by Bangham and coworkers in 1964 using an electron microscope.

Unilamellar, multilamellar and multivesicular liposomes differ primarily in the number of bilayers (Figure 4). Unilamellar liposomes have a single lipid bilayer that surrounds the inner aqueous core and could be further classified into two subtypes: small unilamellar vesicles (SUVs, with diameters ranging from 50 to 100 nanometers) and large unilamellar vesicles (LUVs, with diameters typically in the range of 100 nm to 1 μm). Multilamellar liposomes (MLVs), in contrast, have multiple lipid bilayers stacked on top of each other, creating a series of concentric layers surrounding the aqueous core. Finally, multivesicular liposomes (MVLs) are composed of many internal aqueous compartments separated by numerous nonconcentric lipid bilayers.^{17,19,20}

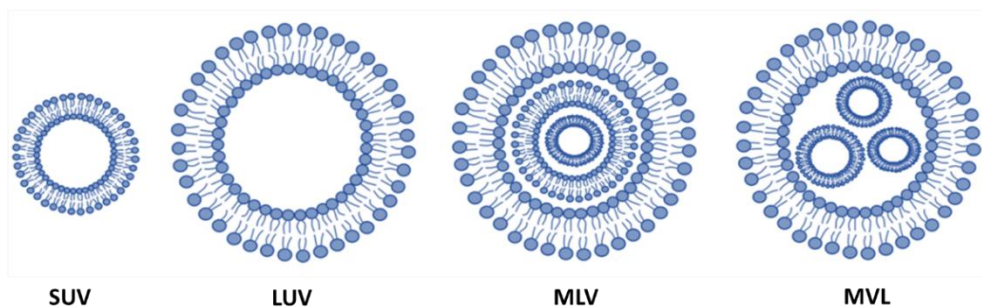


Figure 4. Liposomes classification based on lamellarity and size.

The morphology and the size of the aggregates are mainly controlled by the preparation technique: for example, reverse phase evaporation and solvent injection, as well as technique based on microfluidic chips and on the use of supercritical CO_2 typically results in the formation of LUVs.^{21–26} On the contrary, thin-film hydration technique (Bangham method) results in the formation of MLVs.^{18,21} Anyway, MLVs can be subjected to sonication or extrusion to produce unilamellar dispersions with precisely controlled diameters.^{21,27–29}

Liposomes primarily consist of glycerophospholipids (a glycerol molecule linked to a phosphate group and two fatty acid chains), but they often contain also synthetic surfactants and other components (usually cholesterol, ch, but also proteins or

polymers).³⁰ Their inclusion in liposomes bilayer can enhance the stability of the aggregates and influence their interactions with biological systems.

Lipids in the bilayer are not static, but rather are dynamic: they rotate on their axis and rapidly diffuse laterally in membrane (providing it a fluid structure).³¹

Phospholipids can also move between both leaflets of the bilayer in transverse movement, in a “flip-flop” manner (Figure 5) even if this kind of diffusion is intrinsically very slow.

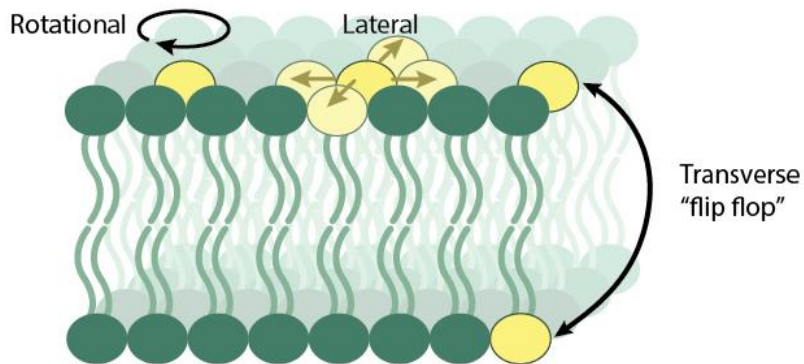


Figure 5. Phospholipids in the lipid bilayer can either move rotationally, laterally in one bilayer, or undergo transverse movement between bilayers.

Given the amphipathic nature of phospholipids and their C_{pp} , they exhibit a strong tendency to create bilayers in an aqueous environment through self-assembly as described in section 1.1:^{17,32} Anyway, liposomes do not form spontaneously, but they require some energy (usually provided by mechanical agitation and/or heating).³³ Liposomes are considered kinetic traps due to the energy barriers that exist during their formation, such as the hydration of hydrophobic tails and the reorganization of phospholipids into a bilayer structure. Once formed, liposomes can be kinetically trapped in their metastable state for prolonged periods of time, but they are not thermodynamically stable. Over time they aggregate, fuse, and eventually precipitate in stacks of infinite, very large, flat bilayers.³³

Liposomes properties such as stability over time, fluidity and permeability are strictly related to their composition. Long saturated hydrocarbon chains exhibit an increased capacity to interact with each other in the bilayer, fostering the formation of structurally rigid bilayer arrangements. On the contrary, phospholipids possessing unsaturated hydrocarbon chains tend to produce liposomes with more fluid and disordered bilayers.³⁴ Electrostatic interactions between charged aggregates can enhance their stability by reducing aggregation and fusion, resulting in a longer shelf life.

Another important parameter that can affect the fluidity of the lipids within the bilayer is the main transition temperature (T_m) of lipids, that indicates the temperature at which the lipid bilayer undergoes a phase transition (Figure 6) changing from a more ordered state (gel phase) to a more disordered and fluid state (liquid crystalline phase). Below T_m , the surface area per lipid is minimal and the bilayer thickness is maximal while, above T_m , the alkyl chains are in their gauche conformation, decreasing the thickness of the bilayer and increasing their permeability.³⁵

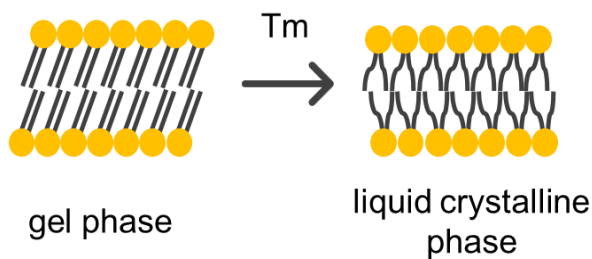


Figure 6. Transition from gel phase to liquid crystalline phase.

T_m varies based on the lipid composition. Specifically, liposomes composed of saturated lipids have a relatively high T_m due to the tight packing of saturated hydrocarbon chains. In contrast, liposomes containing unsaturated lipids feature low T_m because of the kinks introduced by the unsaturated bonds, which disrupt

lipid packing. Chain length and number of unsaturation also plays a role: vesicles composed of lipids with shorter hydrocarbon chains and/or more unsaturation tend to have low T_m .

As mentioned above, a component often present in liposome bilayer is ch, a molecule that can enhance the stability of aggregates.³⁶ Being partially hydrophobic, ch positions itself among the phospholipids with its hydroxyl group near the hydrophilic region and aligns its aromatic rings parallel to the fatty acid chains within the lipid bilayer (Figure 7):³⁷ it promotes an increases compact arrangement of phospholipids, hindering interactions within the lipid chains by intercalating between them. This intercalation promotes the stabilization of the liposomal membrane.^{32,38}

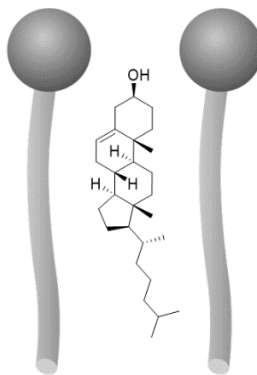


Figure 7. Ch intercalation in lipid bilayer.

The addition of ch to liposomal alters parameters such as fluidity, thickness, compressibility, water penetration, and intrinsic curvature of lipid bilayers, and thus the T_m . In lipid mixtures with multiple components, ch can induce phase separations.^{39,40} At high concentrations (> 30 mol %), ch modify the ordered packing of lipid molecules in the bilayer, abolishing the phase transition.⁴¹ Above 50 mol %, ch phase separates from the membrane into ch-rich domains which can lead to the formation of ch crystals.⁴²

1.3 Lipid Mesophases

Lyotropic liquid crystals (LLCs), also known as lipid mesophases (LMPs), are a class of liquid crystalline materials that exhibit ordered and anisotropic properties in the presence of aqueous media and arise from the self-assembly of peculiar amphiphilic molecules at specific conditions. They display features of both crystalline and liquid substances: similar to crystals, their molecules possess short-range positional order, while like liquids, they lack long-range positional order.^{43,44} LMPs exhibit unique structures contingent on their composition: lamellar, hexagonal, cubic, and micellar cubic phases, among others (Figure 8).⁴⁵

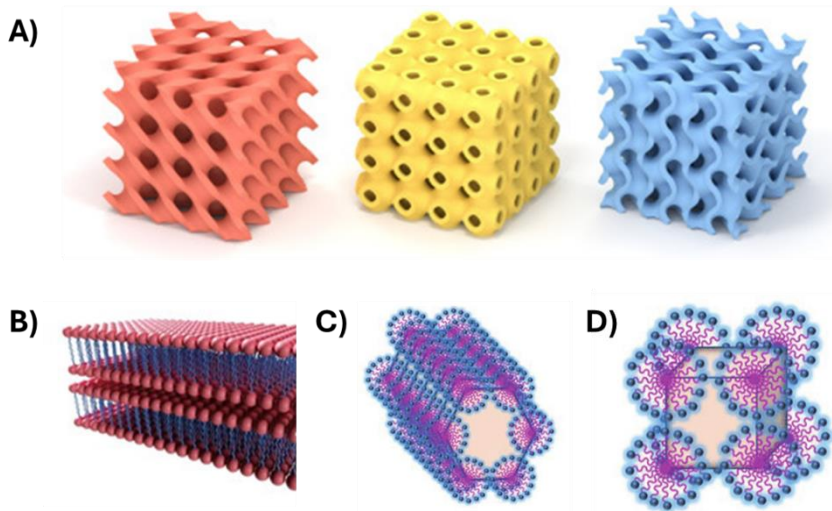


Figure 8. A) Cubic phases ($Pn3m$, $Im3m$, or $Ia3d$), B) lamellar phase, C) hexagonal phase, and D) inverse micellar phase.

The lamellar phase is characterized by a two-dimensional arrangement of amphiphilic bilayers, with aqueous layers between them; each bilayer is composed of two monolayers positioned tail-to-tail to minimize contact between the hydrocarbon chains and water. In this configuration, water predominantly interacts with the lipid polar heads, forming water-lipid head slabs.⁴⁶ The lamellar phase is

termed L_{α} when the lipid tails exhibit disorder within the 2D layers and L_c when they are organized in a lattice.⁴⁷ The hexagonal phase (H_{II}) is constituted by an array of cylindrical micelles organized in a hexagonal lattice. Within this structure, the water-lipid heads form the cylindrical regions, while the lipid tails occupy the continuous matrix.⁴⁸ On the other hand, bicontinuous cubic phases consist of two distinct sets of water channels separated by curved bilayers in three-dimensional space. Each point on the bilayer's midplane surface is a saddle point with a zero-mean curvature. These bilayers enclose a network of organized yet flexible aqueous channels, resulting in a structure that is both nonbirefringent and optically transparent.^{49,50} More specifically, lipid molecules in bicontinuous cubic phases configure a continuous bilayer with high curvature, dividing the two interpenetrating but non-intersecting networks of aqueous channels. These structures can exhibit symmetries such as double gyroid ($Ia3d$, featuring threefold connectivity of aqueous channels), double diamond ($Pn3m$, featuring fourfold connectivity), and primitive ($Im3m$, featuring sixfold connectivity).^{51,52} Lastly, the inverse micellar phase comprises spheroidal micelles arranged in either $Fd3m$ and $Fm3m$ symmetry, or a disordered state, denoted as L_2 .⁵⁰

Lipids, in particular phytantriol, monoolein (MO), and monolinolein are widely recognized as molecules with the ability to undergo self-assembly in water forming LMPs.⁵³⁻⁵⁵

The phase diagrams of MO (Figure 9) depicts its behavior under conditions of thermodynamic equilibrium.⁵¹

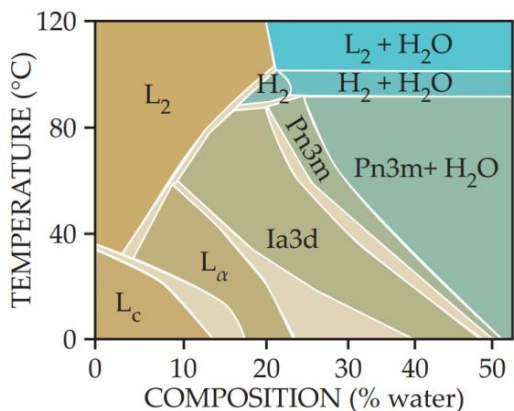


Figure 9. Phase diagram of MO.

The lipid-water mixtures exhibit different mesogenic behavior as a function of either the water content and/or the temperature. An increase in water content initiates a transformation of the lamellar phase, which first transitions into an Ia3d phase and subsequently evolves into a Pn3m phase. Beyond this point, further hydration results in coexistence between the Pn3m phase and excess water. On the contrary, elevating the system's temperature induces a shift from the cubic phase to an inverse hexagonal phase. Once the maximum hydration level is achieved, the Pn3m phase cannot further swell. Any surplus water introduced into the system remains confined outside the cubic structure, resulting in a state of thermodynamic equilibrium where the Pn3m bicontinuous cubic phase coexists with excess water. Excess water coexisting in a state of thermodynamic equilibrium with LMPs is a pivotal and distinguishing characteristic of these structures: differently from liposomes, they maintain their stability over time.⁵⁶

1.4 Bibliography

1. Anastopoulos, I. *et al.* Surface active agents and their health-promoting properties: Molecules of multifunctional significance. *Pharmaceutics* vol. 12 1–35 Preprint at <https://doi.org/10.3390/pharmaceutics12070688> (2020).
2. Ghosh, S., Ray, A. & Pramanik, N. Self-assembly of surfactants: An overview on general aspects of amphiphiles. *Biophysical Chemistry* vol. 265 Preprint at <https://doi.org/10.1016/j.bpc.2020.106429> (2020).
3. Marques, E. F. & Silva, B. F. B. *Encyclopedia of Colloid and Interface Science*. *Encyclopedia of Colloid and Interface Science* (Springer Berlin Heidelberg, 2013). doi:10.1007/978-3-642-20665-8.
4. Nagarajan, R. *Self-Assembly from Surfactants to Nanoparticles-Head vs. Tail*. (2019).
5. McBain, J. W. General discussion on colloids and their viscosity. *Trans. Faraday Soc.* 99–101 (1913).
6. Maibaum, L., Dinner, A. R. & Chandler, D. Micelle formation and the hydrophobic effect. *Journal of Physical Chemistry B* **108**, 6778–6781 (2004).
7. Cui, X., Mao, S., Liu, M., Yuan, H. & Du, Y. Mechanism of surfactant micelle formation. *Langmuir* **24**, 10771–10775 (2008).
8. Tanford, C. *The Hydrophobic Effect and the Organization of Living Matter*. www.sciencemag.org (1881).
9. Nagarajan, R. Constructing a molecular theory of self-assembly: Interplay of ideas from surfactants and block copolymers. *Adv Colloid Interface Sci* **244**, 113–123 (2017).
10. Israelachvili, J. N., Mitchell, D. J. & Ninham, B. W. Theory of self-assembly of hydrocarbon amphiphiles into micelles and bilayers. *Journal of the*

Chemical Society, Faraday Transactions 2: Molecular and Chemical Physics
vol. 72 1525–1568 Preprint at <https://doi.org/10.1039/F29767201525>
(1976).

11. Israelachvili, J. *Self-Assembly in Two Dimensions: Surface Micelles and Domain Formation in Monolayers*. *Langmuir* vol. 10 <https://pubs.acs.org/sharingguidelines> (1994).
12. Dutt, S., Siril, P. F. & Remita, S. Swollen liquid crystals (SLCs): A versatile template for the synthesis of nano structured materials. *RSC Advances* vol. 7 5733–5750 Preprint at <https://doi.org/10.1039/c6ra26390a> (2017).
13. Lombardo, D., Calandra, P., Barreca, D., Magazù, S. & Kiselev, M. A. Soft interaction in liposome nanocarriers for therapeutic drug delivery. *Nanomaterials* vol. 6 Preprint at <https://doi.org/10.3390/nano6070125> (2016).
14. Liu, P., Chen, G. & Zhang, J. A Review of Liposomes as a Drug Delivery System: Current Status of Approved Products, Regulatory Environments, and Future Perspectives. *Molecules* vol. 27 Preprint at <https://doi.org/10.3390/molecules27041372> (2022).
15. Bangham, A. D. Liposomes: Realizing their promise. *Hosp Pract* **27**, (1992).
16. Bangham, A. D. & Horne, R. W. Negative staining of phospholipids and their structural modification by surface-active agents as observed in the electron microscope. *J Mol Biol* **8**, 660–668 (1964).
17. Monteiro, N., Martins, A., Reis, R. L. & Neves, N. M. Liposomes in tissue engineering and regenerative medicine. *Journal of the Royal Society Interface* vol. 11 Preprint at <https://doi.org/10.1098/rsif.2014.0459> (2014).
18. Trucillo, P., Campardelli, R. & Reverchon, E. Liposomes: From bangham to supercritical fluids. *Processes* vol. 8 Preprint at <https://doi.org/10.3390/pr8091022> (2020).

19. Akbarzadeh, A. *et al.* Liposome: Classification, preparation, and applications. *Nanoscale Res Lett* **8**, (2013).
20. Guimarães, D., Cavaco-Paulo, A. & Nogueira, E. Design of liposomes as drug delivery system for therapeutic applications. *International Journal of Pharmaceutics* vol. 601 Preprint at <https://doi.org/10.1016/j.ijpharm.2021.120571> (2021).
21. Fan, M., Xu, S., Xia, S. & Zhang, X. Effect of different preparation methods on physicochemical properties of salidroside liposomes. *J Agric Food Chem* **55**, 3089–3095 (2007).
22. Szoka, F. & Papahadjopoulos, D. *Procedure for Preparation of Liposomes with Large Internal Aqueous Space and High Capture by Reverse-Phase Evaporation (Drug Delivery/Encapsulation/Lipid Vesicles/Encapsulated Macromolecules)*. vol. 75 (1978).
23. Imura, T. *et al.* *Preparation and Physicochemical Properties of Various Soybean Lecithin Liposomes Using Supercritical Reverse Phase Evaporation Method*. www.elsevier.com/locate/colsurfb.
24. Mertins, O., Sebben, M., Pohlmann, A. R. & Da Silveira, N. P. Production of soybean phosphatidylcholine-chitosan nanovesicles by reverse phase evaporation: A step by step study. *Chem Phys Lipids* **138**, 29–37 (2005).
25. Van Swaay, D. & Demello, A. Microfluidic methods for forming liposomes. *Lab on a Chip* vol. 13 752–767 Preprint at <https://doi.org/10.1039/c2lc41121k> (2013).
26. Otake, K., Imura, T., Sakai, H. & Abe, M. Development of a new preparation method of liposomes using supercritical carbon dioxide. *Langmuir* **17**, 3898–3901 (2001).
27. Cho, N. J., Hwang, L. Y., Solandt, J. J. R. & Frank, C. W. Comparison of extruded and sonicated vesicles for planar bilayer self-assembly. *Materials* **6**, 3294–3308 (2013).

28. Ong, S. G. M., Chitneni, M., Lee, K. S., Ming, L. C. & Yuen, K. H. Evaluation of extrusion technique for nanosizing liposomes. *Pharmaceutics* **8**, (2016).
29. de Freitas, C. F., Calori, I. R., Tessaro, A. L., Caetano, W. & Hioka, N. Rapid formation of Small Unilamellar Vesicles (SUV) through low-frequency sonication: An innovative approach. *Colloids Surf B Biointerfaces* **181**, 837–844 (2019).
30. Nsairat, H. *et al.* Liposomes: structure, composition, types, and clinical applications. *Heliyon* vol. 8 Preprint at <https://doi.org/10.1016/j.heliyon.2022.e09394> (2022).
31. Sharom, F. J. Flipping and flopping-lipids on the move. *IUBMB Life* vol. 63 736–746 Preprint at <https://doi.org/10.1002/iub.515> (2011).
32. Bozzuto, G. & Molinari, A. Liposomes as nanomedical devices. *International Journal of Nanomedicine* vol. 10 975–999 Preprint at <https://doi.org/10.2147/IJN.S68861> (2015).
33. On the Thermodynamic Stability of Liposomes. *J Colloid Interface Sci* **140**, 302–304 (1990).
34. Rawicz, W., Olbrich, K. C., McIntosh, T., Needham, D. & Evans, E. A. Effect of chain length and unsaturation on elasticity of lipid bilayers. *Biophys J* **79**, 328–339 (2000).
35. Chapman, D. *Phase Transitions and Fluidity Characteristics of Lipids and Cell Membranes*. *Quarterly Reviews of Biophysics* vol. 8 (1975).
36. Sułkowski, W. W., Pentak, D., Nowak, K. & Sułkowska, A. The influence of temperature, cholesterol content and pH on liposome stability. *J Mol Struct* **744–747**, 737–747 (2005).
37. Beltrán-Gracia, E., López-Camacho, A., Higuera-Ciapara, I., Velázquez-Fernández, J. B. & Vallejo-Cardona, A. A. Nanomedicine review: Clinical developments in liposomal applications. *Cancer Nanotechnology* vol. 10 Preprint at <https://doi.org/10.1186/s12645-019-0055-y> (2019).

38. Lee, S. C., Lee, K. E., Kim, J. J. & Lim, S. H. The effect of cholesterol in the liposome bilayer on the stabilization of incorporated retinol. *J Liposome Res* **15**, 157–166 (2005).
39. Yang, S. T., Kreutzberger, A. J. B., Lee, J., Kiessling, V. & Tamm, L. K. The role of cholesterol in membrane fusion. *Chem Phys Lipids* **199**, 136–143 (2016).
40. Dé Rick De Meyer, F., Smit, B. & Klein, M. L. *Effect of Cholesterol on the Structure of a Phospholipid Bilayer*. vol. 106 www.pnas.org/cgi/doi/10.1073/pnas.0809959106 (2009).
41. Rappolt, M. *et al.* Structural, dynamic and mechanical properties of POPC at low cholesterol concentration studied in pressure/temperature space. *European Biophysics Journal* **31**, 575–585 (2003).
42. Huang, Z. & Szoka, F. C. Sterol-modified phospholipids: Cholesterol and phospholipid chimeras with improved biomembrane properties. *J Am Chem Soc* **130**, 15702–15712 (2008).
43. Dierking, I. & Al-Zangana, S. Lyotropic liquid crystal phases from anisotropic nanomaterials. *Nanomaterials* vol. 7 Preprint at <https://doi.org/10.3390/nano7100305> (2017).
44. Holmberg, K., Shah, D. O. (Dinesh O. & Schwuger, M. J. (Milan J.). *Handbook of Applied Surface and Colloid Chemistry*. (Wiley, 2002).
45. Mezzenga, R. *et al.* Nature-Inspired Design and Application of Lipidic Lyotropic Liquid Crystals. *Advanced Materials* vol. 31 Preprint at <https://doi.org/10.1002/adma.201900818> (2019).
46. Yeagle, P. L. Structures of Lipid Assemblies. in *The Membranes of Cells* 115–154 (Elsevier, 2016). doi:10.1016/b978-0-12-800047-2.00007-3.
47. Seddon, J. M. & Templer, R. H. *Polymorphism of Lipid-Water Systems*.

48. Jouhet, J. Importance of the hexagonal lipid phase in biological membrane organization. *Frontiers in Plant Science* vol. 4 Preprint at <https://doi.org/10.3389/fpls.2013.00494> (2013).
49. Qiu, H., Ca, M. & Rey, ! *The Phase Diagram of the Monoolein/Water System: Metastability and Equilibrium Aspects. Biomaterials* vol. 21 (2000).
50. Sakya, P., Seddon, J. M., Templer, R. H., Mirkin, R. J. & Tiddy, G. J. T. *Micellar Cubic Phases and Their Structural Relationships: The Nonionic Surfactant System C 12 EO 12 /Water.* (1997).
51. Aleandri, S. & Mezzenga, R. The physics of lipidic mesophase delivery systems. *Phys Today* **73**, 38–44 (2020).
52. Luzzati, V. & Husson, F. THE STRUCTURE OF THE LIQUID-CRYSTALLINE PHASES OF LIPID-WATER SYSTEMS. *J. Cell Biol* **12**, (1962).
53. Barauskas, J. & Landh, T. Phase behavior of the phytantriol/water system. *Langmuir* vol. 19 9562–9565 Preprint at <https://doi.org/10.1021/la0350812> (2003).
54. Kulkarni, C. V., Wachter, W., Iglesias-Salto, G., Engelskirchen, S. & Ahualli, S. Monoolein: A magic lipid? *Physical Chemistry Chemical Physics* vol. 13 3004–3021 Preprint at <https://doi.org/10.1039/c0cp01539c> (2011).
55. Chen, Y., Ma, P. & Gui, S. Cubic and hexagonal liquid crystals as drug delivery systems. *Biomed Res Int* **2014**, (2014).
56. Fong, C., Le, T. & Drummond, C. J. Lyotropic liquid crystal engineering—ordered nanostructured small molecule amphiphile self-assembly materials by design. *Chem Soc Rev* **41**, 1297–1322 (2012).

Chapter 2. Drug Delivery Systems: An Overview

2. Evolution of Drug Delivery Systems

Many drugs fall short of realizing their full potential in clinical applications, and this can be attributed to various factors, including:¹

- lack of *in vivo* selectivity, leading to unexpected side effects;
- low therapeutic index, where the required dose for effectiveness proves toxic to normal tissues, either due to intrinsic properties of the molecule or the need for high dosages;
- poor solubility of the active ingredient in water, and consequently, in the bloodstream;
- inability to achieve therapeutic concentrations at the target site;
- challenges associated with drug formulation, such as low solubility in pharmaceutically suitable vehicles;
- low stability in biological fluids;
- high probability of inducing allergic reactions;
- pharmacokinetics requiring a high frequency of daily administrations to maintain drug levels within the desired range.

These factors collectively contribute to the underperformance of many drugs in clinical settings. Hence, there is a requirement for efficient drug delivery systems (DDS). A DDS defined as a formulation or a device that is able to protect an active principle, prolong its half-life, localize and direct it to the affected tissue with a secure interaction² and predefined release kinetics and duration.³

Over years, DDS have demonstrated their ability to enhance treatment outcomes in various ways, such as improving the effectiveness of therapies, minimizing drug toxicity, improving water-solubility of poorly soluble drugs, overcoming biological barriers, promoting patient adherence and even facilitating the development of

entirely new medical treatments.⁴ Drug delivery technology has also advanced to address the distinctive requirements of emerging generation of therapeutics including proteins, peptides, monoclonal antibodies, nucleic acids and even live cells.^{5,6}

Prior to 1950, all medications were formulated as pills or capsules that released the enclosed drug promptly upon contact with water, lacking the capability to regulate the rate of drug release. First-generation DDSs were developed between 1950 and 1980 with the aim of improving drug stability, solubility, and bioavailability and a focus on enhancing drug formulation and delivery methods.⁷ In 1952, S. K. Beecham introduced the first sustained-release formulation based on gelatin capsule and natural waxes, which could control the kinetics of drug release and maintain efficacy for 12 hours.^{8,9} This innovation, referred to as Spansule[®] technology, is particularly useful for medications that need to be taken once or twice daily, as it can help maintain a steady level of the drug in the patient's bloodstream, potentially improving treatment outcomes and reducing the frequency of dosing.⁹ Spansule[®] achieved these goals by using a combination of different layers of a slowly soluble coating material (gelatine or cellulose derivatives) within a capsule or tablet.³

In 1956, the inception of pressurized metered dose inhalers marked the beginning of inhalation delivery system advancements, achieving effective lung delivery. It rapidly became the dominant delivery system for treatment of asthma.¹⁰ In 1979, transdermal patches containing scopolamine became accessible in the market with the approval of Transderm Scop[®] for preventing motion sickness.¹¹ It demonstrated that transdermal administration of scopolamine could alleviate certain side effects associated with the drug in contrast to oral delivery.

The second generation of DDSs (1980 – 2010) represents an advancement over earlier formulations, incorporating innovative strategies to enhance therapeutic efficacy, reduce toxicity, and improve patient compliance. It was dedicated to

development of zero-order release systems, self-regulated drug delivery systems, long-term depot formulations, and nanotechnology-based delivery systems.¹² During this years, Doxil[®] emerged in 1995 as the first liposomal anticancer, while Abraxane[®], the first albumin-bound nanoparticles anticancer, was available in the market in 2005. The approvals of Doxil[®] and Abraxane[®] were based primarily on reduced side effects rather than superior efficacy of the drugs.³ During these years, thousands of different nanoparticle formulations have been prepared and tested for their presumed ability to provide better treatment, especially in cancer therapy. Advancements in drug delivery technologies are ongoing with the third generation of DDS (2010 – present), that has a focus on personalized medicine and targeted therapy.

2.1 Liposomes as DDSs

Liposomes are the most successful nanoparticle-based delivery systems developed until now and continue to constitute an intense field of research.¹³ They are considered a powerful DDS due to their biocompatibility, biodegradability and non-toxic nature, as well as their structural versatility that can regulate their biological characteristics.^{14,15} Their unique structure allows liposomes to encapsulate both hydrophilic (within the aqueous core) and hydrophobic compounds (incorporated into the lipid bilayer).¹³ The encapsulation of drugs within liposomes provides protection against physiological processes, including enzymatic degradation, chemical and immunologic inactivation, and rapid plasma clearance. This protective environment enhances the drug's effectiveness, prolongs its duration of action and favor accumulation in the target tissue. By confining the drug within the liposome, exposure to healthy tissues can be minimized, leading to a reduction in undesirable side effects when compared to the free form of the drug.¹⁶

Based on their composition and functionalization, liposomes can be classified into conventional, PEGylated, ligand-targeted, and magnetic.

Conventional liposomes are composed of neutral or charged phospholipids,^{17,18} usually in combination with ch to improve the stability of the formulation (as explained in paragraph 1.2).¹⁵ Electrostatic interactions between cationic formulations may promote the binding of liposomes to charged tissues or cells. Nevertheless, the major drawback of these formulations includes instability in plasma that leads to a short blood circulation half-life: vesicles are quickly entrapped by the reticuloendothelial system and subsequently eliminated from the bloodstream.¹⁸ To address these challenges, a second generation of liposomes was developed, giving rise to PEGylated – or stealth - liposomes.¹⁹ The stealth approach primarily involves the ability to coat the liposomal membrane surface with biocompatible hydrophilic polymer conjugates, usually based on polyethylene glycol (PEG). This coating enhances the repulsive forces between liposomes and serum components.²⁰ As result, it reduces immunogenicity and macrophage uptake, leading to an extended blood circulation half-life.²¹ However, PEG prevents the selective delivery of the encapsulated compound to specific target cells.²² To overcome this limitation, researchers have developed ligand-targeted liposomes designed for the precise delivery of compounds to specific tissues, promoting increased selectivity and enhanced therapeutic efficacy.¹⁸ In addition to surface modification with PEG, targeted liposomes are further modified by incorporating glycoproteins, polysaccharides, or specific ligands such as antibodies, small molecules, or peptides.^{22,23} These ligands can selectively bind to receptors that are overexpressed on the surfaces of diseased cells, minimizing off-target effects on healthy cells.^{24,25}

The concept of magnetic liposomes (MLs), a fascinating type of nanostructure that combines liposomes with magnetic nanoparticles (MNPs), was first introduced by M. De Cuyper and M. Joniau in a research paper published in 1993.²⁶ To obtain this kind of system, MNPs could be covered with a lipid bilayer (solid MLs, Figure 1), entrapped in the aqueous core of liposomes as a dispersion (aqueous MLs), or they

could be non-covalently functionalized with a lipophilic coating in order to be embedded in the lipid bilayer of common liposomes (aqueous MLs).²⁷

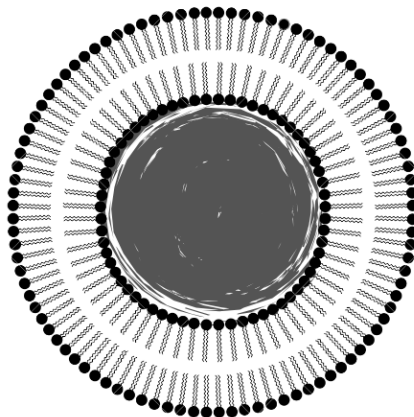


Figure 1. A representation of solid MLs.

This fusion between liposomes and MNPs results in a versatile and innovative magnetic nanomaterial with a range of potential applications, especially in targeted drug delivery, as MLs could be directed to specific areas within the body using external magnetic fields, thus minimizing off-target effects, and improving drug efficacy.^{28–30} They also found application as contrast agents in biomedical imaging^{31–33} and for hyperthermia therapy.^{34–37} The abovementioned architectures (solid or aqueous) need to be selected according to the applications, as each presents advantages and disadvantages. Solid MLs, for example, lack of the aqueous core, limiting their application to the vehiculation of lipophilic molecules. Despite iron oxides MNPs have been approved by FDA for clinical trial studies in humans, the high metal-to-lipid ratio of solid MLs enables high cellular metal uptakes. Aqueous MLs, instead, can carry both hydrophobic and hydrophilic drugs, and show a reduced metal-to-lipid ratio; the major drawback is that they possess reduced magnetic properties due to the extra water mass.

Drug release from liposomes can occur through several mechanisms, depending on the liposomal formulation and environmental conditions. Temperature and pH are

two of the most promising triggers in the development of sensitive formulations to improve the efficacy of drugs.^{38,39} pH-Sensitive liposomes designed to release their payload in response to changes in the acidity of the surrounding environment of specific target tissues. The concept is based on the fact that tumors usually have a lower pH than healthy tissues⁴⁰ and pH-sensitive liposomes are prepared to release the incorporated drug only when subjected to this unique tumor condition. This potentially reducing off-target effects and improving therapeutic outcomes.

In 1978, Yatvin *et al.* suggested for the first time the use of temperature-sensitive liposomes - that release the encapsulated drug in response to heat - combined with hyperthermia for targeting the drug to specific sides.⁴¹ The fundamental concept was to administer the liposomal formulation systemically and then selectively expose to heat only the tissue region where drug delivery is intended. They proposed to use a mixed liposomal formulation that have a T_m of 42–44°C (slightly higher than the one of the human body): upon heating, lipids undergo a transformation from a solid gel-like structure to a highly permeable structure, releasing the drug they vehiculate.^{41,42}

Drug release could also be triggered by changes in redox potential, electrolyte concentrations, as well as the application of ultrasound, electric fields, or magnetic fields.^{43,44}

Currently, scientific literature is rich of studies regarding liposome-based systems and twenty-five liposomal formulations are on the market (Table 1), and additional formulations are under studies.⁴⁵

Table 1.⁴⁵ Liposomal formulation on the market in 2023

Product name	Drug name	Application
Doxil/Caelyx	Doxorubicin	Anti-cancer therapy
AmBisome	Amphotericin B	Anti-fungal agent

Epaxal	Inactivated hepatitis A	Vaccine
Abelcet	Amphotericin B	Anti-fungal agent
DaunoXome	Daunorubicin	Anti-cancer therapy
Amphotec	Amphotericin B	Anti-fungal agent
Inflexal V	Influenza virus	Vaccine
Depocyte	Cytarabine	Anti-cancer therapy
Visudyne	Verteporfin	Photodynamic therapy
Myocet	Doxorubicin	Anti-cancer therapy
LipoDox	Doxorubicin	Anti-cancer therapy
Lipusu	Paclitaxel	Anti-cancer therapy
DepoDur	Morphine	Analgesic
Mepact	Mifamurtide	Anti-cancer therapy
Exparel	Bupivacaine	Analgesic
Marqibo	Vincristine	Anti-cancer therapy
Onivyde	Irinotecan	Anti-cancer therapy
Mosquirix	RTS,S (antigen)	Vaccine
Vyxeos	Daunorubicin/cytarabine	Anti-cancer therapy
Nocita	Bupivacaine	Analgesic
Shingrix	Glycoprotein E	Vaccine
Onpattro	Patisiran	RNAi
Arikayce	Amikacin	Anti-fungal agent
Comirnaty	Coronavirus vaccine	Vaccine
Spikevax	Coronavirus vaccine	Vaccine

2.3 Lipid Mesophases as DDSs

The thermodynamic stability of LMPs, as well their biocompatibility and versatility, makes them valuable as DDSs. Being composed of lipid bilayers and water channels,

LMPs can vehiculate a wide range of drug molecules, both hydrophilic and hydrophobic, and they can be functionalized to incorporate targeting ligands on their surfaces, enabling site-specific drug delivery, reducing off-target effects, and improving treatment precision. One of the key advantages of LMPs is their ability to undergo structural transformations in response to changes in environmental conditions such as temperature, pH, or the presence of specific ions. This responsiveness allows for tunable drug release profiles, making LMPs a promising candidate for personalized medicine.

LMPs gradually release both hydrophobic and hydrophilic biomacromolecules. On the contrary, certain small hydrophilic drugs encapsulated within the water channels of a mesophase may experience rapid release. So far, the most frequently investigated methods for regulating the release of hydrophilic drugs from LMPs involve several key strategies: leveraging ionic interactions between the drug and the polar groups of lipids, modifying the dimensions of the aqueous channels within the mesophase, and employing lipid prodrugs (compounds that activate within the body to generate the active drug). The release mechanisms of hydrophilic compounds are closely tied to the mesophase's structure. The release process itself refers to a Fickian diffusion pattern and follows a first-order kinetic profile, with its kinetics primarily influenced by the size of the aqueous channels within the mesophase, the dimensions of the drug molecules, and notably, the symmetry of the mesophase.⁴⁶ For hydrophilic drug molecules to be released, they must cross the water and the lipid regions: the ability of lipids to confine a drug within the water channels exerts control over its release. The rate of drug diffusion is contingent upon the dimensionality (d) of the water domains, which is defined as the number of orthogonal directions a molecule can explore within the water channel without exiting. In the micellar cubic mesophase, the drug is restricted within micelles with water domains of approximately 2 nm in diameter ($d = 0$). In the hexagonal phase, molecules move through cylindrical water channels ($d = 1$),

while in a lamellar phase, they can get across planar water layers ($d = 2$). Within bicontinuous cubic phases, the diffusion process occurs in three dimensions ($d = 3$). Here, the movement of hydrophilic molecules that are embedded is primarily impeded by the channel size (which is approximately 3-5 nm in diameter) and its tortuosity. The less permeable Im3m symmetry exhibits a lower transport efficiency under similar water content conditions when compared with the more permeable Pn3m geometry. Unexpectedly, the connectivity of the water channels does not affect the diffusion process.

As a general rule, the diffusion coefficient of a hydrophilic drug experiences a decrease as the dimensionality of the phase increases. Consequently, Pn3m phases ($d = 3$) exhibit the highest diffusion coefficients, while micellar cubic phases ($d = 0$) display the lowest.⁴⁶

LMPs offer flexibility in terms of design and structure, allowing researchers to fine-tune their properties for specific drug delivery applications. For example, additives have the capacity to alter their structure: by introducing substances like hexadecane or vitamin E, it's possible to tune the phase of the MO-water system. This variation in phase results in changes to the release profile and, consequently, the drug diffusion coefficient. Certain additives (such as sucrose stearate, phospholipids, and ch) can enhance the dimensions of water channels modulating hydration.⁴⁶ Electrostatic swelling is another method to expand the size of water channels, achieved by either incorporating charged lipids into the mesophases to induce swelling or by reducing the chemical potential of water within the nanochannels. This alteration forces the system to require a greater amount of water to reach equilibrium. Research conducted by multiple groups has demonstrated the effectiveness of electrostatic swelling, with cubic phases exhibiting water channels more than five times larger than those in traditional lipidic mesophases.⁴⁷⁻⁴⁹ With that approach, one could load large hydrophilic biomacromolecules.⁵⁰

The introduction of small concentrations of electrolytes into the aqueous phase of water-amphiphile systems can have a substantial impact on the associated phase diagrams. In the case of MO-water mixtures, the specific type and quantity of electrolyte can lead to either the expansion or contraction of water channels. For example, NaCl causes a dehydration of the MO headgroups at the interface, resulting in a reduction of their effective occupied area, leading to a contraction of the water channels. Contrariwise, the presence of NaI promotes increased hydration of the lipid headgroups, expanding the interfacial area covered by a MO headgroup and consequently causing the water channels in the cubic phase to swell.⁴⁶

The release of a drug can also be regulated by incorporating additives that make the delivery system responsive to both internal factors like pH and temperature and external stimuli such as light and magnetic fields. Through careful molecular design, it becomes possible to achieve spatial and temporal control over the delivery of therapeutic agents, enabling triggered drug release. For example, mesophases formed from a mixture of monolinolein and water with the inclusion of pyridinylmethyl-linoleate undergo a transition from a hexagonal to a cubic structure when exposed to the mildly acidic pH commonly found in cancerous tissues: the phase transition results in an accelerated drug release of the hydrophilic anticancer drug doxorubicin loaded within the engineered mesophase.⁵¹

It is also possible to directly influence the assembly of nanocarriers and, consequently, facilitate drug release. For example, a mesophase responsive to light, which includes a blend of monoolein and a small quantity of light-sensitive lipids, exhibits sequential drug release triggered by exposure to UV light. Conversely, when exposed to visible light, it retains a hydrophilic dye embedded within it.⁵²

2.4 Bibliography

1. Sharma, A. & Sharma, U. S. *International Journal of Pharmaceutics Review Liposomes in Drug Delivery: Progress and Limitations. International Journal of Pharmaceutics* vol. 154 (1997).
2. Anselmo, A. C. & Mitragotri, S. An overview of clinical and commercial impact of drug delivery systems. *Journal of Controlled Release* vol. 190 15–28 Preprint at <https://doi.org/10.1016/j.jconrel.2014.03.053> (2014).
3. Park, H., Otte, A. & Park, K. Evolution of drug delivery systems: From 1950 to 2020 and beyond. *Journal of Controlled Release* **342**, 53–65 (2022).
4. Jain, K. K. *Drug Delivery Systems-An Overview*.
5. Vargason, A. M., Anselmo, A. C. & Mitragotri, S. The evolution of commercial drug delivery technologies. *Nature Biomedical Engineering* vol. 5 951–967 Preprint at <https://doi.org/10.1038/s41551-021-00698-w> (2021).
6. Gao, J., Karp, J. M., Langer, R. & Joshi, N. The Future of Drug Delivery. *Chemistry of Materials* vol. 35 359–363 Preprint at <https://doi.org/10.1021/acs.chemmater.2c03003> (2023).
7. Yun, Y. H., Lee, B. K. & Park, K. Controlled Drug Delivery: Historical perspective for the next generation. *Journal of Controlled Release* **219**, 2–7 (2015).
8. Yu, L., Liu, S., Jia, S. & Xu, F. Emerging frontiers in drug delivery with special focus on novel techniques for targeted therapies. *Biomedicine and Pharmacotherapy* vol. 165 Preprint at <https://doi.org/10.1016/j.biopha.2023.115049> (2023).
9. Park, H., Otte, A. & Park, K. Evolution of drug delivery systems: From 1950 to 2020 and beyond. *Journal of Controlled Release* **342**, 53–65 (2022).
10. Stein, S. W. & Thiel, C. G. The History of Therapeutic Aerosols: A Chronological Review. *Journal of Aerosol Medicine and Pulmonary Drug Delivery* vol. 30 20–41 Preprint at <https://doi.org/10.1089/jamp.2016.1297> (2017).

11. Ramadan, D., McCrudden, M. T. C., Courtenay, A. J. & Donnelly, R. F. Enhancement strategies for transdermal drug delivery systems: current trends and applications. *Drug Deliv Transl Res* **12**, 758–791 (2022).
12. Park, K. Controlled drug delivery systems: Past forward and future back. *Journal of Controlled Release* vol. 190 3–8 Preprint at <https://doi.org/10.1016/j.jconrel.2014.03.054> (2014).
13. Guimarães, D., Cavaco-Paulo, A. & Nogueira, E. Design of liposomes as drug delivery system for therapeutic applications. *International Journal of Pharmaceutics* vol. 601 Preprint at <https://doi.org/10.1016/j.ijpharm.2021.120571> (2021).
14. Mathiyazhakan, M., Wiraja, C. & Xu, C. A concise review of gold nanoparticles-based photo-responsive liposomes for controlled drug delivery. *Nanomicro Lett* **10**, 1–10 (2018).
15. Sercombe, L. *et al.* Advances and challenges of liposome assisted drug delivery. *Frontiers in Pharmacology* vol. 6 Preprint at <https://doi.org/10.3389/fphar.2015.00286> (2015).
16. Bozzuto, G. & Molinari, A. Liposomes as nanomedical devices. *International Journal of Nanomedicine* vol. 10 975–999 Preprint at <https://doi.org/10.2147/IJN.S68861> (2015).
17. Cattel, L., Ceruti, M. & Dosio, F. From Conventional to Stealth Liposomes: a New Frontier in Cancer Chemotherapy. *Journal of Chemotherapy* **16**, 94–97 (2004).
18. Feng, S. S. New-concept chemotherapy by nanoparticles of biodegradable polymers: Where are we now? *Nanomedicine* vol. 1 297–309 Preprint at <https://doi.org/10.2217/17435889.1.3.297> (2006).
19. Saraf, S. *et al.* Advances in liposomal drug delivery to cancer: An overview. *Journal of Drug Delivery Science and Technology* vol. 56 Preprint at <https://doi.org/10.1016/j.jddst.2020.101549> (2020).
20. Hatakeyama, H., Akita, H. & Harashima, H. *The Polyethyleneglycol Dilemma: Advantage and Disadvantage of PEGylation of Liposomes for Systemic Genes and Nucleic Acids Delivery to Tumors. Biol. Pharm. Bull* vol. 892 (2013).

21. Madni, A. *et al.* *Liposomal Drug Delivery: A Versatile Platform for Challenging Clinical Applications. J Pharm Pharm Sci* (www.cspCanada.org) vol. 17 www.cspCanada.org (2014).
22. Torchilin, V. P. Recent advances with liposomes as pharmaceutical carriers. *Nature Reviews Drug Discovery* vol. 4 145–160 Preprint at <https://doi.org/10.1038/nrd1632> (2005).
23. Riaz, M. K. *et al.* Surface functionalization and targeting strategies of liposomes in solid tumor therapy: A review. *International Journal of Molecular Sciences* vol. 19 Preprint at <https://doi.org/10.3390/ijms19010195> (2018).
24. Fathi, S. & Oyelere, A. K. Liposomal drug delivery systems for targeted cancer therapy: Is active targeting the best choice? *Future Medicinal Chemistry* vol. 8 2091–2112 Preprint at <https://doi.org/10.4155/fmc-2016-0135> (2016).
25. Le, N. T. T. *et al.* Soy lecithin-derived liposomal delivery systems: Surface modification and current applications. *International Journal of Molecular Sciences* vol. 20 Preprint at <https://doi.org/10.3390/ijms20194706> (2019).
26. De Cuyper, M. & Joniau, M. *Magnetoproteoliposomes. Journal of Magnetism and Magnetic Materials* vol. 122 (1993).
27. Veloso, S. R. S., Andrade, R. G. D. & Castanheira, E. M. S. Magnetoliposomes: recent advances in the field of controlled drug delivery. *Expert Opin Drug Deliv* **18**, 1323–1334 (2021).
28. Babincová, M., Čičmanec, P., Altanerová, V., Altaner, Č. & Babinec, P. AC-magnetic field controlled drug release from magnetoliposomes: Design of a method for site-specific chemotherapy. *Bioelectrochemistry* **55**, 17–19 (2002).
29. Nappini, S., Bombelli, F. B., Bonini, M., Nordèn, B. & Baglioni, P. Magnetoliposomes for controlled drug release in the presence of low-frequency magnetic field. *Soft Matter* **6**, 154–162 (2009).
30. Nappini, S. *et al.* Controlled drug release under a low frequency magnetic field: Effect of the citrate coating on magnetoliposomes stability. *Soft Matter* **7**, 1025–1037 (2011).

31. Roberts, D., Zhu, W. L., Frommen, C. M. & Rosenzweig, Z. Synthesis of gadolinium oxide magnetoliposomes for magnetic resonance imaging. *J Appl Phys* **87**, 6208–6210 (2000).
32. Martina, M. S., Wilhelm, C. & Cle, O. Magnetic Targeting of Magnetoliposomes to Solid Tumors with MR Imaging Purpose : Methods : Results : Conclusion : *Radiology* **239**, 415–424 (2006).
33. Soenen, S. J., Velde, G. Vande, Ketkar-Atre, A., Himmelreich, U. & De Cuyper, M. Magnetoliposomes as magnetic resonance imaging contrast agents. *Wiley Interdiscip Rev Nanomed Nanobiotechnol* **3**, 197–211 (2011).
34. Babincová, N. *et al.* Applications of magnetoliposomes with encapsulated doxorubicin for integrated chemotherapy and hyperthermia of rat C6 glioma. *Zeitschrift fur Naturforschung - Section C Journal of Biosciences* **73**, 265–271 (2018).
35. Hamaguchi, S. *et al.* Selective hyperthermia using magnetoliposomes to target cervical lymph node metastasis in a rabbit tongue tumor model. *Cancer Sci* **94**, 834–839 (2003).
36. Le, B. *et al.* Preparation of tumor-specific magnetoliposomes and their application for hyperthermia. *Journal of Chemical Engineering of Japan* **34**, 66–72 (2001).
37. Shinkai, M. *et al.* Targeting hyperthermia for renal cell carcinoma using human MN antigen-specific magnetoliposomes. *Japanese Journal of Cancer Research* **92**, 1138–1146 (2001).
38. Lu, Y., Sun, W. & Gu, Z. Stimuli-responsive nanomaterials for therapeutic protein delivery. *Journal of Controlled Release* vol. 194 1–19 Preprint at <https://doi.org/10.1016/j.jconrel.2014.08.015> (2014).
39. Li, L. *et al.* Triggered content release from optimized stealth thermosensitive liposomes using mild hyperthermia. *Journal of Controlled Release* **143**, 274–279 (2010).
40. Tannock2, I. F. & Hot, D. *Acid PH in Tumors and Its Potential for Therapeutic Exploitation1*. <http://aacrjournals.org/cancerres/article-pdf/49/16/4373/2435947/cr0490164373.pdf>.

41. Author, H., Yatvin, M. B., Weinstein, J. N., Dennis, W. H. & Blumenthal, R. *Design of Liposomes for Enhanced Local Release of Drugs*. Source: *Science, New Series* vol. 202 (1978).
42. Motamarry, A., Asemani, D. & Haemmerich, D. Thermosensitive Liposomes. in *Liposomes* (InTech, 2017). doi:10.5772/intechopen.68159.
43. Rana, A., Adhikary, M., Singh, P. K., Das, B. C. & Bhatnagar, S. “Smart” drug delivery: A window to future of translational medicine. *Frontiers in Chemistry* vol. 10 Preprint at <https://doi.org/10.3389/fchem.2022.1095598> (2023).
44. Enzian, P., Kleineberg, N., Kirchert, E., Schell, C. & Rahmanzadeh, R. Light-Induced Liposomal Drug Delivery with an Amphiphilic Porphyrin and Its Chlorin and Bacteriochlorin Analogues. *Mol Pharm* (2024) doi:10.1021/acs.molpharmaceut.3c00749.
45. Peng, T., Xu, W., Li, Q., Ding, Y. & Huang, Y. Pharmaceutical liposomal delivery—specific considerations of innovation and challenges. *Biomaterials Science* vol. 11 62–75 Preprint at <https://doi.org/10.1039/d2bm01252a> (2022).
46. Aleandri, S. & Mezzenga, R. The physics of lipidic mesophase delivery systems. *Phys Today* **73**, 38–44 (2020).
47. Zabara, A. *et al.* Design of ultra-swollen lipidic mesophases for the crystallization of membrane proteins with large extracellular domains. *Nat Commun* **9**, (2018).
48. Kim, H., Song, Z. & Leal, C. Super-swelled lyotropic single crystals. *Proc Natl Acad Sci U S A* **114**, 10834–10839 (2017).
49. Tyler, A. I. I. *et al.* Electrostatic swelling of bicontinuous cubic lipid phases. *Soft Matter* **11**, 3279–3286 (2015).
50. Elzenaty, O., Luciani, P. & Aleandri, S. A lipidic mesophase with tunable release properties for the local delivery of macromolecules: the apoferritin nanocage, a case study. *J Mater Chem B* (2022) doi:10.1039/d2tb00403h.
51. Negrini, R., Fong, W. K., Boyd, B. J. & Mezzenga, R. PH-responsive lyotropic liquid crystals and their potential therapeutic role in cancer treatment. *Chemical Communications* **51**, 6671–6674 (2015).

52. Aleandri, S., Speziale, C., Mezzenga, R. & Landau, E. M. Design of Light-Triggered Lyotropic Liquid Crystal Mesophases and Their Application as Molecular Switches in 'On Demand' Release. *Langmuir* **31**, 6981–6987 (2015).

Chapter 3. Environmental Concerns in Textile Industry

3. Environmental Challenges in Textile Production: From Fiber to Fabric

The textile industry stands as one of the oldest sectors globally and serves as a significant source of income for developing nations. Besides the role of textile industry in generation of employment, the textile industry holds the second position globally in terms of environmental pollution rates. The textile manufacturing process is renowned for its extensive use of resources, including significant amounts of water, fuel, and various chemicals.¹

The textile industry's production chain starts with the conversion of natural fibers (primarily cotton and wool) and synthetic fibers (mainly nylon and polyester) into yarns and fabrics. Environmental impacts manifest right from the initial stage of production. In the case of natural fibers like cotton, the early production stages, involving the extraction of cotton from raw materials, play a significant role in environmental pollution. Cotton cultivation relies on agrochemicals, such as pesticides and fertilizers, which can adversely affect soil health, deplete fertility, and disrupt the natural balance of microorganisms.² Moreover, the extensive use of water in cotton farming raises environmental concerns, contributing to water scarcity in specific regions. Runoff from chemically treated fields exacerbates the problem by contaminating nearby water sources.

Concerning wool, conventional sheep farming introduces additional environmental challenges. The use of pesticides, insecticides, and chemical fertilizers is common, impacting both the environment and animal welfare.³ Intensive sheep farming requires significant water resources for the animals and to cultivate fodder. Furthermore, the methane produced by sheep during digestion contributes to the overall carbon footprint of wool production.³ On the synthetic side, nylon and

polyester, derived from petrochemicals,⁴ contribute to resource depletion and the environmental impact associated with oil and natural gas extraction.

Scouring and bleaching play pivotal roles in the textile wet processing, contributing to the cleanliness, brightness, and overall quality of fabrics. These essential processes are crucial for preparing textiles for subsequent dyeing or finishing treatments. Scouring focuses on the removal of impurities like natural waxes, oils, dirt, and contaminants from fibers or fabrics.⁵ By eliminating impurities, scouring enhances textile absorbency, ensuring better penetration of dyes and chemicals in subsequent processing steps. Scouring agents, typically alkaline substances such as caustic soda or sodium carbonate, are commonly used in this process.⁶ Concurrently, bleaching is employed to eliminate or lighten the natural color of textiles. Bleaching agents, such as hydrogen peroxide or sodium hypochlorite,⁷ are applied to achieve the desired color alteration. Both scouring and bleaching processes need elevated temperatures, contributing to high energy consumption, and involve substantial water usage for rinsing and washing out chemicals.^{8,9} The removal of impurities and color during these processes generates waste materials. In the dyeing phase, pigments are applied to fibers or fabric to introduce colors. Traditional dyeing processes often employ various chemicals, including synthetic dyes, fixing agents, and auxiliary chemicals. Unfortunately, the discharge of these chemicals into water bodies lead to water pollution, adversely affecting aquatic ecosystems and potentially posing risks to human health. Dyeing processes typically require significant amounts of water for rinsing and washing,¹⁰ and they often demand high temperatures (around 100°C)¹¹ and energy-intensive equipment. It's worth noting that some dyes may be toxic or pose health risks, adding another layer of concern to the environmental impact of the dyeing process.

With pressing issues such as climate change, resource scarcity, stringent regulatory frameworks, and a growing demand for sustainable textiles, addressing the environmental impact of textile production has become an urgent imperative.

3.1 The APEOs Issue

Alkylphenol Ethoxylates (APEOs) are a group of non-ionic surfactants that have been widely used in various industrial processes, including the textile industry. These compounds consist of an alkyl chain attached to a phenolic ring, and they are often employed as detergents, emulsifiers, and wetting agents due to their effective surface-active properties.^{12,13}

Despite their utility in industrial applications, APEOs have raised significant environmental concerns. Approximately 60–65% of the total production of these compounds is believed to be introduced into the aquatic environment, mainly through discharges from industrial and municipal wastewater.¹⁴ APEOs can bioaccumulate in the tissues of aquatic organisms,^{15,16} leading to potential magnification of their harmful effects through the food chain. Furthermore, octylphenol ethoxylate (OPEO) and nonylphenol ethoxylate (NPEO) degrade into octylphenol (OP) and nonylphenol (NP), that have been identified as endocrine disruptors (affecting hormonal balance in aquatic organisms and potentially posing risks to ecosystems)¹³ in addition to their well-known estrogenic potential.^{17–20} APEOs metabolites are able to interact with the nervous system,^{21,22} influencing cognitive functions,^{23,24} and causing inflammation, cell damage or apoptosis.¹³ It has also been shown that the immune response of lymphocytes and macrophages can be affected by NP.²⁵

Recognizing the environmental risks, several countries and regions have implemented regulations restricting or banning the use of APEOs in various industries. In the European Union, according to the REACH regulation (Registration, Evaluation, Authorization and Restriction of Chemicals), OPEO and NPEO are classified as substance of very high concern.¹³ Since 1998, the use of APEOs in detergents has been prohibited in Germany and a ban in the use of surfactants in laundry detergents was imposed in Switzerland.²⁶ Furthermore, in January 2005,

the EU directive 2003/53/EG has imposed restrictions on the use of NPEOs, prohibiting concentrations exceeding 0.1% in formulations.¹³ Despite being forbidden in the EU, numerous companies have production sites or suppliers located outside Europe where the use of OPEOs is not restricted.

From the perspective of water and wastewater treatment, there are currently no suitable methods developed to address these contaminants on an urban or industrial scale. During the last decade, though, several wastewater treatment methods were reported and used for the attempted removal of APEOs.

- *Membrane-based processes.*²⁷⁻²⁹ These processes leverage semipermeable membranes to selectively separate and concentrate contaminants. Reverse osmosis, ultrafiltration and nanofiltration are the most commonly employed membrane-based methods for APEOs removal. Their remarkable advantages are the high quality of effluent from a chemical point of view and the potential to reuse the wastewater. Membrane degradation and high operating costs are the main disadvantages.
- *Biological treatments.*²⁹⁻³¹ Microorganisms, such as bacteria and fungi (which form a suspension known as activated sludge), break down APEOs and organic pollutants into simpler and less harmful substances through metabolic processes. Air or oxygen is continuously pumped into the tanks to create aerobic condition needed by the microorganisms in the activated sludge. While the process is effective, its main drawbacks include high energy consumption for aeration, the challenge of maintaining optimal microbial conditions, and the proper handling and disposal of excess sludge.
- *Chemical treatments.*^{29,32} The use of advanced oxidation process, involving the addition or creation of a highly oxidizing species to degrade the organic matter, has been used for the removal of APEOs from wastewater. Strong oxidizing agents such as hydrogen peroxide or ozone are capable of

breaking down APEOs into simpler, less harmful substances through chemical reactions that introduce oxygen atoms. The Fenton's reagent, that includes a mixture of iron salts (Fe^{2+} or Fe^{3+}) and hydrogen peroxide, produces hydroxyl radicals, which react with APEOs to break them down into simpler compounds. Chemical oxidation processes are effective treatment method, but it comes with certain disadvantages: they can generate byproducts, and the nature of these byproducts may vary depending on the oxidizing agent used. The cost of purchasing and handling strong oxidizing agents can be relatively high.

Novel solutions are required to address the removal of APEOs, not only from water but also from actual wastewater. These solutions should be chemically efficient, technically feasible, economically viable, and ecologically friendly.

3.2 The Dyes Issue

Dyes, whether natural or synthetic, impart color to various fibers employed in industries such as textile, pharmaceutical, food, cosmetic, plastic, photographic, paper, and more.³³ Colorants can exist as pigments or dyes. Pigments are largely insoluble, with particle sizes ranging from 1–2 μm ; in contrast, dyes readily dissolve in water and exhibit particle sizes ranging from 25 nm – 1.0 μm .³⁴

Dyes exhibit light absorption within the visible spectrum (400–700 nm) and possess extended conjugation along with one or more chromophores.³⁵ Chromophores, including heteroatoms like N, O, and S, consist of bonds such as: $-\text{N}=\text{N}-$, $=\text{C}=\text{O}$, NO or $\text{N}-\text{OH}$, $-\text{NO}_2$ or $\text{NO}-\text{OH}$, and $\text{C}=\text{S}$.³⁶ These unsaturated chromophore groups consist of atoms or atom groups where the arrangement of successive single and double bonds resonates, facilitating the absorption of light rays.³⁷ In addition to the action of electron acceptors, there are groups known as auxochromes that act as electron donors, typically located on the opposite side of the molecule.³⁸ Their

primary function is to intensify the color, and the fundamental meaning of the term “auxochrome” is a color enhancer. Examples of auxochrome groups include -NH_2 , -COOH , HSO_3^- , and -OH . These groups also possess the significant characteristic of enhancing the affinity for the fiber.

Approximately 20% of the dyes utilized in textile fiber dyeing remain unfixed, leading to their disposal in wastewater, resulting in considerable pollution.³⁹ The environmental impact, however, is not only contingent on the quantity of dye discharged; it also depends on the mixture of dyes with other substances in the effluent, all of which possess toxic properties.⁴⁰

Wastewater containing dyes at levels below 1 ppm, when released into surface or groundwater bodies, induces a reduction in dissolved oxygen concentration in water.⁴¹ This discharge contributes to elevated values of various physicochemical and biological parameters, including chemical oxygen demand, biochemical oxygen demand, total nitrogen, total phosphorus, and non-biodegradable organic compounds.⁴² Additionally, the wastewater exhibits fluctuating pH levels and contains heavy metals such as Cr, Ar, and Zn.³⁷

Synthetic dyes, generally non-biodegradable due to their inherent chemical properties and structure, exhibit adverse effects on the environment.⁴³ In addition, most synthetic dyes are recalcitrant, carcinogenic, and toxic to ecosystems.⁴⁴

Dyes may persist for extended periods, approximately 50 years or more, in the environment.³⁶ The persistence of dyes is closely tied to their chemical reactivity, with unsaturated compounds exhibiting lower persistence than saturated ones. The persistence of aromatic compounds increases with the number of chemical and halogen substitutions, highlighting the importance of evaluating the degradation of dyestuffs individually and in combination.

The predominant dye class in use belongs to the azo category.³⁷ Azo dyes (-N=N-), extensively studied for their applications and negative effects, exhibit toxicity ranging from 60% to 70%, with many being carcinogenic and resistant to

conventional physicochemical treatments.³⁷ The toxicity of azo dyes is attributed to their chemical reduction, leading to the formation of aromatic amines, such as benzidine, dimethoxy-benzidine, and dimethyl-benzidine. These aromatic amines pose a health risk due to their metabolic oxidation, generating electrophilic reductive intermediaries (diazonium salts) that can covalently bind to DNA, resulting in mutagenic properties and diseases such as cancer. A variation of this mechanism involves the chemical reduction of certain azo bonds in specific dyes to form toxic aromatic mono-azo amines.⁴⁵⁻⁴⁷ When azo ionic dyes are released in wastewater, they can adhere to suspended organic matter through electrostatic interactions, binding to sediments or wastewater sludge and thereby increasing their persistence.⁴⁸ Moreover, the contact of colored water or contaminated sludge with aquatic animals can transfer toxic compounds through the food chain to humans, leading to health disorders such as hypertension, cramps, nausea, bleeding, ulceration of the skin or membranes, and mucous membrane disorders. Depending on exposure doses, crucial damages to the kidney, reproductive system, liver, brain, and central nervous system may occur.^{45,47} The methods employed for removing dyes from wastewater are identical to those already addressed in the preceding paragraph.

3.3 Bibliography

1. Khan, W. U., Ahmed, S., Dhoble, Y. & Madhav, S. A critical review of hazardous waste generation from textile industries and associated ecological impacts. *Journal of the Indian Chemical Society* vol. 100 Preprint at <https://doi.org/10.1016/j.jics.2022.100829> (2023).
2. Tausif, M. *et al.* Cotton in the new millennium: advances, economics, perceptions and problems. *Textile Progress* **50**, 1–66 (2018).
3. Henry, B. *Understanding the Environmental Impacts of Wool: A Review of Life Cycle Assessment Studies*. (2012).
4. Slater, K. Environmental impact of polyester and polyamide textiles. in *Polyesters and Polyamides* 171–199 (Elsevier Ltd., 2008). doi:10.1533/9781845694609.1.171.
5. Environmental issues in Scouring of Wool. *Journal of Environmental Nanotechnology* **3**, 179–183 (2014).
6. Madhu, A. & Chakraborty, J. N. Developments in application of enzymes for textile processing. *Journal of Cleaner Production* vol. 145 114–133 Preprint at <https://doi.org/10.1016/j.jclepro.2017.01.013> (2017).
7. Cardamone, J. M. & Marmer, W. M. The whitening of textiles. in *Chemistry of the Textiles Industry* (1995).
8. Wang, S., Li, S., Zhu, Q. & Yang, C. Q. A novel low temperature approach for simultaneous scouring and bleaching of knitted cotton fabric at 60 °C. *Ind Eng Chem Res* **53**, 9985–9991 (2014).
9. Abdel-Halim, E. S. & Al-Deyab, S. S. One-step bleaching process for cotton fabrics using activated hydrogen peroxide. *Carbohydr Polym* **92**, 1844–1849 (2013).
10. Sarayu, K. & Sandhya, S. Current technologies for biological treatment of textile wastewater-A review. *Applied Biochemistry and Biotechnology* vol. 167 645–661 Preprint at <https://doi.org/10.1007/s12010-012-9716-6> (2012).
11. Khattab, T. A., Abdelrahman, M. S. & Rehan, M. Textile dyeing industry: environmental impacts and remediation. *Environmental Science and Pollution Research* vol. 27 3803–3818 Preprint at <https://doi.org/10.1007/s11356-019-07137-z> (2020).

12. Vega Morales, T., Torres Padrón, M. E., Sosa Ferrera, Z. & Santana Rodríguez, J. J. Determination of alkylphenol ethoxylates and their degradation products in liquid and solid samples. *TrAC - Trends in Analytical Chemistry* vol. 28 1186–1200 Preprint at <https://doi.org/10.1016/j.trac.2009.07.011> (2009).
13. Acir, I. H. & Guenther, K. Endocrine-disrupting metabolites of alkylphenol ethoxylates – A critical review of analytical methods, environmental occurrences, toxicity, and regulation. *Science of the Total Environment* vol. 635 1530–1546 Preprint at <https://doi.org/10.1016/j.scitotenv.2018.04.079> (2018).
14. Ahel, M., Giger, W. & Koch, M. *BEHAVIOUR OF ALKYLPHENOL POLYETHOXYLATE SURFACTANTS IN THE AQUATIC ENVIRONMENT-I. OCCURRENCE AND TRANSFORMATION IN SEWAGE TREATMENT.* ~ *Pergamon Wat. Res* vol. 28 (1994).
15. Ekelund, R., Bergman, ~, Granmo, A. & Berggren, M. *Bioaccumulation of 4-Nonylphenol in Marine Animals-A Re-Evaluation.* *Environmental Pollution* vol. 64 (1990).
16. Ahel, M. & Giger, W. *PARTITIONING OF ALKYLPHENOLS AND ALKYLPHENOL POLYETHOXYLATES BETWEEN WATER AND ORGANIC SOLVENTS.* *Chemosphere* vol. 26 (1993).
17. Nagao, T. *et al.* *Disruption of the Reproductive System and Reproductive Performance by Administration of Nonylphenol to Newborn Rats.* *Human & Experimental Toxicology* vol. 19 www.nature.com/het (2000).
18. Soto, A. M., Justicia, H., Wray, J. W. & Sonnenschein, C. *P-Nonyl-Phenol: An Estrogenic Xenobiotic Released from 'Modified' Polystyrene.* *Environmental Health Perspectives* vol. 92 (1991).
19. Preuss, T. G. *et al.* Nonylphenol isomers differ in estrogenic activity. *Environ Sci Technol* **40**, 5147–5153 (2006).
20. De Weert, J. *et al.* Bioavailability and biodegradation of nonylphenol in sediment determined with chemical and bioanalysis. *Environ Toxicol Chem* **27**, 778–785 (2008).
21. Couderc, M. *et al.* Neurodevelopmental and behavioral effects of nonylphenol exposure during gestational and breastfeeding period on F1 rats. *Neurotoxicology* **44**, 237–249 (2014).

22. Jie, Y. *et al.* Mechanism of nonylphenol-induced neurotoxicity in F 1 rats during sexual maturity. *Wien Klin Wochenschr* **128**, 426–434 (2016).
23. Kazemi, S. *et al.* The correlation between nonylphenol concentration in brain regions and resulting behavioral impairments. *Brain Res Bull* **139**, 190–196 (2018).
24. Mao, Z., Zheng, Y. L. & Zhang, Y. Q. Behavioral impairment and oxidative damage induced by chronic application of nonylphenol. *Int J Mol Sci* **12**, 114–127 (2011).
25. Lee, J. W., Han, H. K., Park, S. & Moon, E. Y. Nonylphenol increases tumor formation and growth by suppressing gender-independent lymphocyte proliferation and macrophage activation. *Environ Toxicol* **32**, 1679–1687 (2017).
26. Renner, R. *European Bans on Surfactant Trigger Transatlantic Debate*. <https://pubs.acs.org/sharingguidelines> (1997).
27. Kiso, Y., Kon, T., Kitao, T. & Nishimura, K. *Rejection Properties of Alkyl Phthalates with Nanofiltration Membranes*. *Journal of Membrane Science* vol. 182 (2001).
28. Agenson, K. O., Oh, J. I. & Urase, T. Retention of a wide variety of organic pollutants by different nanofiltration/reverse osmosis membranes: Controlling parameters of process. *J Memb Sci* **225**, 91–103 (2003).
29. Priac, A. *et al.* Alkylphenol and alkylphenol polyethoxylates in water and wastewater: A review of options for their elimination. *Arabian Journal of Chemistry* vol. 10 S3749–S3773 Preprint at <https://doi.org/10.1016/j.arabjc.2014.05.011> (2017).
30. Maki, H., Masuda, N., Fujiwara, Y. & Fujita, M. *Degradation of Alkylphenol Ethoxylates by Pseudomonas Sp. Strain TROI*. *APPLIED AND ENVIRONMENTAL MICROBIOLOGY* <https://journals.asm.org/journal/aem> (1994).
31. Staples, C. A., Naylor, C. G., Williams, J. B. & Gledhill, W. E. Ultimate biodegradation of alkylphenol ethoxylate surfactants and their biodegradation intermediates. *Environ Toxicol Chem* **20**, 2450–2455 (2001).

32. Palmer, M. & Hatley, H. The role of surfactants in wastewater treatment: Impact, removal and future techniques: A critical review. *Water Research* vol. 147 60–72 Preprint at <https://doi.org/10.1016/j.watres.2018.09.039> (2018).
33. Drumond Chequer, F. M. *et al.* Textile Dyes: Dyeing Process and Environmental Impact. in *Eco-Friendly Textile Dyeing and Finishing* (InTech, 2013). doi:10.5772/53659.
34. Torres, F. A. E. *et al.* Natural colorants from filamentous fungi. *Applied Microbiology and Biotechnology* vol. 100 2511–2521 Preprint at <https://doi.org/10.1007/s00253-015-7274-x> (2016).
35. Kuenemann, M. A. *et al.* Weaver's historic accessible collection of synthetic dyes: A cheminformatics analysis. *Chem Sci* **8**, 4334–4339 (2017).
36. Pereira, L. & Alves, M. Dyes-environmental impact and remediation. in *Environmental Protection Strategies for Sustainable Development* 111–162 (Springer Netherlands, 2012). doi:10.1007/978-94-007-1591-2_4.
37. Berradi, M. *et al.* Textile finishing dyes and their impact on aquatic environs. *Heliyon* vol. 5 Preprint at <https://doi.org/10.1016/j.heliyon.2019.e02711> (2019).
38. Gürses, A., Açıkyıldız, M., Güneş, K. & Gürses, M. S. Dyes and Pigments: Their Structure and Properties. in 13–29 (2016). doi:10.1007/978-3-319-33892-7_2.
39. Kant, R. Textile dyeing industry an environmental hazard. *Nat Sci (Irvine)* **04**, 22–26 (2012).
40. Weisz, A., Milstein, S. R., Scher, A. L. & Hepp, N. M. Colouring Agents in Cosmetics: Regulatory Aspects and Analytical Methods. in *Analysis of Cosmetic Products: Second Edition* 123–157 (Elsevier, 2018). doi:10.1016/B978-0-444-63508-2.00007-2.
41. Golka, K., Kopps, S. & Myslak, Z. W. Carcinogenicity of azo colorants: Influence of solubility and bioavailability. *Toxicology Letters* vol. 151 203–210 Preprint at <https://doi.org/10.1016/j.toxlet.2003.11.016> (2004).
42. Ali, H. Biodegradation of synthetic dyes - A review. *Water, Air, and Soil Pollution* vol. 213 251–273 Preprint at <https://doi.org/10.1007/s11270-010-0382-4> (2010).

43. Husain, Q. Potential applications of the oxidoreductive enzymes in the decolorization and detoxification of textile and other synthetic dyes from polluted water: A review. *Critical Reviews in Biotechnology* vol. 26 201–221 Preprint at <https://doi.org/10.1080/07388550600969936> (2006).
44. Aghaie-Khouzani, M., Forootanfar, H., Moshfegh, M., Khoshayand, M. R. & Faramarzi, M. A. Decolorization of some synthetic dyes using optimized culture broth of laccase producing ascomycete *Paraconiothyrium variabile*. *Biochem Eng J* **60**, 9–15 (2012).
45. Sarayu, K. & Sandhya, S. Current technologies for biological treatment of textile wastewater-A review. *Applied Biochemistry and Biotechnology* vol. 167 645–661 Preprint at <https://doi.org/10.1007/s12010-012-9716-6> (2012).
46. Varjani, S., Rakholiya, P., Ng, H. Y., You, S. & Teixeira, J. A. Microbial degradation of dyes: An overview. *Bioresource Technology* vol. 314 Preprint at <https://doi.org/10.1016/j.biortech.2020.123728> (2020).
47. Sarkar, S., Banerjee, A., Halder, U., Biswas, R. & Bandopadhyay, R. Degradation of Synthetic Azo Dyes of Textile Industry: a Sustainable Approach Using Microbial Enzymes. *Water Conservation Science and Engineering* vol. 2 121–131 Preprint at <https://doi.org/10.1007/s41101-017-0031-5> (2017).
48. Soriano, J. J., Mathieu-Denoncourt, J., Norman, G., de Solla, S. R. & Langlois, V. S. Toxicity of the azo dyes Acid Red 97 and Bismarck Brown Y to Western clawed frog (*Silurana tropicalis*). *Environmental Science and Pollution Research* **21**, 3582–3591 (2014).

Chapter 4. Techniques for Comprehensive Characterization

4. Introduction to Experimental Techniques

In this chapter, the main experimental techniques used in this thesis are introduced, with brief explanations of their fundamental principles.

4.1 Dynamic Light Scattering

The Dynamic Laser Light-Scattering (DLS) method, also known as photon correlation spectroscopy, is a non-invasive technique used to measure the size and size distribution of particles in a solution.¹ The technique is based on the Brownian motion of dispersed particles: when they are dispersed in a liquid, they move randomly in all directions because of the collision with solvent molecules. These collisions cause a certain amount of energy to be transferred, which induces particle movement. The energy transfer is more or less constant and therefore has a greater effect on smaller particles. As a result, smaller particles are moving at higher speeds than larger particles. The relation between the speed of the particles and the particle size is given by the Stokes-Einstein equation:

$$D = \frac{K_B T}{6\pi\eta r}$$

where D is the translational diffusion coefficient (which represent speed of the particles), K_B is the Boltzmann constant (1.38×10^{-23} J/K), T is the absolute temperature in Kelvin, η is the dynamic viscosity of the fluid, and r is hydrodynamic radius of the particle. The time depending fluctuation of the intensity of the scattered light can be expressed by the experimental correlation function:

$$g(q, \tau) = \frac{\langle I(q, t) I(q, t + \tau) \rangle}{\langle I(q, t) \rangle^2}$$

where q is equal to $\text{sen}(\theta/2)$, being θ the scattering angle (the angle at which the light is collected). This function represents the average of the product of the signal at time t (the number of photon counted by the detector) for the signal at time $t + \tau$, varying as a function of τ . For ranges of time comparable to those of a particle diffusion g is proportional to the diffusion coefficient, according to the relation:

$$g(q, \tau) \propto 1 + e(-Dq^2\tau)$$

Hence, the variations in the intensity of the scattered light are linked to the rate of particle diffusion within and out of the studied region, and the data can be analyzed to derive diffusion coefficients for the particles causing the scattering. In the presence of multiple species in the solution, a distribution of diffusion coefficients is observed. These motion data are conventionally processed to obtain a size distribution for the sample, where the size is represented by the "Stokes radius" or "hydrodynamic radius" of the particle.

Through scattering experiments, it becomes feasible to estimate the hydrodynamic radius of particles in the nanometer to micrometer range in solution. This hydrodynamic radius is influenced by both particle mass and shape, as well as the number of solvation molecules. Consequently, it may differ significantly from the actual size of the system under investigation. Nevertheless, DLS experiments are highly valuable for determining changes in particle diameter over time. In the exploration of aggregates like micelles and liposomes, this technique provides an estimation of their size and enables the monitoring of phase transition processes such as micelle-liposome transition, vesicle fusion, and aggregate destruction.

4.2 Electrophoretic Mobility

The zeta potential (ζ) of a particle is a physical property exhibited by any particle in suspension and represents the overall charge that the particle acquires in a

particular medium.² The development of a net charge at the colloidal surface affects the distribution of ions in the surrounding interfacial region, resulting in an increased concentration of counter ions close to the surface. Thus, an electrical double layer exists round each particle. The liquid layer surrounding the particle is divided into two regions: an inner segment known as the Stern layer, where ions are strongly bound, and an outer (slipping) region where their association is less firm. Within the diffuse layer, a conceptual boundary is established, inside which ions and particles create a stable entity. As the particle undergoes movement, such as due to gravity, the ions within this boundary move along with it, while those beyond the boundary remain in the bulk dispersant. The potential at this boundary, identified as the surface of hydrodynamic shear, is defined as ζ (Figure 1).

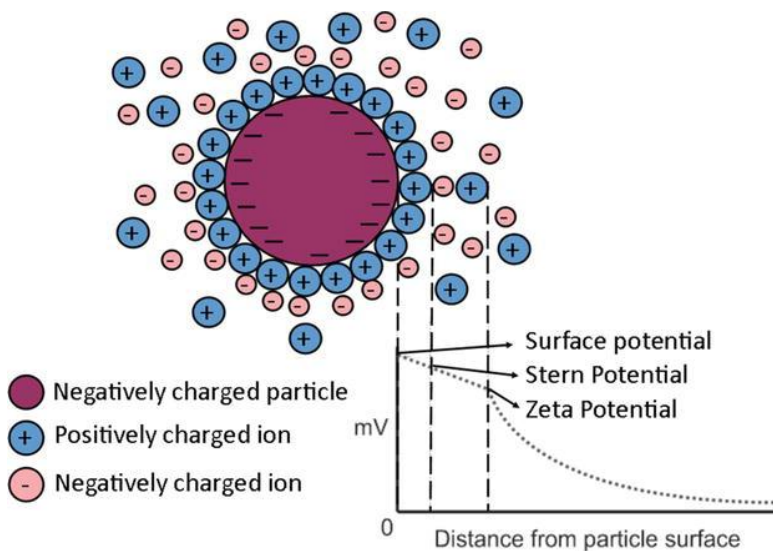


Figure 1. A schematic representation of ζ .

The presence of electrical charges on the surface of particles leads to their interaction with an applied electric field, collectively termed electrokinetic effects. When an electric field is applied across an electrolyte, charged particles

suspended in the electrolyte are attracted toward the electrode of opposite charge. Viscous forces acting on the particles tend to oppose this movement. When equilibrium is achieved between these opposing forces, the particles move with a constant velocity. The velocity depends on the strength of the electric field or voltage gradient, the dielectric constant of the medium, the viscosity of the medium, and the zeta potential. The velocity of a particle in a unit electric field is referred to as its electrophoretic mobility. ζ is related to the electrophoretic mobility by the Henry equation:

$$U_E = \frac{2 \varepsilon \zeta f(\kappa a)}{3\eta}$$

where U_E is the electrophoretic mobility, ζ is the zeta potential, ε is the dielectric constant, η is the viscosity and $f(\kappa a)$ is the Henry's function. The units of κ , called the Debye length, are reciprocal length and κ^{-1} is often taken as a measure of the thickness of the electrical double layer. The parameter 'a' refers to the radius of the particle and therefore κa measures the ratio of the particle radius to electrical double layer thickness. Electrophoretic assessments of zeta potential are commonly conducted in aqueous solutions with moderate electrolyte concentrations. In this scenario, $f(\kappa a)$ equals 1.5, known as the Smoluchowski approximation.

The electrophoretic mobility of colloidal dispersions is determined through microelectrophoresis, a technique involving the application of voltage across electrodes positioned at the ends of a cell containing the particle dispersion. Charged particles migrate toward the oppositely charged electrode, and their velocity is measured and quantified in unit field strength as their mobility. This measurement relies on the principles of Laser Doppler electrophoresis. Combining the frequencies of the scattered and reference beams results in a modulated beam, characterized by constructive and destructive effects, leading to a much

smaller, measurable frequency. The magnitude of the Doppler shift is determined by comparing the beat frequency with a reference frequency, utilizing optical mixing or interferometric techniques. The Doppler shift analysis can be conducted through Phase Analysis Light Scattering (PALS), which employs the same optical setup as conventional laser Doppler electrophoresis but employs a different signal processing method than the commonly used Fourier transformation. Instead of measuring the frequency shift, PALS determines the phase shift, which is proportional to the change in the particles' position.

4.3 X-ray Diffraction

X-ray diffraction (XRD) is a versatile non-destructive analytical technique used to analyze structural properties in ordered materials, such as phase composition, crystal structure and orientation of powder, solid and liquid samples.³ X-rays are highly penetrating electromagnetic radiation with wavelengths spanning between 0.1 Å and 100 Å, typically similar to the interatomic distances in a crystal. An X-ray photon interacting with a sample will be either transmitted (simply by not interacting with the matter and continuing along its original direction), or scattered by the electrons of the atoms in the material. The scattered waves, emitted in multiple directions, may interfere with each other. The nature of interference can be constructive or destructive, based on the direction and type of interaction of the photons, meaning that the ordered arrangement of atomic structures in solids may cause constructive interference. There is a strong correlation between materials structure periodicity and electromagnetic waves diffraction, namely that short-range periodicity is associated with higher diffraction angles, and conversely, long range periodicity is correlated to lower diffraction angles.

In order to obtain readable data from this phenomenon, monochromatic radiation is mandatory. A simple explanation that was proposed by W. H. Bragg in

1913: according to his analysis, the atomic planes of crystals are assumed to be in layers. A distance d separates these layers, as shown in Figure 2, and collision of incident X-rays on these atomic planes produces in phase reflection. At the lattice planes, the angle between the incident beam and the equivalent diffracted wave remains equal. Being diffraction a constructive interference of scattered waves, when path difference lengths become equal to $n\lambda$, Bragg's diffraction conditions are satisfied.

The general relationship between the wavelength of the incident X-rays, angle of incidence, and spacing between the crystal lattice planes of atoms, is known as Bragg's Law, expressed as:

$$n\lambda = 2d\sin(\theta)$$

where n is an integer number, λ is the X-rays wavelength, d denotes spacing between atomic planes, and θ represents diffraction beam angle.

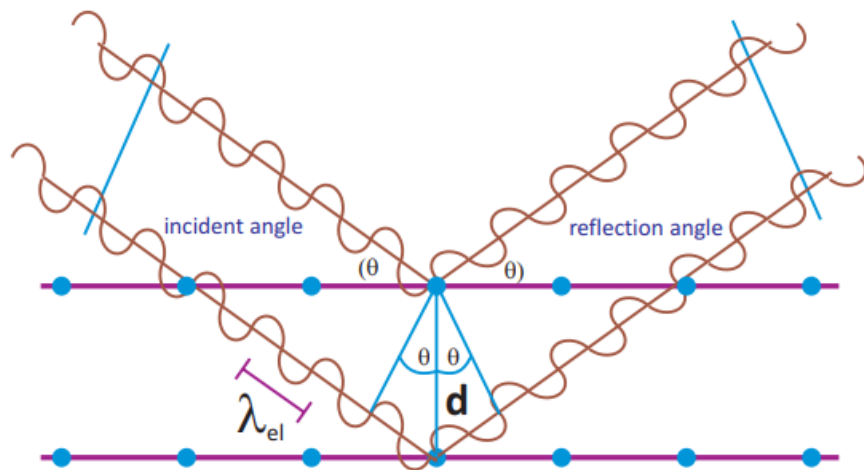


Figure 2. Principles of X-ray Diffraction.

XRD is employed for determining the type of crystalline phase, crystallinity degree and orientation, chemical nature of the compound (in comparison to a known standard), and size of the crystallites. Sharp and broad diffraction peaks are

observed for crystalline and amorphous materials, respectively, with smaller crystallites producing broader diffraction peaks.

4.4 Small Angle X-ray Scattering

In an X-ray scattering experiment, a sample is exposed to an incident X-ray beam. Due to the interaction between X-ray photons and atoms in the sample, a portion of the incident radiation is scattered at various angles. Elastic scattering, occurring when there is no energy exchange between the incident X-ray photon and the sample, ensures that the scattered radiation maintains the same energy as the incident radiation. Some X-ray photons will be deflected or scattered at different angles to the incident X-ray radiation. By measuring the scattering angle and intensity of the X-ray radiation, information on the structural features of the sample can be recovered, such as particle sizes and distributions or the degree of disorder. Small Angle X-ray Scattering (SAXS) refers specifically to measuring the elastically scattered X-rays at small angles ($0.1 - 10^\circ$).^{4,5} This angular range gives information on pore diameters, characteristic distances of partially ordered materials and the shape and size of macromolecules. The setup of a SAXS experiment is conceptually simple: the sample is subjected to a monochromatic X-ray beam, with the majority of X-rays crossing the sample without interaction. A fraction of the emitted X-ray photons interacts with the electrons of atoms within the sample, leading to elastic dispersion. This elastic scattering of photons results in small vector changes while maintaining their kinetic energy and wavelength. Then, a scattering pattern is obtained by a flat X-ray detector placed on the sample's other side from the X-ray emitter, which can be utilized to deduce details about the structure of the sample.

4.5 Wide Angle X-ray Scattering

Wide Angle X-ray Scattering (WAXS) is a technique used for the investigation of crystalline and partially ordered materials down to their atom-atom spacing.⁵ This technique specifically refers to the analysis of Bragg peaks scattered to wide angles ($2\theta > 5^\circ$), which by Bragg's law implies that they are caused by sub nanometer-sized structures. As a technique that is complementary to SAXS, WAXS extends the length scale at which a sample can be investigated, that is down to interatomic distances.

The intensity of the d -space pattern is directly proportional to the number of electrons (atoms) in the imaginary planes. Every crystalline solid has a unique pattern of d -spacings (known as the powder pattern), which is a fingerprint for that solid. Solids with the same chemical composition but different phases can be identified by their pattern of d -spacings.

4.6 X-ray Photoelectron Spectroscopy

X-ray photoelectron spectroscopy (XPS) is an analytical technique, in which monochromatic X-ray photons hit the surface of a material and, if their energy is sufficient to displace a core electron from its energy level, that electron is expelled from the atom and its kinetic energy is measured.⁶ The technique is based on the photoelectric effect, first discovered by H. Hertz in 1887 that noticed that electrons were emitted from surfaces when irradiated with light. The fact that the probe of this technique are electrons, implies that we are dealing with a surface-sensitive technique. Indeed, due to the extremely short mean free path of electrons inside solids, only electrons coming from the first few nanometers beneath material surface will be able to be emitted and detected.

Emitted photoelectrons are the result of complete transfer of the x-ray energy to a core level electron. This is expressed mathematically in the equation:

$$h\nu = BE + KE + \Phi_{\text{spec}}$$

The equation simply states that the energy of the x-ray ($h\nu$) is equal to the binding energy (BE) of the electron (how tightly it is bound to the atom/orbital to which it is attached), plus the kinetic energy (KE) of the electron that is emitted, plus the spectrometer work function (Φ_{spec}), a constant value.

All the electrons with a lower binding energy with respect to the incident X-ray radiation energy should be emitted from the sample and detected with the XPS technique. The binding energy of an electron is a material property and it is independent of the X-ray source used to eject it.

The technique is powerful due to its surface sensitivity and its capability to provide information about the chemical state of elements within the sample (the technique can determine composition of material surfaces a few atomic layers thick). It can detect all elements except hydrogen and helium, making it applicable to the study of various materials, ranging from plastics and textiles to soil and semiconductors.

4.7 Magnetic Behavior and Alternating Gradient Force Magnetometer

The magnetic character of matter is typically established by measuring either the magnetization (M) or the magnetic susceptibility (χ). M is the total magnetic moment divided by the volume of the sample. An alternative parameter often used is the total magnetic moment divided by the mass. χ is a measure of how much a material will become magnetized in an applied magnetic field (H). Its definition, $\chi = M/H$, implies that materials with a positive magnetic susceptibility become magnetized in the same direction as the applied field, while those with a negative susceptibility become magnetized in the opposite direction.

There are several types of magnetic response, which classifies the materials accordingly. The most common are: paramagnetism, diamagnetism,

ferromagnetism, antiferromagnetism, and ferrimagnetism. An additional form of magnetism, of interest in our field, is superparamagnetism, which appears in sufficiently small ferromagnetic or ferrimagnetic nanoparticles.

The measure of susceptibility is more indicated for materials with a linear dependence between M and H , as its definition suggests. Paramagnetic materials have a weakly positive magnetic susceptibility, which means their magnetization slightly enhances the magnetic field. Paramagnetism arises from the presence of unpaired electrons in the material, which can align their spins only in presence of an external magnetic field. Examples of paramagnetic materials include a large number of compounds containing transition and rare-earth elements (such as salts), many metals such as aluminum and platinum and, among molecular substances, oxygen.

Diamagnetic materials have a negative magnetic susceptibility, which means their magnetization is in the opposite direction to the magnetizing field. The material possesses no permanent magnetic dipole moment, and in the presence of an external magnetic field, the orbital motion of electrons induces a weak magnetic response that opposes the applied field. All materials have a diamagnetic response, but this is overwhelmed when other forms of magnetism are present. Examples of diamagnetic materials include many insulating materials, few metals as copper, silver, and gold.

Ferromagnetic materials have a very high magnetic susceptibility, which means they can become strongly magnetized in the presence of an external magnetic field. Ferromagnetism arises from the interaction between the spins of the electrons in the material, which can spontaneously align to create a net magnetic moment. As a consequence, magnetization can even be present without an external field. In this case, susceptibility is not a characterizing quantity and it is better to use magnetization, instead. Examples of ferromagnetic materials include

iron, nickel, cobalt, some rare-earths , and many compounds containing these elements.

In antiferromagnetism, adjacent magnetic moments are aligned in opposite directions, resulting in a net zero magnetic moment for the material, in absence of an external magnetic field. Examples of antiferromagnetic materials include manganese oxide and chromium.

Ferrimagnetic materials have two or more types of magnetic moments that are aligned in opposite directions but are not equal in magnitude, resulting in a net magnetic moment. An example of a ferrimagnetic material is magnetite.

Superparamagnetism occurs in certain nanoscale magnetic materials, such as nanoparticles, which are either ferromagnetic or ferrimagnetic in bulk form, where thermal fluctuations can cause random reversals of magnetic moments. Unlike traditional ferromagnetism, superparamagnetic materials do not exhibit a permanent macroscopic magnetization, and an external magnetic field is needed to progressively align the magnetic moments.

The Alternating Gradient Force Magnetometer (AGFM) is a modification of the well-known Faraday balance.

The AGFM technique determines the magnetic moment of a sample by measuring the response of a magnetic sample to an applied magnetic field.⁷ The sample is positioned between the poles of an electromagnet that produces a primary uniform magnetic field. An additional set of coils creates a field gradient, resulting in a force experienced by the magnetic moments of the sample. The force exerted on the sample depends on its magnetic properties and the gradient of the magnetic field. Supplying alternating current to the coils, the field gradient oscillates, and so does the force exerted on the magnetic moments, causing the sample to oscillate as well. The amplitude of this oscillation is proportional to the magnetic moment of the sample and can be detected by a highly sensitive piezoelectric displacement sensor. By varying the strength of the primary applied

magnetic field, while keeping constant the field gradient, and measuring the resulting oscillation amplitude, the AGFM can determine the magnetization curve $M(H)$, of the sample.

4.8 N₂ Absorption-Desorption Studies

The Brunner-Emmett-Teller (BET) theory, employed for determining the surface area of solid or porous materials, provides crucial insights into their physical structure.⁸ The surface area of a material plays a significant role in influencing its interactions with the environment. Various properties, including dissolution rates, catalytic activity, moisture retention, and shelf life are frequently associated with the surface area of a material.

Using the BET theory involves determining specific surface area of materials, encompassing surface irregularities and pore walls, at an atomic level through the adsorption of an unreactive gas. Given the typically weak interaction between most gases and solids, the solid material necessitates cooling, often achieved using a cryogenic liquid. Throughout this process, the temperature of the solid sample remains constant, ensuring isothermal conditions, while the pressure or concentration of the adsorbing gas is systematically increased. As the gas pressure is increased, more and more molecules adsorb on the surface of the materials, and a thin layer will eventually cover the entire surface. The porosimeter is the instrument used to measure the adsorption of a gas by an adsorbent material. The number of gas molecules in the monolayer is recorded from the adsorbed volume. Since the cross-sectional area of the adsorbate is known, the area of the accessible surface may be calculated. However, gas adsorption as a function of pressure does not follow a simple linear relationship. Therefore, an appropriate mathematical model must be used to calculate the surface area: the BET equation (named after Brunauer, Emmett, and Teller who developed the theory).

$$\frac{1}{X\left[\left(\frac{P}{P_0}\right) - 1\right] + \frac{1}{X_m C} + \frac{C-1}{X_m C} \cdot \left(\frac{P}{P_0}\right)}$$

This equation describes the relationship between the number of gas molecules adsorbed (X) at a given relative pressure (P/P₀), where C is a second parameter related to the heat of adsorption. The BET equation strictly describes a linear plot of 1/[X(P₀/P)-1] vs P/P₀, which for most solids, using nitrogen as the adsorbate, is restricted to a limited region of the adsorption isotherm, usually in the P/P₀ range of 0.05 to 0.35.

The surface area (SA) of materials is calculated knowing the slope and intercept of the plot:

$$SA = \frac{1}{\text{slope} + \text{intercept}} \text{ CSA}$$

where CSA is the cross-sectional area of the adsorbate.

The BET model does not take into account the strong interaction between adsorbent and adsorbate and at the same time predicts a heterogeneous surface of infinite adsorption layers when the pressure equals the saturation pressure. Weak intermolecular forces are established between the various adsorbate gas molecules, but only the vertical direction, while horizontal interactions aren't considered.

4.9 Electron Microscopy

Under optimal lighting conditions, the human eye can differentiate between two points in space separated by 0.2 mm without the assistance of additional lenses. This separation distance is referred to as the resolving power or resolution of the eye. To amplify this capability, a lens, or a combination of lenses (as in a microscope) can be employed, allowing the eye to perceive points that are much closer together than 0.2 mm.

The resolving power of the microscope is not only limited by the number and quality of lenses but also by the wavelength of the light used for illumination. Microscope resolution can be described by the Rayleigh criterion:

$$\delta = \frac{0.61\lambda}{\mu\beta}$$

where δ is smallest resolvable distance, λ is incident wavelength, μ is the refractive index of viewing medium, and β is the diameter of the aperture (such as the objective lens in a microscope). Based on the Rayleigh equation, the smaller the λ , the better the resolving power of the optical system.

Visible light (employed by optical microscope) has wavelengths on the order of hundreds of nanometers, limiting the level of detail that can be resolved using traditional light microscopy. X-rays and γ -rays have much shorter wavelengths compared to visible light (which could theoretically provide extremely high resolution in imaging), but it's difficult to focus them using lenses, as these high-energy rays tend to penetrate matter rather than being refracted or diffracted. Electrons, having a wave-particle duality according to quantum mechanics, are characterized by a wavelength determined by the De Broglie equation:

$$\lambda = \frac{h}{m_0v}$$

where λ is the wavelength, h is the Planck constant, m_0 is the mass of the electron, and v is the velocity of the electron.

Electrons have much shorter wavelengths (on the scale of picometers) if compared to visible light, allowing for much higher resolution and the visualization of structures at the nanoscale. Electron microscopes, then, have a much higher resolving power than light microscopes and can reveal the structure of smaller objects. E. Ruska, a German engineer and academic professor, built the first electron microscope in 1931, and the same principles behind his prototype still govern modern instrumentation.

As the electron beam interacts with the sample, the beam undergoes energy loss through diverse mechanisms (Figure 3).

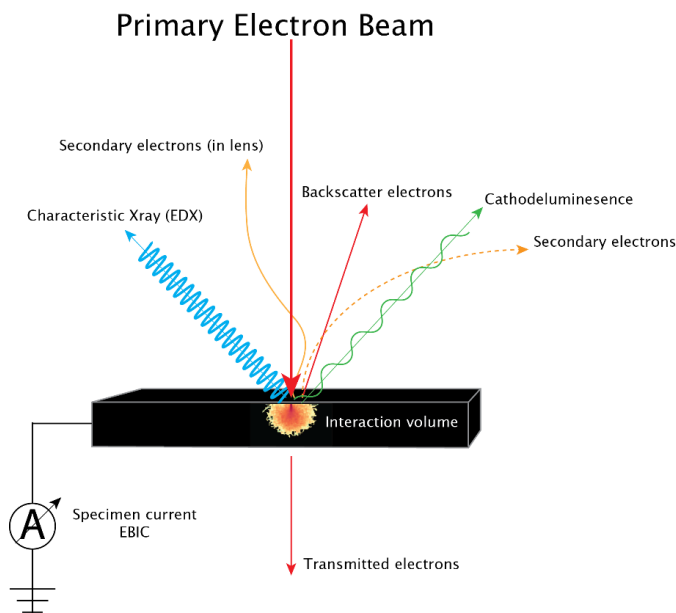


Figure 3. Possible interaction of the electron beam with the sample.

This dissipated energy transforms into different forms including heat; the release of low-energy secondary electrons, high-energy backscattered electrons, and Auger electrons; light emission (cathodoluminescence); or X-ray emissions. Each of these outcomes generates signals that convey valuable information about the surface properties of the sample, such as its topography and composition.

There are two types of electron microscopes, with different operating styles: Transmission Electron Microscope (TEM) and Scanning Electron Microscope (SEM).

4.9.1 TEM

TEM allows analyzing images with magnifications of up to 10 magnification zoom. With this technique, it becomes possible to observe the actual sizes of structures

that are beyond the reach of an optical microscope.⁹ A schematic representation of an instrument is illustrated in Figure 4.

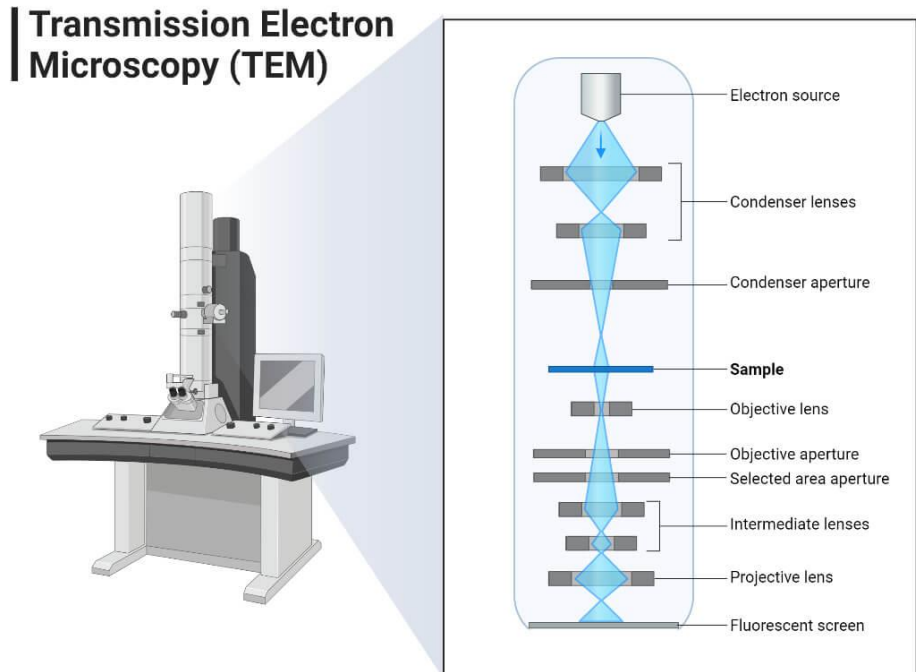


Figure 4. A schematic representation of a TEM instrument.

The fundamental components of TEM primarily include an electron source known as a gun or electron cannon. Typically, this source features a V-shaped filament made of lanthanum hexaboride or tungsten. An electric potential, positive to the anode, is applied. As a result, the filament, or cathode, heats up, leading to the generation of an electron current. The high energy electron beam is accelerated through an extremely thin sample, typically thinner than 100 nm. A series of electromagnetic lenses and apertures are placed throughout the microscope's column to focus the beam on the sample, and minimize distortions. Following this stage, the electron beam impacts the sample, undergoing various processes. During these processes, electrons that influence the sample disperse, preventing energy loss (elastic scattering). Additionally, there are other processes in which

electrons transfer some of their energy to internal electrons within the sample (inelastic scattering). Subsequently, the objective lens comes into play, focusing the scattered beams to create the initial image. This is achieved through a diffraction process facilitated by the projection lens, which enlarges the electron beam and reflects it onto the phosphor screen.

All the signals generated in the TEM either originate from elastic scattering or inelastic scattering. Elastic scattering events involve no energy transfer to the incident electrons. Two types of interactions with isolated atoms result in elastic scattering:

- interaction with the electron cloud results in low angle scattering;
- Coulombic attraction to the positively charged nucleus results in high angle (Rutherford) scattering.

Unlike elastic scattering, inelastic scattering is characterized by a measurable loss of energy to the incident electrons – on the order meV (1000 meV = 1 eV) up to several hundred eV, which represent a small fraction of the incident beam energy. Inelastic scatter generates energy-loss electrons, X-ray emission, secondary electron emission, and sometimes visible light emission (i.e., cathodoluminescence or CL). The two most popular inelastic signals analyzed in the TEM are energy-loss electrons measured via electron energy-loss spectroscopy (EELS), and characteristic X-rays detected with energy-dispersive X-ray spectroscopy (i.e., EDS or EDX spectroscopy).

4.9.2 SEM

SEM is a highly versatile technique used to obtain high-resolution images and detailed surface information of samples.¹⁰

A schematic representation of an instrument is illustrated in Figure 5.

Scanning Electron Microscopy (SEM)

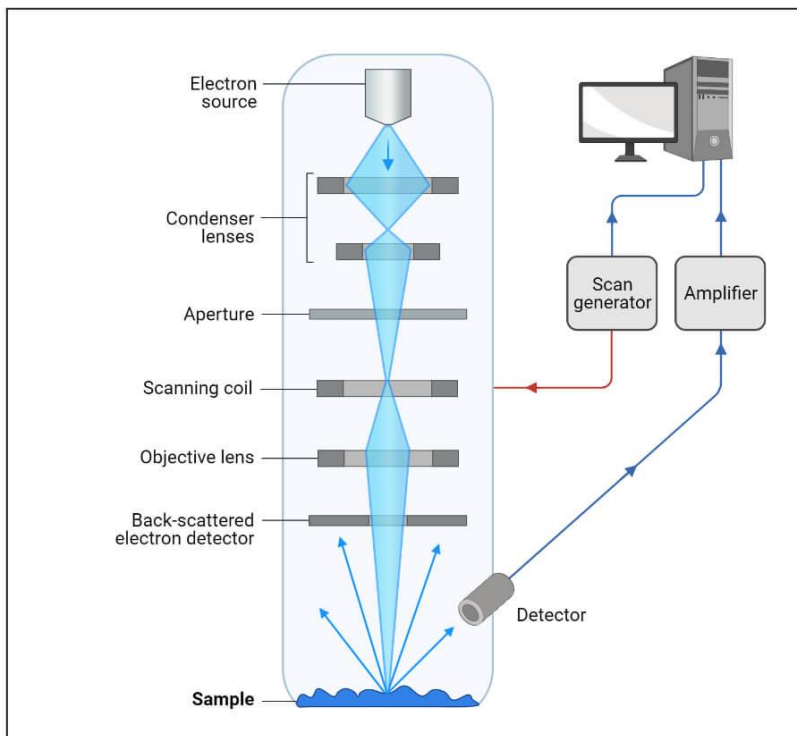


Figure 5. A schematic representation of a SEM instrument.

The electron source plays a pivotal role in the analytical performance of a SEM. Often known as the electron gun, this element must produce a brilliant and coherent flow of electrons, which can be intentionally dispersed onto the sample through lenses within the column. SEM commonly employ three widely recognized types of electron emitters: tungsten filaments, solid-state hexaboride crystals, and field emission guns. Electromagnetic lenses are used to manipulate the electron beam in an SEM. The main purpose of a condenser lens is to reduce the diameter of the primary beam that is emitted from the electron source.

In the experiment, a concentrated stream of electrons is concentrated across the surface of a sample at a specified accelerating voltage (1 keV – 30 keV), and electrons interact with the atoms in the sample, generating diverse signals that

can be used to obtain information about the surface's topography and composition.

The sample is positioned on a stage within the chamber, and both the column and the chamber are sustained in a vacuum through a combination of pumps. When the electron beam hits the surface of the sample, it penetrates the sample to a depth of a few microns, before interacting with atoms in the sample, generating a variety of signals including secondary electrons, backscattered electrons, and characteristic X-rays. The extent of the interaction volume will depend upon the accelerating voltage of the primary electrons and the density of the sample material. Low-density samples facilitate a tear-drop interaction volume whereas samples composed of heavier elements have a hemispherical interaction volume. Higher accelerating voltage results in a greater depth of penetration.

The most used signals in the SEM are secondary electrons, backscattered electrons, and characteristic X-rays, which are then detected by appropriate detectors.

Secondary electrons are predominantly employed for capturing topographical images as they originate in close proximity to the sample surface. These electrons are emitted through inelastic scattering, which involves energy transfer from a primary beam electron to an atom in the sample. Secondary electrons typically have energies below 50 eV. Images obtained with secondary electrons exhibit superior lateral resolution because of the relatively small interaction volume, which is approximately the size of the beam diameter.

At high angles ($> 90^\circ$), elastic scattering leads to the release of backscattered electrons above the sample surface. When the primary beam approaches the nucleus of an atom in the sample, the positive charge induces a deflection of the fast electron, causing it to be ejected from the surface. The production of backscattered electrons is influenced by the average atomic number, with heavier elements, having more positive charge, resulting in a higher yield. Consequently,

the contrast in images obtained with backscattered electrons offers insights into the surface composition.

Characteristic X-rays emerge when an ionized atom returns to its ground state by replenishing an electron hole in an inner shell with an electron from a higher orbital. The energy disparity between these two electron shells corresponds to the characteristic X-ray energy, enabling the identification of the specific element of origin. In contrast to backscattered electrons, characteristic X-rays resulting from inelastic scattering provide accurate identification of elements within the sample. Besides the characteristic X-ray peaks evident in EDS data, a continuum (background) signal arises due to the deceleration of incident electrons during their interaction with the sample.

Different detectors are needed to distinguish secondary electrons, backscattered electrons, or characteristic X-rays.

The maximum resolution obtained in an SEM depends on multiple factors including the electron beam spot size and interaction volume of the electron beam with the sample. While it cannot provide atomic resolution, some SEMs can achieve resolution below 1 nm.

Real-time visualization of images occurs on an external monitor through software that correlates the position of the electron beam with the intensity of electrons detected. The most common detectors employed are the secondary electron detector (SED) and the backscattered electron detector (BSD).

Secondary electrons (SEs) possess minimal energies, typically around 50 eV, restricting their mean free path within solid matter. As a result, these electrons can only escape from the top few nanometers of the surface of a sample. The signal generated by SEs tends to be concentrated precisely at the impact point of the primary electron beam. This characteristic enables the collection of high-resolution images of the sample surface, with a level of detail surpassing 1 nm.

Back-scattered electrons (BSEs) refer to electrons in the beam that are reflected from the sample through elastic scattering. Given their higher energy compared to SEs, BSEs originate from deeper regions within the specimen. As a result, the resolution of images obtained through BSEs is typically lower than those acquired using SEs.

4.10 Differential Scanning Calorimetry

Differential scanning calorimetry (DSC) is an experimental technique to measure the heat energy uptake or release that takes place in a sample during controlled increase (or decrease) in temperature.¹¹ As well as being used to characterize the thermal properties of a material, a differential scanning calorimeter is used to determine the temperature at which particular phase transitions occur, including phase transition temperature, fusion and crystallization events. At the simplest level it may be used to determine thermal transition temperatures for samples in solution, solid, or mixed phases (as suspensions). The advantages of calorimetric techniques are due to the fact that they are based on direct measurements of intrinsic thermal properties of the samples, are usually non-invasive and require no chemical modifications or extrinsic probes. Furthermore, with careful analysis and interpretation, calorimetric experiments can directly provide fundamental thermodynamic information about the processes involved. The output from any DSC experiment is a thermogram showing the excess heat capacity (C_p) as a function of temperature.

We can assume that the system of interest can exist in either two distinct states (A and B) over a finite temperature range; the equilibrium constant concentration can be written as: $K = a_B / a_A$

Thus, if the fractional occupancy of the state B, the higher enthalpy state, is denoted by f , then $f = K/(1 + K)$.

The standard Gibbs energy change for the reaction is given by:

$$\Delta G^\circ = \Delta H^\circ - T\Delta S^\circ = -RT\ln K,$$

where ΔH° and ΔS° are the standard enthalpy and entropy changes of the reaction. When ΔG° is close to zero, the system exists in a mixture of the two states. The temperature at which the two states are equally probable is the transition temperature, T_m . At this temperature the Gibbs energy difference between the two states is zero and $T_m = \Delta H^\circ/\Delta S^\circ$.

The integral under the curve obtained during a DSC experiment is equal to the enthalpy change for the transition from state A to state B (ΔH°), the T_m is approximately the temperature of C_p maximum and, since the T_m is equal to $\Delta H^\circ/\Delta S^\circ$, the entropy change for the transition can also be calculated.

Traditionally, the information derived from heat capacity curves has been limited to determination of ΔH° and ΔS° . However, the shape of the heat capacity curve also contains useful information about the transition.

The heat uptake during the transition depends on the amount of sample present in the active volume of the DSC cell and is a model-free absolute measure of the absolute enthalpy of the process involved.

4.11 Thermogravimetric Analysis

Thermogravimetric analysis (TGA) is a technique used to analyze the thermal properties of materials by monitoring changes in their weight as a function of temperature (or time) under controlled atmospheres. The temperature of the sample is gradually increased at a constant rate while its weight is continuously monitored. As the temperature increases, the sample undergoes various thermal events such as decomposition, phase transitions, or chemical reactions. These events can lead to changes in the sample's weight due to loss of volatile components, decomposition, oxidation, or other processes. The TGA instrument continuously records the sample weight as a function of temperature or time. This data is then used to generate a thermogravimetric curve, which plots the weight

loss or gain of the sample versus temperature (or time). By analyzing the thermogravimetric curve, various parameters can be determined, including: onset temperature (the temperature at which the weight loss or gain begins); endset temperature (the temperature at which the weight loss or gain ends); peak temperature (the temperature at which the maximum rate of weight change occurs); weight loss (the amount of material lost or gained as a function of temperature). TGA can be performed under various atmospheres such as air, nitrogen, helium, or inert gases to study different types of reactions or decomposition processes. This allows the investigation of the thermal stability and behavior of materials under specific environmental conditions.

4.12 Bibliography

1. Stetefeld, J., McKenna, S. A. & Patel, T. R. Dynamic light scattering: a practical guide and applications in biomedical sciences. *Biophysical Reviews* vol. 8 409–427 Preprint at <https://doi.org/10.1007/s12551-016-0218-6> (2016).
2. Clogston, J. D. & Patri, A. K. Zeta Potential Measurement. in *Methods in Molecular Biology* vol. 697 63–70 (Humana Press Inc., 2011).
3. Bunaciu, A. A., Udriștioiu, E. gabriela & Aboul-Enein, H. Y. X-Ray Diffraction: Instrumentation and Applications. *Critical Reviews in Analytical Chemistry* vol. 45 289–299 Preprint at <https://doi.org/10.1080/10408347.2014.949616> (2015).
4. Pauw, B. R. Everything SAXS: Small-angle scattering pattern collection and correction (Journal of Physics Condensed Matter (2013) 25 (383201)). *Journal of Physics Condensed Matter* **26**, (2013).
5. Graewert, M. A. & Svergun, D. I. Impact and progress in small and wide angle X-ray scattering (SAXS and WAXS). *Current Opinion in Structural Biology* vol. 23 748–754 Preprint at <https://doi.org/10.1016/j.sbi.2013.06.007> (2013).
6. Stevie, F. A. & Donley, C. L. Introduction to x-ray photoelectron spectroscopy. *Journal of Vacuum Science & Technology A: Vacuum, Surfaces, and Films* **38**, (2020).
7. O’Grady, K., Lewis, V. G. & Dickson, D. P. E. Alternating gradient force magnetometry: Applications and extension to low temperatures (invited). *J Appl Phys* **73**, 5608–5613 (1993).
8. Naderi, M. Surface Area: Brunauer-Emmett-Teller (BET). in *Progress in Filtration and Separation* 585–608 (Elsevier Ltd, 2015). doi:10.1016/B978-0-12-384746-1.00014-8.
9. Williams, D. B. & Carter, C. B. *The Transmission Electron Microscope*. (Springer-Verlag US , 2009).
10. Zhou, W., Apkarian, R. P., Lin Wang, Z. & Joy, D. *Fundamentals of Scanning Electron Microscopy*.
11. Gill, P., Moghadam, T. T. & Ranjbar, B. *Differential Scanning Calorimetry Techniques: Applications in Biology and Nanoscience*. (2010).

5. Aim of the Work

Lipid-based systems have emerged as versatile platforms with remarkable advantages for a broad spectrum of applications in both biomedical and environmental fields.

In biomedical applications, lipid-based systems, including liposomes and lipid mesophases, offer exceptional biocompatibility and biodegradability, making them ideal candidates for drug delivery systems.

Lipid-based materials exhibit a low environmental impact, aligning with sustainable practices in the environmental field. They are used for efficiently removing pollutants from soil and water systems, delivering remediation agents to contaminated sites, and enhancing the wool and cotton dyeing process.

Inspired and motivated by these potential benefits, the investigations reported in this PhD thesis explored liposomes and lipid mesophases as drug delivery systems, magnetoliposomes as tools for wastewater remediation, and liposomes as additives in the wool dyeing process. The primary objective was to assess the correlation of lipid aggregate molecular structure with their physicochemical properties and, consequently, their efficacy in specific applications. This systematic approach aimed to identify crucial parameters influencing the success of formulations across diverse purposes.

Chapter 6: Liposomes as DDSs for Levodopa

6. Levodopa-loaded Liposomes for the Treatment of Parkinson's Disease

Parkinson's disease (PD) is a progressive neurological disorder that affects movement control. Named after the British physician James Parkinson who first described it in 1817,¹ Parkinson's is characterized by the gradual degeneration of specific nerve cells in the brain, particularly those responsible for producing dopamine. Dopamine plays a crucial role in transmitting signals within the brain that regulate and coordinate movement.² The hallmark symptoms of Parkinson's disease include tremors, bradykinesia (slowness of movement), rigidity, and postural instability. These motor symptoms often manifest subtly and progress gradually, impacting various aspects of daily life as the disease advances. Beyond motor symptoms, individuals with Parkinson's may experience non-motor symptoms such as cognitive impairment, sleep disturbances, and mood changes, contributing to the complexity of the disease.³ The exact cause of Parkinson's remains elusive, and while both genetic and environmental factors are believed to play a role, the precise interplay is not fully understood.⁴ The majority of cases are idiopathic, meaning the cause is unknown. Age is a significant risk factor, with the prevalence of Parkinson's increasing with advancing age. Oxidative stress (that occurs when there is an imbalance between the production of reactive oxygen species and the ability of the body to neutralize or repair the resulting damage) contributes to neurodegeneration and plays a significant role in the pathophysiology of PD.⁵

Despite extensive research, there is currently no cure for Parkinson's disease, but various treatment options aim to manage symptoms and improve the quality of life for individuals affected.⁶ Dopamine itself cannot be administered directly as a drug

because it does not cross the blood-brain barrier (BBB) effectively. The BBB is a selective membrane that restricts the passage of many substances, including dopamine, from the bloodstream into the brain. Introduced in the late 1960s, levodopa (LD) revolutionized the treatment landscape by alleviating the motor symptoms associated with this progressive neurological disorder. As a prodrug, LD crosses the BBB and is converted into dopamine, compensating for the diminished dopamine levels in the brains of individuals with Parkinson's. LD, orally administered, is absorbed from the intestine but only an amount less than 3% enters the brain unaffected so, as a consequence, it must be given in large quantities to reach the minimum therapeutic concentration, leading to significant side effects.⁷ The most notable issue is the development of motor fluctuations and dyskinesias over time, referred to as the "wearing-off" phenomenon. Patients may experience a diminishing response to each dose, leading to unpredictable fluctuations between mobility and immobility, impacting their daily activities. LD effectiveness diminishes with the progression of Parkinson's disease, and its long-term usage is associated with the risk of motor complications. Moreover, LD is light sensitive and easily oxidized to melanins in aqueous medium becoming inactive.⁸

Despite these limitations, LD remains the gold standard in the treatment of PD.

The intranasal route of drug administration is gaining attention as a promising and non-invasive method for delivering therapeutic agents. It provides a direct pathway to the central nervous system through the olfactory and trigeminal nerve pathways, avoiding the need to cross the BBB.⁹ This is particularly relevant for drugs targeting neurological conditions, as it allows for efficient delivery to the brain.

The effectiveness of intranasal therapy depends on the ability of the drug to penetrate the nasal mucosa and to its physical and chemical properties: the molecular weight, the charge, the polarity and, of course, the resistance to hydrolytic and redox enzyme that are present on the mucosa.¹⁰ A limiting factor is the mucociliary clearance, which is a defense mechanism of the respiratory system:

when xenobiotics interact with the nasal mucosa, they are rapidly eliminated through the digestive system. In the past few years, liposomes have gained a lot of attention as drug carriers because of their biocompatibility and their ability to entrap both polar and non-polar molecules, protecting them from the surrounding environment. Besides, it was demonstrated by several researches that they show mucoadhesive properties, making them good candidates for intranasal delivery. Zheng and colleagues showcased the superior efficacy of intranasal delivery for a hydrophilic β -amyloid protein breaker peptide encapsulated in liposomes compared to intravenous administration of the free drug. This was evident in terms of prolonged residence time and enhanced brain uptake.¹¹ In a separate study, Guo *et al.* demonstrated that liposomal intranasal delivery of ferric ammonium citrate for treating iron deficiency anemia led to elevated drug levels across all brain sections one day post-treatment, particularly in the olfactory bulb, a crucial entry point for the drug into the brain.¹² Furthermore, liposomal formulations extend their applicability to lipophilic drugs, showcasing their potential for efficient brain delivery after intranasal administration. The use of liposomes addresses challenges associated with low solubility, resulting in prolonged therapeutic effects, heightened drug concentration, and sustained distribution within the brain.¹³ Donepezil, when included in liposomes and administered intranasally, exhibited increased brain and systemic bioavailability. Additionally, research by Al Asmari *et al.* highlighted that the transport of the drug to the brain occurs through both direct and indirect pathways.¹⁴

The physicochemical characteristics of liposomes are strictly linked to the chemical composition of the monomers involved in their formation. Factors such as the length of alkyl chains, the presence or absence of unsaturations, and the adjustment of the hydrophilic/hydrophobic balance within the molecules exert considerable influence on the fluidity of the bilayer and the interaction with solutes encapsulated within the vesicles.^{15,16} The effectiveness of the aggregates in

interacting with target cells, membrane permeability, and the entrapment efficiency of loaded active principles is influenced by factors such as the charge of the polar headgroup^{15,17-21} and/or the nature of counterions.²²⁻²⁴

The incorporation of surfactants can induce destabilization of vesicle bilayers, facilitating changes in shape and volume at minimal energetic cost, thereby enhancing the elasticity of liposomes.^{25,26} Additionally, the introduction of surfactants into the liposomal bilayer has the potential to alter the physical and chemical properties of the vesicles.^{27,28} Within the diverse classes of amphiphilic molecules, our attention was drawn particularly to *N*-oxide (*N*-ox) and quaternary ammonium surfactants. *N*-ox surfactants, recognized for their biodegradability and non-toxic nature,²⁹ exhibit a charge dependent on the medium's pH, remaining non-ionic under physiological conditions. They have been previously employed in the preparation of pH-sensitive liposomes and possess noteworthy antioxidant,³⁰ antiperoxidative,³¹ and antiradical properties.²⁹ Similarly, quaternary ammonium surfactants have demonstrated antioxidant capabilities, effectively reducing the oxidation of membrane lipids in pig erythrocytes.²⁰

Based on these premises, we designed mixed liposomes for the delivery of LD composed of a saturated natural phospholipid (1,2-dimyristoyl-sn-glycero-3-phosphocholine, DMPC) and one of the micelle-forming surfactants outlined in Chart 1A. Two different molar ratios, 9:1 and 7:3, were used in the preparation. Despite having the same chain length, the surfactants differ in their polar headgroup: two bear the *N*-oxide moiety, while the other two possess the quaternary ammonium group. The *L*-prolinol derivatives, owing to the presence of the pyrrolidinium ring, exhibit a lower degree of freedom compared to their acyclic analogues.³² This characteristic significantly influences the volume and hydration of the headgroup. They demonstrated the ability to enhance the antiradical activity of substrates within the micelles they form and improve the efficacy of liposomes as delivery systems when included in the aggregates.

Two potent natural antioxidants (Chart 1B), the hydrophilic ascorbic acid (AA) and the hydrophobic quercetin (Qu), were incorporated into the formulations to prevent prodrug oxidation and limit the progression of PD.³³ Notably, AA can safeguard neuronal cells from damages induced by reactive oxygen species and reduce the consumption of endogenous scavenging antioxidants.³⁴ Due to its polar nature, AA was loaded into the aqueous core of liposomes alongside LD through passive loading, effectively inhibiting LD oxidation to melanins. Conversely, Qu was situated in the lipid bilayer, reacting with oxygen that might traverse the membrane, thereby hindering it from reaching the prodrug.

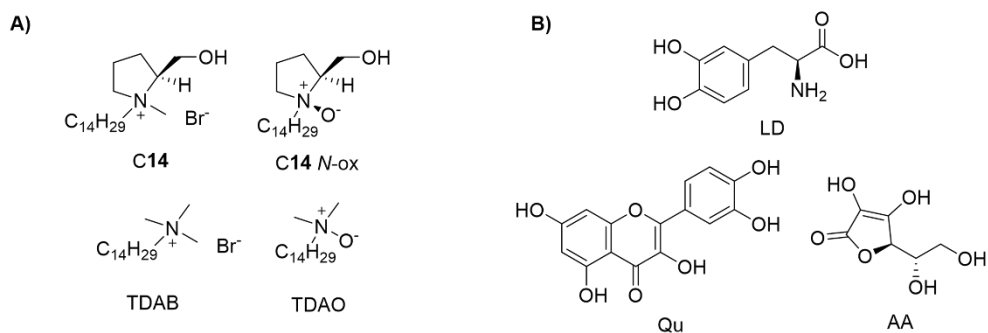


Chart 1. Structures of A) the surfactants used in liposomal formulations, and B) the molecules vehiculated.

Our investigation aimed to comprehend how the composition of mixed liposomes influences vesicular properties, including entrapment efficiency, transition temperature, antiradical activity of liposomal Qu, and *ex-vivo* permeability through porcine nasal mucosa. We delved into the subtle differences in the molecular structure of lipids, examining their impact on surface properties, bilayer organization, and consequently, the physicochemical and biological behavior of the formulation. The primary goal was to highlight the critical characteristics of liposomal components essential for efficiently delivering LD across the BBB.

Diverging from existing literature, our formulations simultaneously incorporated both a hydrophilic and a hydrophobic natural antioxidant. This approach aimed to

exploit their potential synergistic effects, a novel aspect not commonly reported in prior studies.

6.1 Liposome preparation and characterization

Liposome formulations were prepared according to the Bangham methodology. Briefly, lipids, surfactants, and Qu at the appropriate molar ratio were dissolved in a mixture of chloroform and methanol. Subsequently, the organic solvent was evaporated under reduced pressure to obtain a lipid film, that was hydrated with a PBS solution containing LD and AA. The mixture was then heated and vortex-mixed to obtain MLVs, and then sonicated to obtain SUVs. Untrapped drugs were removed via dialysis protocols.

The size and ζ -potential of the investigated formulations (assessed through dynamic light scattering and electrophoretic mobility, respectively) are presented in Table 1.

Table 1. Size (expressed in nm, and obtained from intensity weighted distributions) and ζ -potential (expressed in mV) of the investigated formulations in the presence or in the absence of LD, AA and Qu. Reported values correspond to the average values over 3 measurements. Error in ζ -potential values is within 3 mV. Pdl is lower than 0.2 in all cases. * These samples show a statistically significant difference from their loaded counterparts.

	empty formulations		loaded formulation	
	size	ζ -potential	size	ζ -potential
DMPC	107 ± 7	-2	117 ± 7	-2
DMPC/TDAB 9:1	105 ± 9	12	92 ± 6	10
*DMPC/TDAO 9:1	157 ± 14	8	92 ± 9	2
*DMPC/C14 9:1	149 ± 12	12	118 ± 13	11
DMPC/C14 <i>N</i> -ox 9:1	160 ± 13	9	140 ± 15	7
DMPC/TDAB 7:3	117 ± 9	11	121 ± 13	21
DMPC/TDAO 7:3	104 ± 7	17	90 ± 7	20
*DMPC/C14 7:3	154 ± 8	15	105 ± 11	26
DMPC/C14 <i>N</i> -ox 7:3	114 ± 11	18	112 ± 12	22

As expected, formulations containing a cationic surfactant exhibited positive ζ -potential values, even if relatively low, due to the cautious application of low voltage to avoid potential Joule heating effects. Notably, using a higher voltage led to the blackening of the electrode surface, resulting in the degradation of data quality. Positive ζ -potentials were also expected for aggregates containing zwitterionic surfactants, based on our earlier observations of relatively high ζ -potentials in aggregates containing C14 *N*-ox or its analogues.^{35–38}

Liposomes formulated with 10 mol% of surfactant, whether loaded or not, displayed the lowest ζ -potential values. An overall increase in ζ -potential was observed with an increased amount of the cationic component (30 mol%). This increase was particularly notable in the loaded formulations, suggesting electrostatic interactions between the loaded molecules and liposomal components and/or different counterion binding. However, in the case of empty DMPC/TDAB liposomes, ζ -potential remained unchanged with 10 or 30 mol% of the cationic component. This anomalous behavior may be attributed to domain formation, as reported in the literature for mixed empty liposomes containing quaternary ammonium surfactants:^{39,40} phase segregation could result in a unique lipid organization influencing the exposure of polar headgroups to the bulk.

In general, empty liposomes exhibited diameters ranging from 100 nm to 160 nm. In certain instances, the diameter of loaded liposomes showed a slight decrease. The results of the one-way ANOVA test revealed that the observed differences in diameter between loaded and empty liposomes are statistically significant ($p < 0.05$) for three formulations (DMPC/TDAO 9:1, DMPC/C14 9:1, DMPC/C14 7:3). This finding supports the hypothesis of specific electrostatic interactions occurring between liposomes and their cargo.

It is well-established that the incorporation of a cationic component in the bilayer can influence specific characteristics, such as electric charge density, lipid packing, or membrane permeability, in a concentration-dependent manner. In the

investigated formulations, the occurrence of electrostatic interactions between the positively charged liposome surface and LD and AA, both ionized at the working pH, is not surprising. Similar considerations are reported in the literature for cationic liposomes loaded with LD and AA.⁴¹

The stability of liposomal dispersions is of paramount importance in pharmaceutical applications: they need to remain stable over time to ensure that the encapsulated drugs are preserved, maintaining their efficacy and preventing potential degradation or changes in pharmacological activity. Stability prevents the aggregation or fusion of liposomes, ensuring that they do not coalesce and lose their unique properties.

All formulations with a ratio of 7:3 remained stable for at least two weeks, whereas we observed an increase in the Pdl values (≈ 0.4) in 9:1 and pure DMPC formulations after 10 days. This occurrence is likely attributed to the higher ζ -potential values of the 7:3 formulations, which serve to prevent aggregation.

The morphology and dimensions of the liposomes were further examined through electron microscopy measurements, after the deposition of 10 μL of the liposome dispersion on a copper grid (200 mesh) with an amorphous carbon film. Samples were analyzed using a Zeiss GeminiSEM 500 microscope. Representative images of both empty and loaded liposomes are presented in Figure 1.

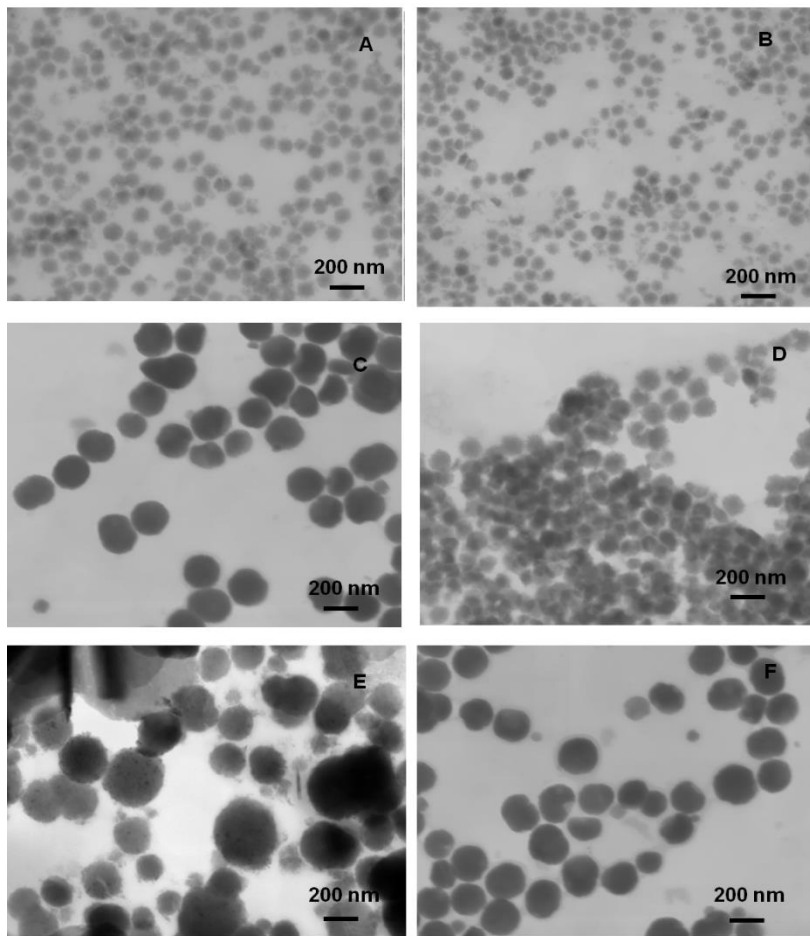


Figure 1. SEM images of (A) empty and (B) loaded DMPC liposomes, (C) empty and (D) loaded DMPC/TDAO 9:1 liposomes and (E) empty and (F) loaded DMPC/C14 *N*-ox 9:1 liposomes.

These images validate the spherical structure of vesicles and align well with the DLS results. In the case of the DMPC formulation, the diameter of both empty and loaded liposomes is approximately the same (≈ 100 nm, Figure 1A and 1B), similar to the situation with DMPC/C14 *N*-ox 9:1 (≈ 150 nm, Figure 1E and 1F). However, empty DMPC/TDAO 9:1 liposomes exhibit a larger diameter than the loaded ones (Figure 1C and 1D).

6.2 LD and Qu Entrapment

LD and the two antioxidants were incorporated during the formation of liposomes through passive loading. The encapsulation efficiency (EE) values for LD and Qu in DMPC alone and in mixed formulations are presented in Figure 2.

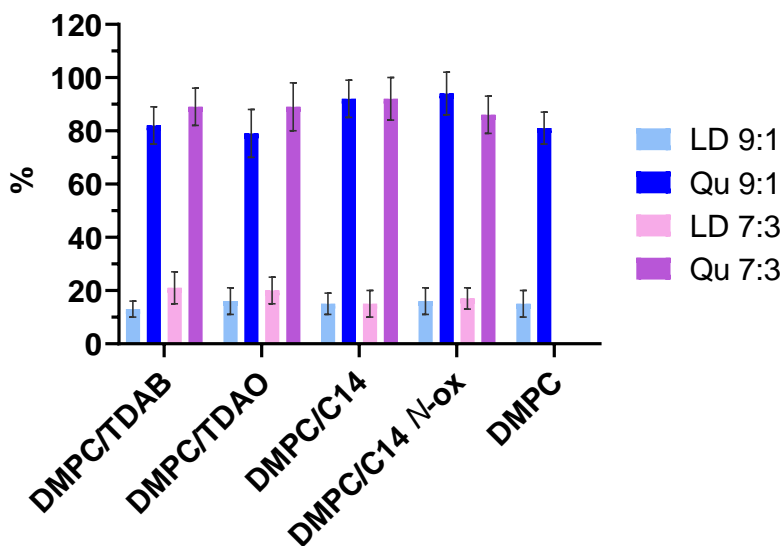


Figure 2. %EE of LD and Qu in the investigated formulations.

The EE of Qu was approximately 85%, whereas the EE of LD was around 15%. This disparity is unsurprising given the hydrophobic nature of Qu and the hydrophilic nature of LD. In general, hydrophobic drugs can readily incorporate into the lipid bilayer, leading to higher entrapment efficiency. In contrast, hydrophilic drugs face challenges in being encapsulated in the core of due to their affinity for water.

As anticipated, no notable differences were observed among the various formulations. The EE of AA was not assessed as it was only added to prevent the oxidation of LD.

6.3 Liposome Transition Temperature

The thermotropic parameter of liposome formulations were evaluated through DSC measurements. We analyzed MLVs to avoid complex thermograms resulting from fusion into larger aggregates during the scans, a phenomenon commonly observed in unilamellar vesicles.⁴²

The thermodynamic parameters for both loaded and unloaded MLVs are presented in Table 2-3, respectively.

Table 2. Thermodynamic parameters obtained by DSC measurements on empty and loaded 9:1 liposome formulations. Empty and loaded DMPC liposomes are also reported for comparison. Uncertainties are ± 0.1 °C for the temperature values and ± 0.5 J/g for the ΔH_m values.

Tp is related to the rotation of the polar headgroup of phospholipids, while Tm corresponds to the transition between the gel phase and the liquid crystalline phase of the lipid bilayer.

Formulation (9:1)	Tp (°C)	Tm (°C)	ΔH (J/g)
DMPC	14.0	24.1	27.9
DMPC + Qu, LD, AA	/	23.8	27.5
DMPC/TDAB	16.3	25.3	27.6
DMPC/TDAB + Qu, LD, AA	/	25.1	28.4
DMPC/TDAO	12.8	24.0	30.8
DMPC/TDAO + Qu, LD, AA	/	24.5	29.2
DMPC/C14	11.7	24.8	33.2
DMPC/C14 + Qu, LD, AA	/	24.0	24.2
DMPC/C14 N-ox	13.4	25.1	39.7
DMPC/C14 N-ox + Qu, LD, AA	/	24.7	27.8

Table 3. Thermodynamic parameters obtained by DSC measurements on empty and loaded 7:3 liposome formulations. Empty and loaded DMPC liposomes are also reported for comparison. Uncertainties are ± 0.1 °C for the temperature values and ± 0.5 J/g for the ΔH_m values.

Formulation (7:3)	T _p (°C)	T _m (°C)	ΔH (J/g)
DMPC	14.0	24.1	27.9
DMPC + Qu, LD, AA	/	23.8	27.5
DMPC/TDAB	17.2	24.0, 25.5	31.0
DMPC/TDAB + Qu, LD, AA	/	20.6, 25.5	33.4
DMPC/TDAO	/	22.0, 24.4	30.0
DMPC/TDAO + Qu, LD, AA	/	22.9, 25.0	29.3
DMPC/C14	/	22.7, 25.5	29.7
DMPC/C14 + Qu, LD, AA	/	21.8, 24.8	27.3
DMPC/C14 <i>N</i> -ox	/	23.6, 25.2	31.8
DMPC/C14 <i>N</i> -ox + Qu, LD, AA	/	22.3, 24.8	23.2

The thermograms for both loaded and empty DMPC/surfactant 9:1 liposomes generally exhibited an increase in T_m values, indicating a higher compactness of the bilayer compared to pure DMPC. As mentioned earlier, the interaction among the alkyl chains contributes more significantly to the main transition than the nature of the polar headgroup. Despite structural differences between DMPC and the minor component, their equal chain length minimizes any potential disturbing effects from the micelle-forming surfactant. In line with this, ΔH values remain nearly unchanged in mixed bilayers compared to DMPC alone, with the exception of DMPC/C14 and DMPC/C14 *N*-ox not loaded liposomes.

In the presence of solutes, the pretransition vanishes in all 9:1 formulations, indicating their proximity or localization in a region of the bilayer close to the

headgroups. This observation aligns with findings in the literature regarding Qu.^{43,44} Despite Qu being a highly hydrophobic molecule with limited solubility in water⁴⁵ and it would be expected to find it deeply in the bilayer, it appears that its hydroxyl groups may interact with the polar headgroups of lipids. Qu has five exchangeable protons with pKa values ranging from 6 to 13 units, and it exists in three different anionic forms at physiological pH.⁴⁶ Likely, the microenvironment surrounding the liposome headgroup promotes the partial deprotonation of Qu hydroxyl groups, leading to electrostatic attraction between the negatively charged antioxidant and the polar groups of lipids.

As the percentage of synthetic surfactant increases from 10% to 30%, the thermograms exhibit the disappearance of T_p, with the exception of TDAB-containing liposomes. This observation, coupled with the fact that DMPC/TDAB liposomes 9:1 feature the highest T_p (at least 3 °C difference from other formulations), suggests particularly strong interactions in the headgroup region that remain unaltered even with an increased amount of the cationic component. Broadening and splitting of the main peak appear in the thermograms, both in the presence and absence of Qu. This indicates phase separation in the liposome bilayer, likely due to poor miscibility of the components at this molar percentage. Literature reports confirm that phase separation occurs in empty mixed liposomes containing quaternary ammonium surfactants, with or without the *L*-prolinol moiety.^{39,40} In particular, in the case of empty DMPC/TDAB 7:3 liposomes, the predominant peak appears at 25.5°C, the same temperature as the peak relative to the main transition in the thermogram of 9:1 liposomes. This, along with the presence of T_p, suggests that lipid organization in most parts of the bilayer is very similar in liposomes containing 10 or 30 molar percentage of TDAB. The broadening of the peak at a lower temperature is more evident in Qu-loaded liposomes compared to not loaded ones (except for DMPC/TDAO), indicating that the antioxidant preferentially accumulates in the corresponding domain. The ΔH values

are quite similar and decrease only when Qu is included in DMPC/C14 and DMPC/C14 N-ox liposomes, as observed in 9:1 formulations.

Overall, liposomes containing synthetic surfactants with the pyrrolidinium ring exhibit similar thermotropic behavior, whereas liposomes containing acyclic analogues show peculiar thermotropic properties, likely due to different organization in the headgroup region, as confirmed by the trend in ζ -potential values.

6.4 Qu and Liposomal-Qu Antiradical Activity

The antiradical activity of both free and loaded Qu was assessed using the ABTS^{•+} methodology. In its oxidized state, ABTS^{•+} exhibits a green color, which disappears upon reduction, resulting in a colorless solution. The rate of this process is indicative of the concentration and antiradical capacity of the system. Spectrophotometric monitoring of the degradation of ABTS^{•+} over time was conducted in the absence and presence of free and liposomal Qu (Figure 3).

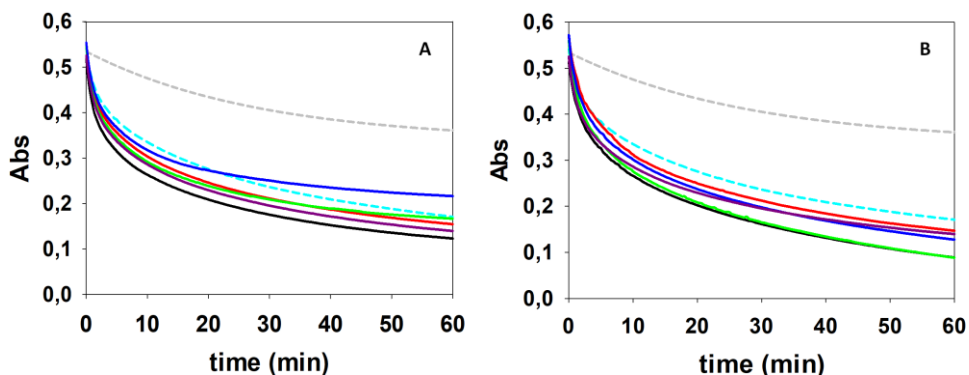


Figure 3. Kinetic measurements of ABTS^{•+} degradation in the absence or in the presence of free and loaded Qu for 9:1 formulations (A) and 7:3 formulations (B): free ABTS^{•+} (grey dashed line), free Qu (cyano dashed line), DMPC/TDAB (dark line), DMPC/TDAO (red line), DMPC/C14 (green line), DMPC/C14 N-ox (blue line), DMPC (purple line).

As expected, the degradation of ABTS^{•+} in the presence of free Qu (cyano dashed line) occurred much more rapidly compared to its degradation in the absence of Qu

(grey dashed line). Qu is known to be one of the most efficient antioxidants among flavonoids due to its two antioxidant pharmacophores and its capability to scavenge free radicals and bind transition metal ions.⁴⁷ When Qu is incorporated into liposomal formulations of DMPC or those containing 10% of acyclic surfactants, its antiradical activity increases, especially with TDAB. This outcome can be explained by considering that in the latter formulation, Qu engages in specific interactions with the polar headgroups region (as indicated by T_p values), affecting its ability to scavenge $ABTS^+$. Generally, the antioxidant activity of a molecule is significantly influenced by the polarity of its microenvironment^{48,49} and, for aqueous solutions, by the pH of the medium.^{50,51} Based on the ζ -potential values, Qu in DMPC/TDAB liposomes experiences a more polar environment compared to the almost neutral DMPC and DMPC/TDAO liposomes.

On the other hand, after an initial burst, the formulation containing C14 N-ox surfactant exhibited a slowdown of the antiradical activity of Qu after twenty minutes (blue line in Figure 3A), while the formulation containing the C14 surfactant (green line in Figure 3A) showed behavior comparable to free Qu. Despite the similar ζ -potential values of these formulations to the TDAB one, lipid organization differs, as suggested by DSC results. This may imply a different hydration of the polar headgroups and/or different water penetration near them, with a consequent effect on the antiradical activity of Qu due to its different accessibility and microenvironment polarity. The folding of the pyrrolidinium ring of N-ox could explain why this formulation behaves differently from the others.³⁵ This evidence confirms that the antiradical activity of a molecule embedded in the bilayer does not depend only on its intrinsic properties but is primarily affected by its interaction with lipids, and even subtle modifications of their molecular structure can be relevant.

With an increase in the molar fraction of surfactant up to 30%, the antiradical activity of Qu exhibits an overall enhancement in all the investigated mixed

formulations compared to their corresponding 9:1 counterparts, especially in the case of cationic ones. The presence of a Qu-rich domain, as indicated by DSC results, likely leads to an elevated local concentration of Qu, influencing its interaction with the radical cation in a manner contingent upon the properties of the domain. The only exception was observed in TDAO-containing liposomes, possibly because Qu does not appear to segregate into a preferential domain in these aggregates.

Each curve was fitted with an exponential decay by two processes with the exception of the curve related to the spontaneous degradation of free ABTS^{•+} that was fitted with a simple exponential decay. The resulting time constant (τ) indicates the time required for half of the ABTS^{•+} in solution to be reduced through interaction with Qu, thereby providing information about the speed of the reaction between ABTS^{•+} and free or loaded Qu in the studied systems. The τ values derived from the data analysis are presented in Figure 4.

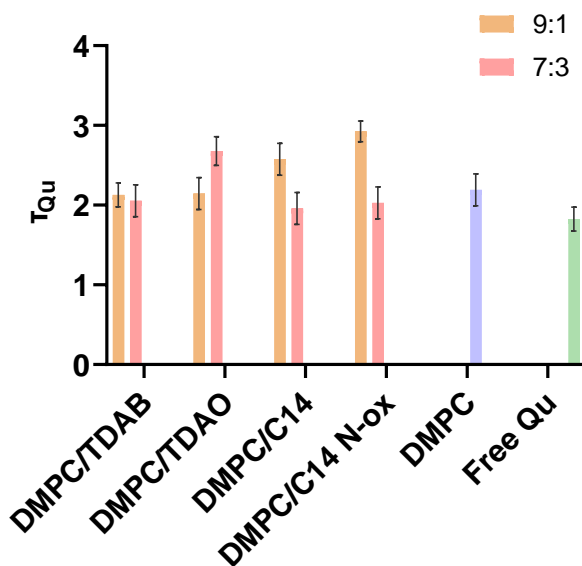


Figure 4. Comparison of τ_{Qu} relative to of ABTS^{•+} degradation curve in the presence of free or liposomal Qu for 9:1 and 7:3 formulations. The reported errors correspond to the standard error obtained from the fit.

In the majority of instances, comparable outcomes were achieved with both free and liposomal Qu. This suggests that the antioxidant activity of liposomal Qu remains intact. This is a positive outcome, considering that a portion of liposomal Qu is not exposed to $\text{ABTS}^{\cdot+}$ as it is situated in a deeper layer of the bilayer (inaccessible to a radical cation). Variations in the bilayer's compactness can also impact the ability of $\text{ABTS}^{\cdot+}$ to reach Qu within the bilayer.

6.5 *Ex-vivo* Permeability to Porcine Nasal Mucosa

The ability of both free and liposomal LD to cross the nasal mucosa was assessed through *ex-vivo* permeability studies utilizing vertical Franz diffusion cells. Initially, we confirmed the absence of lipid interaction with our 3D printed cells by conducting the Stewart assay on the liposomal solution that had been in contact with them for 24 hours. For the permeability tests, we opted not to separate unloaded LD from liposomes due to the high free LD concentration in the solution, making the removal process through dialysis excessively prolonged and prone to LD degradation. Porcine nasal mucosa was selected for its similarity to the human counterpart,⁵² and the experiments were conducted at 37 °C to replicate the temperature of the human nose. A PBS buffer (150 mM, pH 7.4) served as the receptor medium to mimic physiological conditions.⁵³

HPLC analyses were employed for this assessment due to the release of substances by porcine mucosa into the acceptor compartment of the Franz cells, causing interference with the fluorescence of LD. The percentage of LD that crossed the mucosa in the presence of loaded liposomes after 3 and 6 hours was less than 1%, hence Figure 5 presents only the percentage after 24 hours. Interestingly, the quantity of free LD traversing the nasal mucosa was remarkably high (exceeding 90%), likely attributed to its small dimensions and comparatively low water solubility compared to the aggregates.

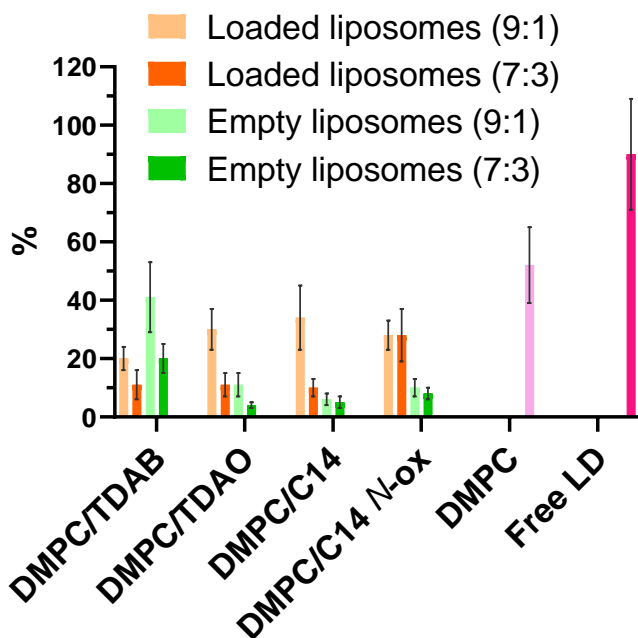


Figure 5. Comparison of the % of LD that crosses the porcine nasal mucosa after 24 h, either free, vehiculated in liposomes, or free in the presence of empty liposomes.

The observation that a reduced quantity of LD, in comparison to free LD, reaches the acceptor compartment in the presence of loaded liposomes suggests that the aggregates tend to remain within the membrane, obstructing it to varying degrees depending on the formulation. Notably, neutral DMPC liposomes exhibited the highest percentage of LD in the acceptor compartment, while formulations containing 30% of TDAO, C14, and C14 *N*-ox allowed no more than 10% of LD to reach it. This outcome implies that the strength of the interaction between aggregates and negatively charged nasal mucosa is proportional to their ζ -potential values (refer to Table 1). Specifically, mixed formulations with 10% of surfactant exhibited lower ζ -potential values and higher LD permeability compared to their counterparts with 30% of surfactant, except for the formulation containing 30% of TDAB, which featured a potential similar to other 7:3 formulations. This suggests that liposomes ζ -potential is not the only parameter governing their interaction

with biological membranes; factors such as polar head group exposure, structure (cationic or *N*-ox), and counterion association also play crucial roles. To quantify the impact of liposomes on the reduction of LD nasal membrane permeability, we conducted similar experiments in which empty liposomes and free drug were combined in the donor compartment of Franz cells. In all cases, the presence of empty liposomes resulted in a lower amount of LD passing through the mucosa compared to when loaded liposomes were present (see Figure 5). This implies that even if some liposomes are retained in the membrane, the amount that successfully passes facilitates drug transport.

6.6 Conclusion

This study conducted preliminary investigations into the potential application of liposomes as an intranasal DDS.

DLS, TEM, and DSC analysis confirmed the formation of mixed liposomes and the successful incorporation of the four synthetic surfactants into the lipid bilayer. It was observed that ζ -potential alone does not exclusively influence the interaction with negatively charged biological membranes; the lipid organization and bilayer compactness also play crucial roles, as evidenced by Qu antiradical activity. Among the mixed formulations, the cationic formulation DMPC/TDAB 7:3 emerged as the most promising for intranasal LD delivery. It exhibited the highest LD entrapment efficiency, Qu antiradical activity, and ex-vivo permeability through nasal mucosa. Despite the lower percentage of LD reaching the acceptor compartment for liposome-loaded LD compared to the free form, the results are still considered promising for several reasons: i) the presence of a DDS protects LD from oxidation; ii) free LD is known to exhibit side effects;⁵⁴ iii) only a small amount of the free drug can reach the brain when administered intravenously.

6.7 Bibliography

1. Fahn, S. The medical treatment of Parkinson disease from James Parkinson to George Cotzias. *Movement Disorders* vol. 30 4–18 Preprint at <https://doi.org/10.1002/mds.26102> (2015).
2. Segura-Aguilar, J. *et al.* Protective and toxic roles of dopamine in Parkinson's disease. *Journal of Neurochemistry* vol. 129 898–915 Preprint at <https://doi.org/10.1111/jnc.12686> (2014).
3. Pfeiffer, R. F. Non-motor symptoms in Parkinson's disease. *Parkinsonism Relat Disord* **22**, S119–S122 (2016).
4. Wood-Kaczmar, A., Gandhi, S. & Wood, N. W. Understanding the molecular causes of Parkinson's disease. *Trends in Molecular Medicine* vol. 12 521–528 Preprint at <https://doi.org/10.1016/j.molmed.2006.09.007> (2006).
5. Jenner, P. *et al.* Oxidative stress in Parkinson's disease. *Annals of Neurology* vol. 53 Preprint at <https://doi.org/10.1002/ana.10483> (2003).
6. Lew, M. Overview of Parkinson's disease. *Pharmacotherapy* vol. 27 Preprint at <https://doi.org/10.1592/phco.27.12part2.155s> (2007).
7. Ferreira, J. J. *et al.* Effect of opicapone on levodopa pharmacokinetics, catechol-O-methyltransferase activity and motor fluctuations in patients with Parkinson's disease. *Eur J Neurol* **22**, 815–e56 (2015).
8. Bunsen, A. & Fitzpatrick', T. B. *BIOCHEMISTRY OF MELANIN FORMATION*.
9. Emad, N. A., Ahmed, B., Alhalmi, A., Alzobaidi, N. & Al-Kubati, S. S. Recent progress in nanocarriers for direct nose to brain drug delivery. *Journal of Drug Delivery Science and Technology* vol. 64 Preprint at <https://doi.org/10.1016/j.jddst.2021.102642> (2021).
10. Costantino, H. R., Illum, L., Brandt, G., Johnson, P. H. & Quay, S. C. Intranasal delivery: Physicochemical and therapeutic aspects. *International Journal of Pharmaceutics* vol. 337 1–24 Preprint at <https://doi.org/10.1016/j.ijpharm.2007.03.025> (2007).
11. Zheng, X. *et al.* Intranasal H102 Peptide-Loaded Liposomes for Brain Delivery to Treat Alzheimer's Disease. *Pharm Res* **32**, 3837–3849 (2015).
12. Guo, X. *et al.* Nasal delivery of nanoliposome-encapsulated ferric ammonium citrate can increase the iron content of rat brain. *J Nanobiotechnology* **15**, (2017).

13. Hong, S. S., Oh, K. T., Choi, H. G. & Lim, S. J. Liposomal formulations for nose-to-brain delivery: Recent advances and future perspectives. *Pharmaceutics* vol. 11 Preprint at <https://doi.org/10.3390/pharmaceutics11100540> (2019).
14. Al Asmari, A. K., Ullah, Z., Tariq, M. & Fatani, A. Preparation, characterization, and in vivo evaluation of intranasally administered liposomal formulation of donepezil. *Drug Des Devel Ther* **10**, 205–215 (2016).
15. Bordi, F. *et al.* Synthesis and physicochemical characterization of new twin-tailed N-oxide based gemini surfactants. *Langmuir* **26**, 6177–6183 (2010).
16. Battista, S. *et al.* Curcuminoids-loaded liposomes: influence of lipid composition on their physicochemical properties and efficacy as delivery systems. *Colloids Surf A Physicochem Eng Asp* **597**, (2020).
17. Bombelli, C. *et al.* Efficiency of liposomes in the delivery of a photosensitizer controlled by the stereochemistry of a gemini surfactant component. *Mol Pharm* **7**, 130–137 (2010).
18. Bombelli, C. *et al.* New cationic liposomes as vehicles of m-tetrahydroxyphenylchlorin in photodynamic therapy of infectious diseases. in *Molecular Pharmaceutics* vol. 5 672–679 (2008).
19. Giansanti, L. *et al.* Glucosylated pH-sensitive liposomes as potential drug delivery systems. *Chem Phys Lipids* **200**, 113–119 (2016).
20. Kleszczyńska³, H., Sarapuk³, J., Święcimskab, M. O. & Itekb, S. W. *Antioxidative Activity of Some Quaternary Ammonium Salts Incorporated into Erythrocyte Membranes*. *Z. Naturforsch* vol. 55 www.znaturforsch.com (2000).
21. Gabizon, A. & Papahadjopoulos, D. The role of surface charge and hydrophilic groups on liposome clearance in vivo. *Biochim Biophys Acta* **1103**, 94–100 (1992).
22. Feitosa, E., Adati, R. D. & Karlsson, G. The role of counterion and concentration on the thermal behavior and structure of dioctadecyldimethylammonium bromide and chloride in water. *Thermochim Acta* **724**, (2023).
23. Oliveira, A. C. N. *et al.* Counter ions and constituents combination affect DODAX:MO nanocarriers toxicity: In vitro and in vivo. *Toxicol Res (Camb)* **5**, 1244–1255 (2016).

24. Shang, X., Liu, Y., Yan, E. & Eisenthal, K. B. Effects of counterions on molecular transport across liposome bilayer: Probed by second harmonic generation. *Journal of Physical Chemistry B* **105**, 12816–12822 (2001).
25. Bnyan, R. *et al.* Surfactant Effects on Lipid-Based Vesicles Properties. *Journal of Pharmaceutical Sciences* vol. 107 1237–1246 Preprint at <https://doi.org/10.1016/j.xphs.2018.01.005> (2018).
26. Marwah, M., Perrie, Y., Badhan, R. K. S. & Lowry, D. Intracellular uptake of EGCG-loaded deformable controlled release liposomes for skin cancer. *J Liposome Res* **30**, 136–149 (2020).
27. Tai, K. *et al.* A comparison of physicochemical and functional properties of icaritin-loaded liposomes based on different surfactants. *Colloids Surf A Physicochem Eng Asp* **518**, 218–231 (2017).
28. Caritá, A. C. *et al.* Elastic cationic liposomes for vitamin C delivery: Development, characterization and skin absorption study. *Int J Pharm* **638**, (2023).
29. Lewińska, A., Kulbacka, J., Domżał-Kędzia, M. & Witwicki, M. Antiradical properties of n-oxide surfactants—two in one. *Int J Mol Sci* **22**, (2021).
30. Piasecki, A., Piłakowska-Pietras, D., Baran, A. & Krasowska, A. Synthesis and properties of surface chemically pure alkylamidoamine-N- oxides at the air/water interface. *J Surfactants Deterg* **11**, 187–194 (2008).
31. Krasowska, A., Piasecki, A., Murzyn, A. & Sigler, K. *Assaying the Antioxidant and Radical Scavenging Properties of Aliphatic Mono- and Di-N-Oxides in Superoxide Dismutase-Deficient Yeast and in a Chemiluminescence Test.* *Folia Microbiol* vol. 52 <http://www.biomed.cas.cz/mbu/fovia/> (2007).
32. Karukstis, K. K. & McDonough, J. R. Characterization of the aggregates of N-Alkyl-N-methylpyrrolidinium bromide surfactants in aqueous solution. *Langmuir* **21**, 5716–5721 (2005).
33. Jin, H. *et al.* Mitochondria-targeted antioxidants for treatment of Parkinson's disease: Preclinical and clinical outcomes. *Biochimica et Biophysica Acta - Molecular Basis of Disease* vol. 1842 1282–1294 Preprint at <https://doi.org/10.1016/j.bbadis.2013.09.007> (2014).
34. Covarrubias-Pinto, A., Acuña, A. I., Beltrán, F. A., Torres-Díaz, L. & Castro, M. A. Old things new view: Ascorbic acid protects the brain in neurodegenerative disorders. *International Journal of Molecular Sciences* vol. 16 28194–28217 Preprint at <https://doi.org/10.3390/ijms161226095> (2015).

35. Battista, S. *et al.* Use of N-oxide and cationic surfactants to enhance antioxidant properties of (+)-usnic acid loaded liposomes. *Colloids Surf A Physicochem Eng Asp* **585**, (2020).
36. Battista, S. *et al.* Homogeneous and stable (+)-usnic acid loaded liposomes prepared by compressed CO₂. *Colloids Surf A Physicochem Eng Asp* **624**, (2021).
37. Battista, S. *et al.* Quatsomes Formulated with I -Prolinol-Derived Surfactants as Antibacterial Nanocarriers of (+)-Usnic Acid with Antioxidant Activity. *ACS Appl Nano Mater* **5**, 6140–6148 (2022).
38. Battista, S. *et al.* Structurally Related Liposomes Containing N-Oxide Surfactants: Physicochemical Properties and Evaluation of Antimicrobial Activity in Combination with Therapeutically Available Antibiotics. *Mol Pharm* **19**, 788–797 (2022).
39. Barenholz, Y. *et al.* Influence of lipid composition on the thermotropic behavior and size distribution of mixed cationic liposomes. *J Colloid Interface Sci* **356**, 46–53 (2011).
40. Lima, L. M. C. *et al.* Morphological and nanomechanical behavior of supported lipid bilayers on addition of cationic surfactants. *Langmuir* **29**, 9352–9361 (2013).
41. García Esteban, E., Cózar-Bernal, M. J., Rabasco Álvarez, A. M. & González-Rodríguez, M. L. A comparative study of stabilising effect and antioxidant activity of different antioxidants on levodopa-loaded liposomes. *J Microencapsul* **35**, 357–371 (2018).
42. Drazenovic, J. *et al.* Effect of lamellarity and size on calorimetric phase transitions in single component phosphatidylcholine vesicles. *Biochim Biophys Acta Biomembr* **1848**, 532–543 (2015).
43. Drăgușin, M., Țugulea, L. & Ganea, C. The effects of the natural antioxidant quercetin and anions of the Hofmeister series on liposomes marked with chlorophyll a. *Gen Physiol Biophys* **29**, 41–49 (2010).
44. Liu, W. & Guo, R. Interaction between flavonoid, quercetin and surfactant aggregates with different charges. *J Colloid Interface Sci* **302**, 625–632 (2006).
45. Abraham, M. H. & Acree, W. E. On the solubility of quercetin. *J Mol Liq* **197**, 157–159 (2014).

46. Álvarez-Diduk, R., Ramírez-Silva, M. T., Galano, A. & Merkoçi, A. Deprotonation mechanism and acidity constants in aqueous solution of flavonols: A combined experimental and theoretical study. *Journal of Physical Chemistry B* **117**, 12347–12359 (2013).
47. Ozgen, S., Kilinc, O. K. & Selamoglu, Z. *Antioxidant Activity of Quercetin: A Mechanistic Review. Turkish Journal of Agriculture-Food Science and Technology* vol. 4 www.agrifoodscience.com, (2016).
48. Oehlke, K., Heins, A., Stöckmann, H. & Schwarz, K. Impact of emulsifier microenvironments on acid-base equilibrium and activity of antioxidants. *Food Chem* **118**, 48–55 (2010).
49. Shang, Y. J. *et al.* Antioxidant capacity of curcumin-directed analogues: Structure-activity relationship and influence of microenvironment. *Food Chem* **119**, 1435–1442 (2010).
50. Galano, A., Alvarez-Idaboy, J. R. & Francisco-Márquez, M. Physicochemical insights on the free radical scavenging activity of sesamol: Importance of the acid/base equilibrium. *Journal of Physical Chemistry B* **115**, 13101–13109 (2011).
51. León-Carmona, J. R., Alvarez-Idaboy, J. R. & Galano, A. On the peroxy scavenging activity of hydroxycinnamic acid derivatives: Mechanisms, kinetics, and importance of the acid-base equilibrium. *Physical Chemistry Chemical Physics* **14**, 12534–12543 (2012).
52. Wadell, C., Bjork, E. & Camber, O. *Nasal Drug Delivery-Evaluation of an in Vitro Model Using Porcine Nasal Mucosa. European Journal of Pharmaceutical Sciences* vol. 7 (1999).
53. Gavini, E., Rassu, G., Sanna, V., Cossu, M. & Giunchedi, P. Mucoadhesive microspheres for nasal administration of an antiemetic drug, metoclopramide: in-vitro/ex-vivo studies. *Journal of Pharmacy and Pharmacology* **57**, 287–294 (2010).
54. Hauser, R. A. Levodopa: Past, present, and future. *European Neurology* vol. 62 1–8 Preprint at <https://doi.org/10.1159/000215875> (2009).

Chapter 7: Liposomes as DDSs for Vancomycin

7. Liposomes as Potential DDSs for Vancomycin

Antimicrobials – including antibiotics, antivirals, and antifungal – are medicines used to treat infectious diseases in humans, animals and plants. Since the 1950s, when the “golden era” of antibiotics began, Alexander Fleming had expressed concerns about the potential emergence of resistance if treatment is used for an inadequate amount of time.¹ Since then, there has been an increasing demand for new and novel antibiotics, in order to combat highly resistant strains that have been emerging. Antimicrobial resistance (AR) occurs when bacteria, viruses, and fungi no longer respond to antimicrobial medicines.² As a result, antibiotics and other antimicrobial medicines become ineffective and infections become difficult or impossible to treat, increasing the risk of disease spread, severe illness, disability and death.

The Global Research on Antimicrobial Resistance Project conducted the first known long-term study to estimate the global consumption of antibiotics. It covered 204 nations from years 2000–2018, and it was assessed a significant increase of 46% in the global antibiotic consumption rate was observed throughout this period of time.³ Without preventative measures, it is estimated that by 2050, AR could potentially become the world’s primary cause of death, with the forecast of 10 million deaths per year globally.⁴ Consequently, there is a compelling necessity to investigate and discover alternative antibacterial therapies, whether based on newer generations of antibiotics or through the revitalization of “old” antibiotics that are re-engineered to enhance their effectiveness. In this regard, using nanotechnology is one of the most promising ways to deal with these infectious diseases.

Antibiotics may lose their effectiveness against bacteria due to different molecular mechanisms employed by the microbial organisms:

- inactivation by an enzyme (bacteria produce new specific enzymes that can modify or deactivate antibiotics, making them ineffective);^{5,6}
- alteration in the antibiotic target (bacteria can modify the target sites that antibiotics interact with, involving changes in the structure of proteins or ribosomal RNA, and making the antibiotic unable to bind effectively);⁶
- efflux of drug (bacteria can pump out antibiotics using specialized efflux pumps, preventing the drugs from reaching effective concentrations within the cell);^{5,7}
- reduced uptake of antibiotics (changes in the permeability of bacterial cell membranes or the loss of specific channels can reduce the entry of antibiotics into the bacterial cell).⁷

Lipid-based nano systems, such as liposomes, can contribute to the battle against microbial resistance through various mechanisms. Liposomes, in fact, can protect antibiotics from enzyme degradation, guaranteeing their stability and effectiveness.⁸ Liposomes can also aid in overcoming bacterial efflux mechanisms: by encapsulating antibiotics within liposomes, these nanocarriers can evade or mitigate efflux pumps, allowing a more sustained interaction between the antibiotic and the target bacteria.⁶ Finally, liposomes can improve the penetration of antibiotics into bacterial cells:⁹ their lipid bilayer structure is similar to the bacterial cell membrane, and that may facilitate the fusion of liposomes with bacterial membranes. This fusion can enhance the entry of antibiotics into bacterial cells, overcoming reduced uptake. Furthermore, liposomes can be engineered for active targeting, where specific ligands or antibodies are attached to their surface. This targeting strategy enables liposomes to recognize and bind to specific receptors on bacterial cells, promoting selective uptake.¹⁰

Based on these premises, we designed and prepared liposomes aimed at the delivery of vancomycin (VAN), a potent antibiotic used to treat Gram+ bacterial infections.¹¹ It works by inhibiting the synthesis of the bacterial cell wall, leading to the disruption of the cell membrane and eventual cell death.¹² VAN is particularly effective against bacteria such as *Staphylococcus aureus* but, sadly, the rise of resistant bacteria has diminished the effectiveness of VAN against methicillin-resistant strains.¹³

At the aim of revert VAN resistance, our investigation focused on the preparation of various nanoscaled liposomal formulations consisting of saturated or unsaturated phospholipids and a combination of pH-sensitive and/or cationic species, that were prepared using two different preparation techniques. The physicochemical characteristics of liposome aggregates and, consequently, their biological fate,^{14–18} are significantly influenced by the molecular structure of liposome components^{19–22} and the methodology employed for their preparation and loading. These formulations were thoroughly characterized to assess their potential as DDS; finally, the best formulations in terms of dimensions, stability, and EE were tested against Gram-positive and Gram-negative organisms (*Staphylococcus aureus* and *E. coli*, respectively).

The systematic approach employed in this investigation aimed to deepen our understanding of the effects of variations in the molecular properties of liposome components associated with the preparation and loading technique of VAN.

7.1 Liposome Preparation and Characterization

Liposome formulations were prepared according to two different procedures: the Bangham method (*Thin Film Hydration*, TFH) and the *Reverse Phase Evaporation* (RPE) method. The TFH method is widely employed due to its simplicity, whereas the RPE method requires a multistep procedure (Figure 1). Briefly, in the TFH method, the aqueous medium (containing the hydrophilic drug) is directly

introduced to the lipid film obtained after the evaporation of organic solvents. The mixture is then vortexed to yield MLVs. On the other hand, in the RPE technique, the lipid film is re-dissolved in organic solvent or a mixture of organic solvents (we used methyl t-butyl ether). The aqueous medium (containing the hydrophilic drug) is then added, resulting in a two-phase system. After sonication, a homogeneous dispersion is obtained. Subsequently, the organic solvent is gradually evaporated, transforming the system into a viscous gel composed of inverted micelles, ultimately forming a liposome-containing aqueous dispersion.²³

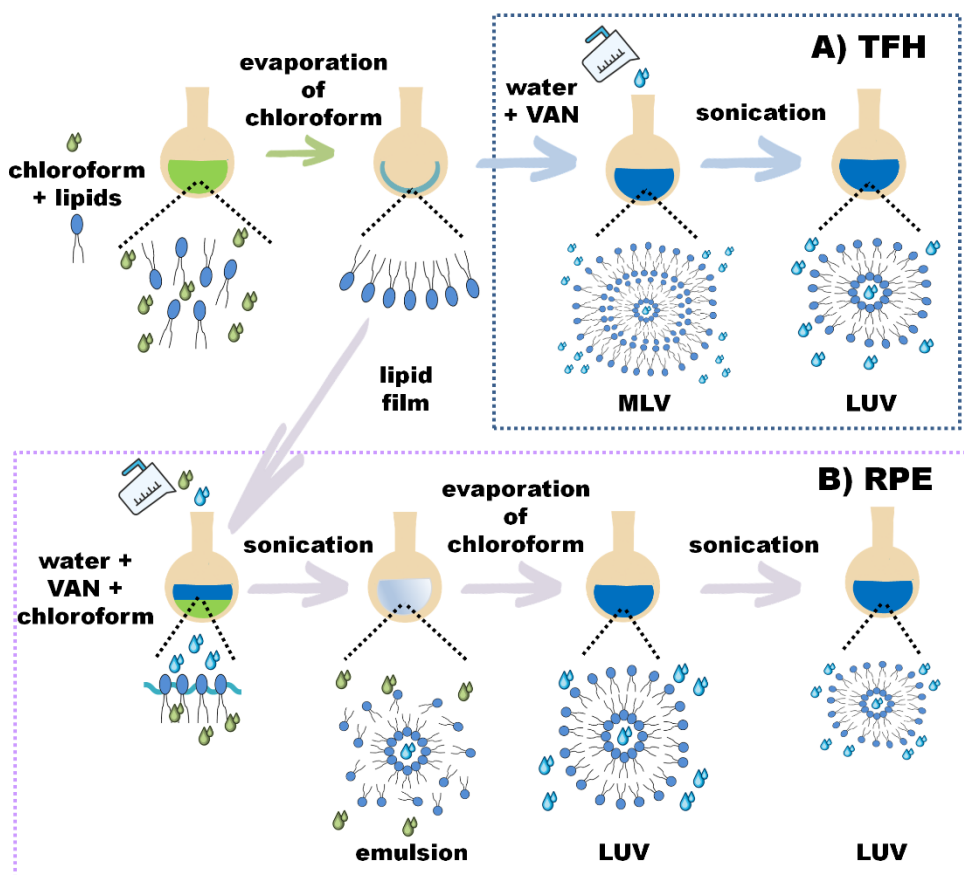


Figure 1. Schematic illustration of (A) TFH and (B) RPE liposome preparation methodology.

In contrast to the TFH method, the RPE technique presents the advantage of achieving higher internal aqueous loading,²⁴ a crucial aspect when liposomes are employed as DDSs for hydrophilic drugs.

In the first step of our investigation, VAN-loaded liposomes were formulated using five distinct phospholipids: DMPC, DPPC, DOPC, POPC, and EPC (Chart 1).

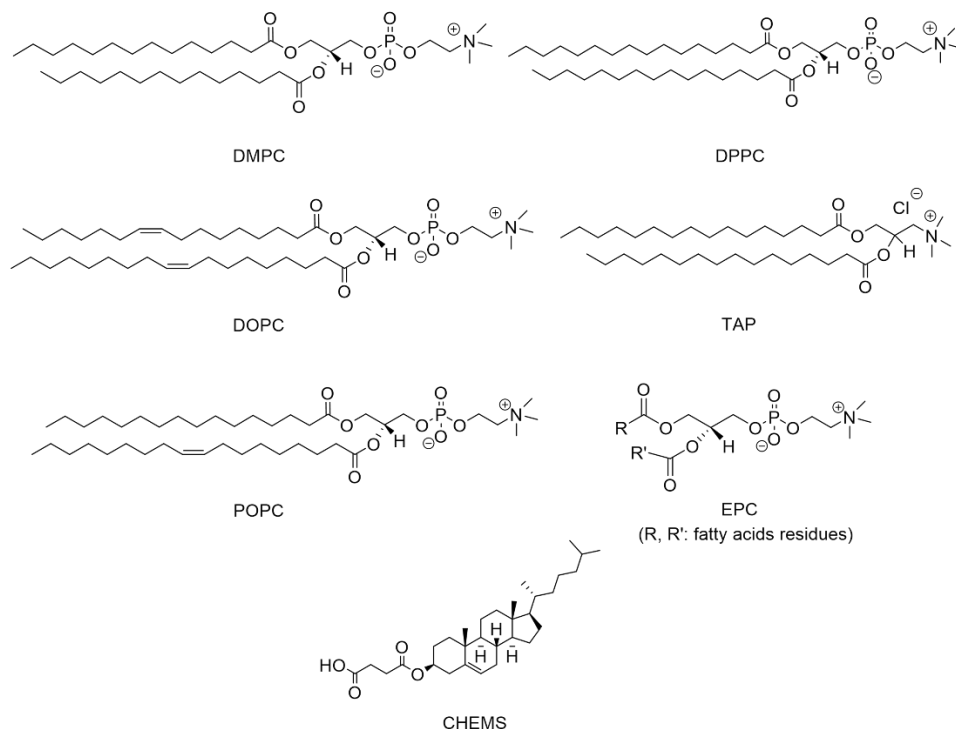


Chart 1. Liposome components.

DMPC and DPPC are saturated phospholipids, differing in the length of their alkyl chains. DOPC and POPC, on the other hand, are unsaturated phospholipids, varying in alkyl chain length, the number of unsaturations, and the position of double bonds. Finally, EPC is a mixture of different unsaturated phospholipids.

All liposome formulations (whether loaded or not) prepared using the TFH method followed by sonication, resulted in monodisperse populations with an average diameter of 100 nm and PDI values lower than 0.25, as determined by DLS

measurements. The same formulations, obtained by RPE method, showed different distributions depending on their formulation, as reported in Table 1.

Table 1. Size (expressed in nm, and obtained from intensity weighted distributions) and PDI of the investigated formulations obtained by RPE technique in the presence or in the absence of VAN. Reported values correspond to the average values over 3 measurements.

	empty formulations		loaded formulations	
	Size	PDI	Size	PDI
DPPC	129 ± 14	0.21	138 ± 17	0.23
DMPC	122 ± 16	0.28	133 ± 14	0.27
DOPC	637 ± 150	0.71	650 ± 125	0.75
POPC	757 ± 100	0.62	730 ± 130	0.65
EPC	830 ± 140	0.59	810 ± 110	0.62

No differences were observed between empty and loaded formulations. Liposomes formulated with saturated lipids were monodisperse, similar to what was observed in the case of TFH. On the other hand, liposomes prepared with unsaturated lipids were polydisperse. To verify if this result could be ascribed to the organic solvent used in their preparation, we replaced methyl t-butyl ether with diisopropyl ether, ethyl acetate or diethyl ether (each with or without chloroform), but we obtained polydisperse liposomal dispersions in all cases.

Considering the results obtained in terms of diameter and PDI, we decided to use DPPC as the main phospholipid. We decided to prepare mixed formulations by combining DPPC with a cationic lipid (TAP, Chart 1) to make the formulation positively charged and favor their interaction with negatively charged target cells, and a pH-sensitive cholesterol (CHEMS, Chart 1) to increase vesicles stability²⁵ and impart them a fusogenic behavior (making them pH sensitive).²⁶ A ternary mixture of lipids (DPPC/CHEMS/TAP at 4:3:3 molar ratio) was also prepared to evaluate the combined effect of CHEMS and TAP on liposome properties.

As in the previous cases, all the formulations prepared according to the TFH method followed by sonication showed an average diameter of 100 nm and PDI values lower than 0.25. Interestingly, the DPPC/TAP 7:3 formulation underwent gelation after sonication, observed either in the presence and in the absence of VAN (Figure 2).

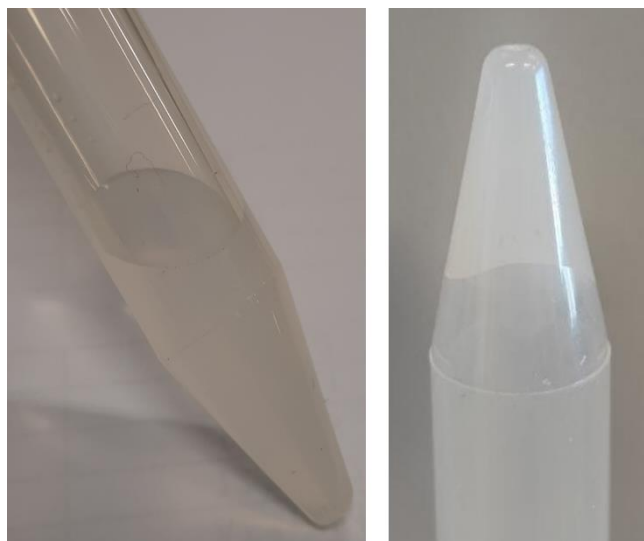


Figure 2. DPPC/TAP 7:3 liposomes prepared by TFH method before (on the left) and after sonication (on the right).

The size of the formulations obtained by RPE are reported in Table 2.

Table 2. Size (expressed in nm, and obtained from intensity weighted distributions) and PDI of the investigated formulations obtained by RPE technique in the presence or in the absence of VAN. Reported values correspond to the average values over 3 measurements.

	empty formulations		loaded formulations	
	Size	PDI	Size	PDI
DPPC	129 ± 14	0.21	125 ± 17	0.21
DPPC/TAP 7:3	153 ± 13	0.36	147 ± 15	0.34
DPPC/CHEMS 6:4	120 ± 21	0.13	125 ± 18	0.15
DPPC/TAP/CHEMS 4:3:3	151 ± 16	0.31	145 ± 20	0.33

SAXS experiments were performed to evaluate the lamellarity of the formulations. The SAXS profile of formulations prepared through the TFH method revealed a singular population of unilamellar vesicles, whereas the SAXS profile of formulations prepared through the RPE method showed a prevalent composition of unilamellar vesicles alongside a minor fraction of multilamellar vesicles (an example is reported in Figure 3A). The presence of a single bilayer was assessed also in sonicated DPPC/TAP 7:3 formulation (Figure 3B).

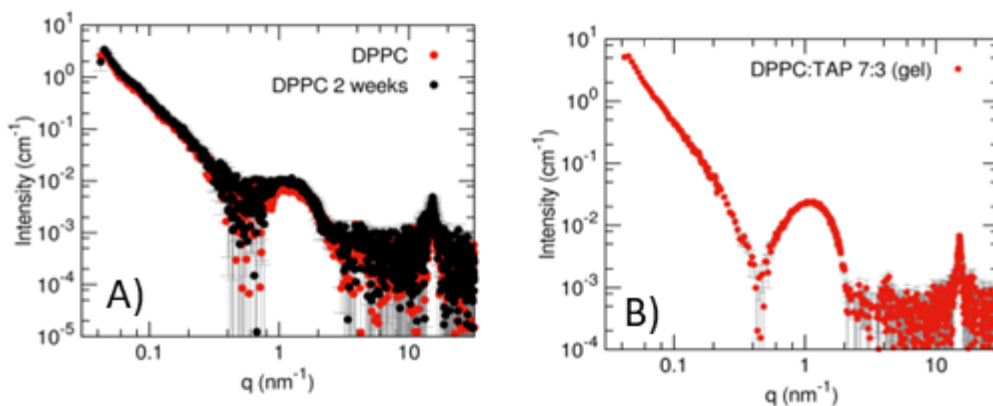


Figure 3. SAXS profile of A) DPPC vesicles prepared according to RPE technique, and B) sonicated DPPC/TAP 7:3 vesicles prepared according to TFH.

Generally, the gelation of a liposomal dispersion can be triggered by the introduction of long-chain alcohols or glycerol with different substitutions.^{27,28} This process relies on the unfolding of vesicles, typically formulated with at least two components, resulting in the formation of uniformly distributed sheetlike structures within water layers, forming a network. The occurrence of this phenomenon is closely tied to liposome composition and is observed within a specific composition range. It is typically noted in liposomes characterized by highly packed rigid bilayers.²⁹ Surface charge and surface charge density also play crucial roles in liposome gelation, influencing the intrabilayer interaction among headgroups within the aqueous network. Our findings suggest that, in the case of DPPC/TAP 7:3 liposomes, the opening of closed aggregates induced by sonication

creates optimal conditions for gel formation in terms of bilayer rigidity and surface charge.

Despite the monodispersity and low PDI values observed in DPPC and mixed formulations prepared according RPE, we chose to sonicate all the formulations to avoid potential issues in future tests with bacterial cells. In a previous study, in fact, we observed that even a small fraction of MLVs posed challenges in estimating the minimum inhibitory concentration (MIC) in the presence of aggregates. The sonicated formulation prepared with RPE exhibited a reduction of approximately 20% in dimensions, and similar to the TFH method, gelation was observed in DPPC/TAP 7:3 samples.

All the formulation prepared according to RPE method were stable for at least two months at room temperature, while the same formulation prepared according to TFH method showed an increase in PDI values over time.

We investigated the nanovesicles morphology by electron microscopy measurements. In Figure 4A, an image obtained from the investigation of DPPC/TAP/CHEMS 4:3:3 after sonication is presented as an example. Similar images were obtained with sonicated nanoscaled liposomes of other formulations, excluding sonicated 7:3 liposomes. The dimensions of nanoliposomes obtained with electron microscopy are consistent with those identified by DLS measurements. In Figure 4B and 4C, STEM images of DPPC/TAP 7:3 liposomes before and after sonication are depicted. It is evident that the aggregates present in the sample vanished upon sonication, leading to gelation.

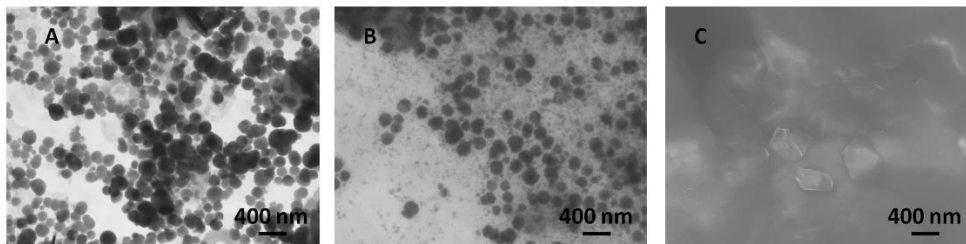


Figure 4. STEM images of (A) DPPC/TAP/CHEMS 4:3:3 liposomes before sonication, (B) DPPC/TAP 7:3 liposomes before sonication, and (C) DPPC/TAP 7:3 liposomes after sonication.

Given the obtained results, we opted to delve deeper into nanoscaled liposomes, specifically those composed of DPPC alone or in combination with CHEMS and/or TAP, to explore their potential as DDSs for VAN.

7.2 VAN entrapment

VAN was incorporated during the formation of liposomes through passive loading. The EE achieved through TFH method was notably low, not exceeding 3 molar percentage (equivalent to less than 90 $\mu\text{g}/\text{mL}$). However, when employing RPE technique, the EE significantly increased to approximately 15 molar percentage (around 450 $\mu\text{g}/\text{mL}$), with no significant differences observed based on the liposome composition. Our results are in line with expectations. It is well-documented in literature that the EE of hydrophilic drugs in liposomes is notably high when prepared through RPE procedure.³⁰ Conversely, in the TFH method, a higher EE is typically observed with hydrophobic compounds. This phenomenon could be elucidated by the microemulsions formed during sonication and solvent evaporation in the RPE procedure, facilitating the encapsulation of a relatively larger amount of water and, consequently, the solute dissolved within. It's worth noting that a previous study in the literature also reported a higher EE for liposomal VAN using RPE compared to TFH.³¹

7.3 Liposome Transition Temperature

To enhance our understanding of the physicochemical characteristics of the bilayer, we conducted DSC measurements on the formulations, whether empty or loaded with VAN, prepared through either TFH or RPE methods.

As expected, the inclusion of CHEMS at a 40 molar percentage in the formulations abolished the main transition, resulting in the absence of peaks in the thermograms.

The thermograms and calorimetric data for the remaining samples, prepared via TFH or RPE, with or without VAN, are provided in Figure 5 and Table 3.

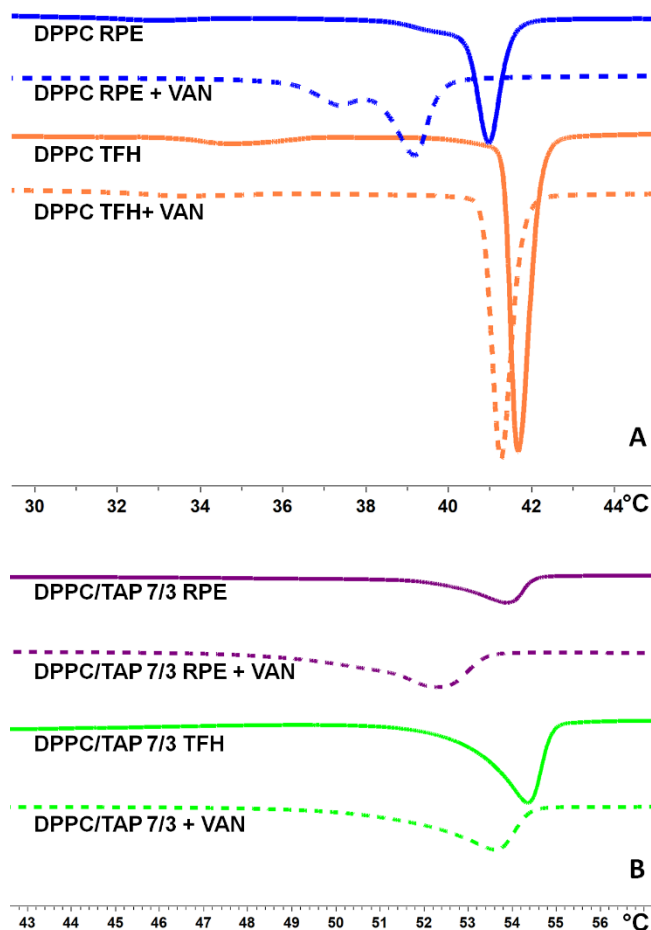


Figure 5. Thermograms of the investigated formulation prepared according A) TFH, and B) RPE techniques.

Table 3. Thermodynamic parameters obtained by DSC measurements on empty and loaded liposome formulations. Uncertainties are ± 0.1 °C for the temperature values and ± 5 KJ/mol for the ΔH_m values. ^a Formulations prepared according to TFH method, ^b formulations prepared according to RPE method.

Formulation (9:1)	T _p (°C)	T _m (°C)	ΔH (KJ/mol)
^a DPPC		41.0	19
^a DPPC + VAN	/	39.2	22

^a DPPC/TAP 7:3	/	54.0	10
^a DPPC/TAP 7:3 + VAN	/	52.4	20
^b DPPC		41.7	33
^b DPPC + VAN	/	41.2	26
^b DPPC/TAP 7:3	/	54.4	26
^b DPPC/TAP 7:3 + VAN	/	53.7	20

Lipids within empty nanoliposomes (with or without TAP) prepared via the TFH method exhibit a more efficient packing compared to those in liposomes generated through the RPE method, as indicated by the ΔH values. This reaffirms that the choice of the preparation method can significantly impact lipid organization.

In the case of DPPC liposomes, the presence of VAN abolished the pretransition and induces a slight reduction in T_m . The influence of the preparation method extends beyond lipid packing, affecting the interaction of VAN. In VAN-loaded nanovesicles prepared via RPE, a noticeable broadening of the peak and appearance of a shoulder are observed, suggesting a strong interaction between VAN's sugar and polar moieties with the lipid polar headgroups. The emergence of a shoulder in the presence of VAN implies that the sugar moieties likely influence lipid organization. Near T_m , sugars can dehydrate lipids, leading to a partial delayed melting³² and membrane thinning, resulting in the formation of a disordered, glassy state in the hydrophobic core of the bilayer.³³ This glassy phase formation could explain the reduction in ΔH value, primarily associated with van der Waals interactions among lipid chains. Conversely, when VAN is loaded into liposomes prepared via TFH, the shape of the peak remains unchanged. These results may be attributed to the more efficient lipid packing in the bilayer in liposomes prepared by TFH compared to liposomes prepared with RPE, resulting in a diminished impact of VAN in the aqueous phase. Another plausible explanation could be associated with the higher

quantity of liposomal VAN in aggregates formed with RPE compared to TFH. The increase in ΔH value suggests that, nonetheless, the presence of the drug disrupts lipid organization, although not to a significant extent as observed with the RPE method. It's noteworthy that in the case of liposomes prepared with TFH, the amount of VAN entrapped in the aggregates is lower than that in the corresponding liposomes prepared with RPE, potentially reducing the overall impact of the drug for this reason.

The incorporation of 30 molar percentage of TAP results in a notable elevation of T_m (more than 10 °C) and ΔH values, accompanied by a broadening of the peak. This indicates a significant impact of this cationic lipid on lipid organization. Even in these samples, the presence of VAN leads to a reduction in T_m compared to empty nanoliposomes, without any apparent shoulder in the thermograms. This distinction is likely attributed to weaker interactions among alkyl chains of DPPC and TAP than those among alkyl chains of DPPC alone. The influence of the sugar moieties of VAN on lipid packing appears to be less pronounced.

7.4 Antimicrobial activity of VAN-loaded liposomes

The antimicrobial activity of VAN encapsulated in sonicated DPPC, DPPC/CHEMS 6:4, and DPPC/CHEMS/TAP 4:3:3 nanoscaled liposomes was evaluated against *S. aureus* and *E. coli*, and compared to free VAN. The efficiency of the DPPC/TAP 7:3 formulation could not be determined due to its gel-phase after sonication, which impeded assessment. Nevertheless, given its gelation after sonication, it holds promise as a drug delivery system for topical treatment, as reported in the literature for other liposomal gels.³⁴⁻³⁷

We also opted to exclusively assess formulations prepared through the RPE method, given the superior EE of vancomycin and the stability of the formulations over time.

All formulations were ineffective against *E. coli*, which was not surprising considering its challenging penetration due to the Gram-negative outer membrane and the lack of activity of free VAN on these pathogens at an acceptable MIC.

VAN loaded in DPPC nanoliposomes exhibited no biological activity against *S. aureus*, while DPPC/CHEMS 6:4 and DPPC/CHEMS/TAP 4:3:3 vesicles demonstrated a MIC (1.4 and 1.3 µg/mL, respectively) comparable to that of free VAN (1.0 µg/mL). The corresponding empty formulations did not exhibit any bactericidal activity. This outcome suggests that these mixed fusogenic formulations could serve as suitable carriers for VAN delivery, potentially expanding its therapeutic scope, although the specific contributions of CHEMS and TAP remain uncertain. This, in turn, broadens the potential of these formulations as delivery systems for other active ingredients that might face limitations in their current form.

7.5 Conclusion

To address the growing failure of antimicrobial therapies, one potential strategy is the use of effective DDSs capable of overcoming pathogen resistance to active substances. In this context, various nanoscaled liposomal formulations, composed of saturated or unsaturated phospholipids along with mixed pH-sensitive and/or cationic molecules, were prepared using the TFH or RPE procedures. In this study, a systematic approach was adopted to enhance our understanding of how variations in the molecular properties of liposome components, influenced by the preparation techniques, impact the potential of these formulations as DDSs. The results highlight i) the critical role of lipid molecular structure (which affects lipid organization and aggregate charge), and ii) the methodology used for liposome formulation (that may play a pivotal role in determining lipid organization and entrapping efficiency) in determining liposome properties and their biological efficacy as DDSs. The observed bactericidal activity in certain mixed formulations,

comparable to that of free VAN, suggests their potential utility as effective DDSs for VAN.

7.6 Bibliography

1. Nicolosi, D. *et al.* Innovative Phospholipid Carriers: A Viable Strategy to Counteract Antimicrobial Resistance. *International Journal of Molecular Sciences* vol. 24 Preprint at <https://doi.org/10.3390/ijms242115934> (2023).
2. Tang, K. W. K., Millar, B. C. & Moore, J. E. Antimicrobial Resistance (AMR). *British Journal of Biomedical Science* vol. 80 Preprint at <https://doi.org/10.3389/bjbs.2023.11387> (2023).
3. Browne, A. J. *et al.* Global antibiotic consumption and usage in humans, 2000–18: a spatial modelling study. *Lancet Planet Health* **5**, e893–e904 (2021).
4. *TACKLING DRUG-RESISTANT INFECTIONS GLOBALLY: FINAL REPORT AND RECOMMENDATIONS THE REVIEW ON ANTIMICROBIAL RESISTANCE CHAIRED BY JIM O’NEILL.* (2016).
5. Munita, J. M. & Arias, C. A. Mechanisms of Antibiotic Resistance. *Microbiol Spectr* **4**, (2016).
6. Ghosh, R. & De, M. Liposome-Based Antibacterial Delivery: An Emergent Approach to Combat Bacterial Infections. *ACS Omega* vol. 8 35442–35451 Preprint at <https://doi.org/10.1021/acsomega.3c04893> (2023).
7. Kapoor, G., Saigal, S. & Elongavan, A. Action and resistance mechanisms of antibiotics: A guide for clinicians. *Journal of Anaesthesiology Clinical Pharmacology* vol. 33 300–305 Preprint at https://doi.org/10.4103/joacp.JOACP_349_15 (2017).
8. Ferreira, M. *et al.* Liposomes as antibiotic delivery systems: A promising nanotechnological strategy against antimicrobial resistance. *Molecules* **26**, (2021).
9. Ferreira, M. *et al.* Liposomes as a nanoplatform to improve the delivery of antibiotics into staphylococcus aureus biofilms. *Pharmaceutics* **13**, 1–25 (2021).
10. Zou, W., McAdorey, A., Yan, H. & Chen, W. Nanomedicine to overcome antimicrobial resistance: challenges and prospects. *Nanomedicine* vol. 18 471–484 Preprint at <https://doi.org/10.2217/nnm-2023-0022> (2023).

11. Levine, D. P. *Vancomycin: A History*.
https://academic.oup.com/cid/article/42/Supplement_1/S5/275962.
12. Mohammad, H. *et al.* Phenylthiazole Antibacterial Agents Targeting Cell Wall Synthesis Exhibit Potent Activity in Vitro and in Vivo against Vancomycin-Resistant Enterococci. *J Med Chem* **60**, 2425–2438 (2017).
13. Boswihi, S. S. & Udo, E. E. Methicillin-resistant *Staphylococcus aureus* : An update on the epidemiology, treatment options and infection control. *Curr Med Res Pract* **8**, 18–24 (2018).
14. Giuliani, C. *et al.* Remote loading of aloe emodin in gemini-based cationic liposomes. *Langmuir* **31**, 76–82 (2015).
15. Giansanti, L. *et al.* Influence of lipid composition on the ability of liposome loaded voacamine to improve the reversion of doxorubicin resistant osteosarcoma cells. *Chem Phys Lipids* **223**, 104781 (2019).
16. Som, A. & Tew, G. N. Influence of lipid composition on membrane activity of antimicrobial phenylene ethynylene oligomers. *Journal of Physical Chemistry B* **112**, 3495–3502 (2008).
17. Battista, S. *et al.* Curcuminoids-loaded liposomes: influence of lipid composition on their physicochemical properties and efficacy as delivery systems. *Colloids Surf A Physicochem Eng Asp* **597**, (2020).
18. Bozzuto, G. & Molinari, A. Liposomes as nanomedical devices. *Int J Nanomedicine* **10**, 975–999 (2015).
19. Villalva, D. G., Giansanti, L., Mauceri, A., Ceccacci, F. & Mancini, G. Influence of the state of phase of lipid bilayer on the exposure of glucose residues on the surface of liposomes. *Colloids Surf B Biointerfaces* **159**, 557–563 (2017).
20. Gradella Villalva, D. *et al.* Molecular Packing in Langmuir Monolayers Composed of a Phosphatidylcholine and a Pyrene Lipid. *Journal of Physical Chemistry B* **120**, 1126–1133 (2016).
21. Scindia, Y., Silbert, L., Volinsky, R., Kolusheva, S. & Jelinek, R. Colorimetric detection and fingerprinting of bacteria by glass-supported lipid/polydiacetylene films. *Langmuir* **23**, 4682–4687 (2007).
22. Barry, J. *et al.* Determining the effects of lipophilic drugs on membrane structure by solid-state NMR spectroscopy: The case of the antioxidant curcumin. *J Am Chem Soc* **131**, 4490–4498 (2009).

23. Szoka, F. & Papahadjopoulos, D. Procedure for preparation of liposomes with large internal aqueous space and high capture by reverse-phase evaporation. *Proc Natl Acad Sci U S A* **75**, 4194–4198 (1978).
24. Dhiman, J. Novel Drug Delivery System: Brief Review. *Journal of Drug Delivery and Therapeutics* **13**, 188–196 (2023).
25. Talsma, H. *et al.* The influence of the molar ratio of cholesteryl hemisuccinate/dipalmitoylphosphatidylcholine on 'liposome' formation after lipid film hydration. *Chem Phys Lipids* **62**, 105–112 (1992).
26. Hafez, I. M. & Cullis, P. R. Cholesteryl hemisuccinate exhibits pH sensitive polymorphic phase behavior. *Biochim Biophys Acta Biomembr* **1463**, 107–114 (2000).
27. Nakagawa, Y., Nakazawa, H. & Kato, S. Mechanism of gelation in the hydrogenated soybean lecithin (PC70)/hexadecanol/water system. *J Colloid Interface Sci* **376**, 146–151 (2012).
28. Gräbner, D. *et al.* Hydrogels from phospholipid vesicles. *Adv Colloid Interface Sci* **208**, 252–263 (2014).
29. Nakagawa, Y., Ohta, M., Nakazawa, H. & Kato, S. Requirement of charged lipids for the hexadecanol-induced gelation in the phospholipid bilayer system. *Colloids Surf A Physicochem Eng Asp* **443**, 272–279 (2014).
30. Lombardo, D. & Kiselev, M. A. Methods of Liposomes Preparation: Formation and Control Factors of Versatile Nanocarriers for Biomedical and Nanomedicine Application. *Pharmaceutics* **14**, (2022).
31. Gonzalez Gomez, A., Syed, S., Marshall, K. & Hosseinidoust, Z. Liposomal Nanovesicles for Efficient Encapsulation of Staphylococcal Antibiotics. *ACS Omega* **4**, 10866–10876 (2019).
32. Morandi, M. I. *et al.* DPPC Bilayers in Solutions of High Sucrose Content. *Biophys J* **114**, 2165–2173 (2018).
33. Dhaliwal, A., Khondker, A., Alsop, R. & Rheinstädter, M. C. Glucose can protect membranes against dehydration damage by inducing a glassy membrane state at low hydrations. *Membranes (Basel)* **9**, 20–26 (2019).
34. Jindal, S., Awasthi, R., Singhare, D. & Kulkarni, G. T. Topical delivery of Tacrolimus using liposome containing gel: An emerging and synergistic approach in management of psoriasis. *Med Hypotheses* **142**, 109838 (2020).

35. Jøraholmen, M. W., Basnet, P., Tostrup, M. J., Moueffaq, S. & Škalko-Basnet, N. Localized therapy of vaginal infections and inflammation: Liposomes-in-hydrogel delivery system for polyphenols. *Pharmaceutics* **11**, 1–19 (2019).
36. Jain, H. *et al.* Liposome mediated topical delivery of Ibrutinib and Curcumin as a synergistic approach to combat imiquimod induced psoriasis. *J Drug Deliv Sci Technol* **68**, 103103 (2022).
37. Mitkari, B. V., Korde, S. A., Mahadik, K. R. & Kokare, C. R. Formulation and evaluation of topical liposomal gel for fluconazole. *Indian Journal of Pharmaceutical Education and Research* **44**, 324–333 (2010).

Chapter 8: Lipid Mesophases as DDSs

8. LMPs-based Injectable Beads as a New and Versatile Drug Delivery Platform for Sustained Release

Medical drugs are rarely administered in a single dose: quite often, their concentration quickly falls below the minimum effective concentration, with a decline in therapeutic effect. A larger dose may cause toxic side reactions, while multiple dosing causes fluctuation of drug concentration reducing the patients' compliance. As explained before, DDSs offer the advantage of sustained and controlled release, lowering the dosing frequency without altering the desired effect on molecular targets and reducing side effects in patients.

Among all the different classes of drug carriers, LMPs show unique material properties and functionality, already reported in Section 2.3. An additional advantage is that they are prepared through a single-step process by mixing monoacyl glycerol lipids (such as MO, Chart 1) with water.

LMPs are thermodynamically stable structures and, thanks to their high degree of order, they are less prone to fusion, leakage or aggregation compared to other lipid-based DDSs, thus they are particularly appealed as a depot system to be applied locally.¹ In addition, the release property of the formulation can be tuned by modulating the size of the water channel and the phase symmetry of the mesophase by adding additives such as the antioxidant Vitamin E (VitE, Chart 1).²⁻⁸ Compared to liposomes, the ordered arrangement of lipids in the mesophase allows for a more efficient packing of drugs, increasing either their loading capacity and/or their retention into the gel.⁹ Moreover, in contrast to other gel-based drug carriers, LMPs could prevent the initial burst release resulting from the swelling process,¹⁰ as the lamellar phase (L, which forms at low water percentages) has a lower diffusion coefficient compared to more hydrated topologies.^{2,11}

In 2012 Barenholz and his group prepared alginate- or chitosan-based beads containing bupivacaine (BUPI)-loaded liposomes.¹² This approach enabled the reduction of considerable drug leakage from liposomes that occurred during liposomes storage, hindering their clinical application despite their potential as extremely long-acting local anesthetics. Their beads also showed the advantage of an easy removal of the storage medium, addressing the challenge of separating liposomes from free drug before administration.

In general, beads show a high surface/volume ratio, and particles with a high surface/volume ratio usually tend to exhibit great strength and stability, enhancing an overall structural integrity, and have an increased surface interaction.

Inspired by Barenholz's works and having in mind the potential of LMPs, we prepared, for the first time, LMPs-based beads using MO in the absence or presence of different percentages of VitE with the aim of formulating a new drug delivery platform meant for local administration. In our case, an additional advantage worth noting is that LMPs-based beads can be readily produced in large quantities through a straightforward manual technique. Consequently, the scalability and reproducibility of bead production could make them more suitable for large-scale manufacturing. In contrast, LMPs-based bulk gels can be more challenging to handle and may require specialized application techniques.

We selected four model drugs (Tofacitinib citrate, TOFA; Rapamycin, RAPA; Gefitinib, GEFI; and BUPI, Chart 1) to load into the beads and demonstrate the beads' potential as novel drug delivery platform. These drugs were chosen based on their diverse physicochemical properties, distinct sites of action, varied routes of administration, and current applications in different therapeutic contexts. Specifically: TOFA is a hydrophilic Janus Kinase inhibitor commonly employed to treat autoimmune diseases like rheumatoid arthritis,^{13,14} RAPA is a hydrophobic immunosuppressant employed to treat rheumatoid arthritis,¹⁵⁻¹⁷ GEFI is a hydrophobic anti-tumor drug with good potential for the treatment of metastatic

colorectal cancer,^{18,19} and BUPI is a potent hydrophilic local anesthetic.²⁰⁻²² The loaded beads could potentially be administered to the target site via an intra-articular injection for TOFA and RAPA, an intraperitoneal injection for GEFI, and a subcutaneous injection for BUPI, aiming to circumvent their systemic administration and thereby reduce potential side effects.

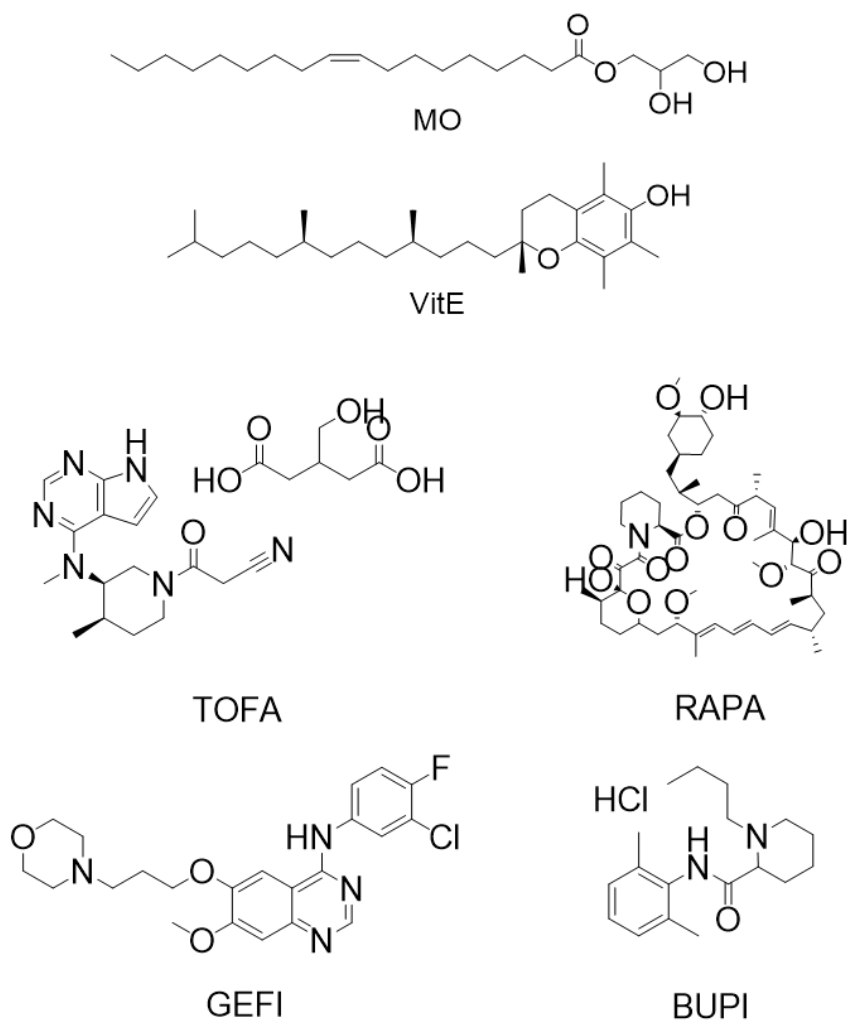


Chart 1. Structures of MO, VitE, TOFA, RAPA, BUPI, and GEFI.

8.1 Preparation and Characterization of the Beads

MO was selected as the primary lipid for bead preparation, and it was combined with different percentages of the antioxidant VitE. Acting as a stiffener for lipid chains, VitE facilitates the creation of highly viscous hexagonal phases (H_{II}) or inverted micellar phases.^{2,3,6,23–25} The addition of 20% (w/w) or 45% (w/w) of VitE to MO enabled the attainment of H_{II} and inverse micelle-based beads, structures that MO alone could not form. However, while the H_{II} -based beads (MO/VitE-B) are stable and maintain their shape over time, the others exhibited instability and a tendency to aggregate within a brief time, limiting their application as DDS. Morphology and surface of hydrated MO-based beads (MO-B) and MO/VitE-B were investigated using optical and a Scanning Electron Microscope (SEM) equipped with a Peltier cooling device, which allows the investigation of samples in conditions more similar to the real ones. Representative images of MO-B and MO/VitE-B are reported in Figure 1.

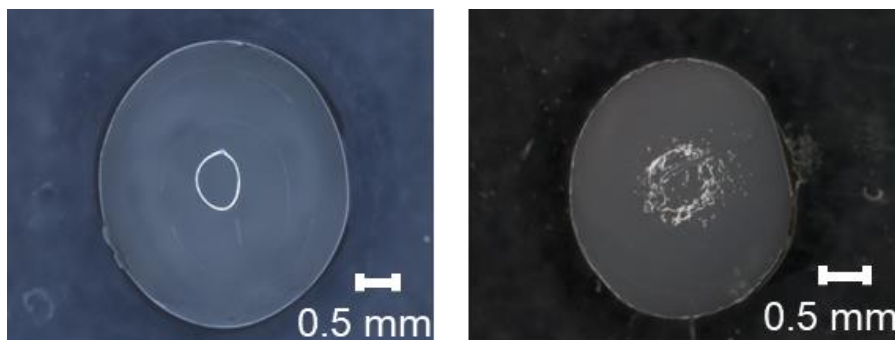


Figure 1. representative images of MO-B (on the left) and MO/VitE-B (on the right).

The spherical nature of the beads and their mean diameter (≈ 3 mm) is evident in the optical microscope pictures (Figure 1), while SEM put in evidence that the surface roughness is more pronounced in pure MO-B compared to smoother and gel-like texture of MO/VitE-B (Figure 2). In both cases, the production process allowed us to obtain batches with low variability in terms of size and weight.

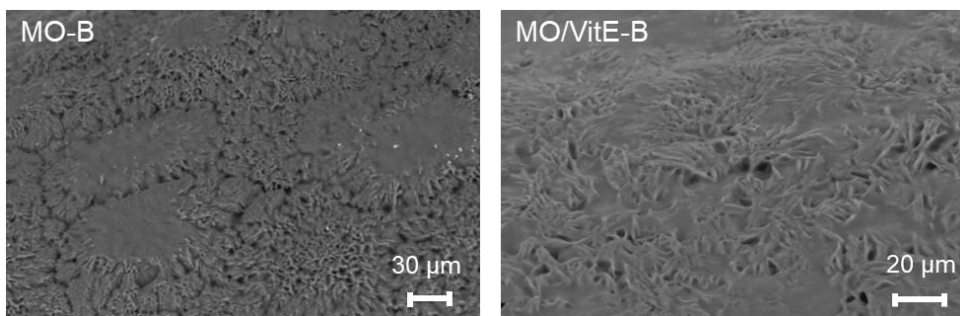


Figure 2. Surface of MO-B (on the left) and MO/VitE-B (on the right).

Since the beads were formed by dropping molten lipid in water, to deepen our knowledge on the internal structure and symmetry of the beads at different hydration times, and thus gain information about the kinetics of swelling, we investigated changes in mesophase structure and transitions by SAXS measurements. In the context of LMPs, SAXS provides valuable information about the spatial arrangement and ordering of lipid molecules at the nanoscale level; each phase exhibits distinctive scattering patterns, thus SAXS can be used to identify different topologies. According to Figure 3a, MO-B exhibited a L phase between 10 and 20 min of hydration. Subsequently, a transition to an Ia3d phase occurred and it is completed in 10 min, while after 2 h the gel reached a fully hydrated Pn3m phase, in agreement with the phase diagram of MO.^{23,26}

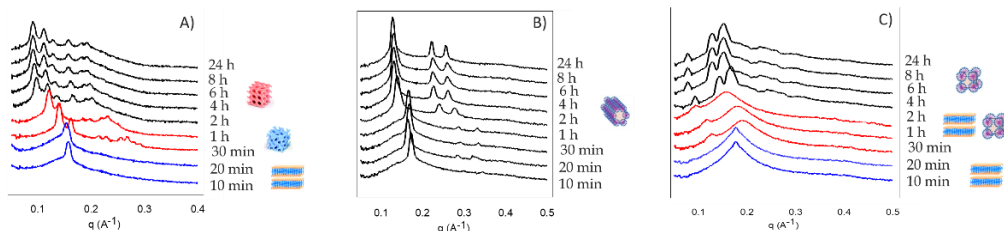


Figure 3. SAXS kinetic experiments on A) MO-B, B) MO-VitE-B and C) MO/VitE 55/45-B.

The swelling process of MO-B during time could be noticed by naked eye, as shown in Figure 4: L beads are milky-white, Ia3d beads show transparent sides, while Pn3m beads are entirely transparent.

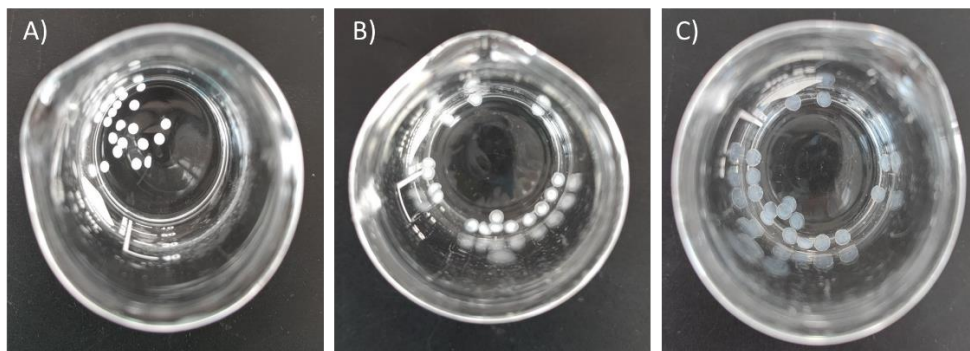


Figure 4. MO-B swelling during time.

The lattice parameters (a ; which refers to the spacing between repeating structural units) are ≈ 3 nm for the L phase, 11 nm for the Ia3d phase and roughly 9 nm for the Pn3m phase, while the water channel diameter (d_w) is approximately 2.5 nm and 4 nm for the Ia3d phase and the Pn3m phase, respectively, in good agreement with the bulk gel parameters reported in the literature.²³

Upon the addition of 20% (w/w) of VitE to MO, the beads promptly exhibit a stable H_{II} phase yet after 10 min, with a lattice of approximately 5 nm (Figure 3B) as expected from literature.³ Despite the instability observed in beads composed of MO/VitE 55/45, we successfully identified an inverse micellar phase after 2 h, in analogy with what observed in the bulk gel (Figure 3C).²⁷

While SAXS gave information about a short-range order, rheology measurements enabled us to predict the relation among stress, strain, and the rate of deformation of materials to characterize the mechanical properties of the beads. All the beads (independently from their hydration) show a shear thinning behavior (Figure 5) and the shape of G' and G'' (the storage and loss of moduli, respectively) exhibit a sharp downturn at the limit of the linear viscoelastic region. Above that, a strain increase

causes the disruption of the network, resulting in a decrease of both G' and G'' as evident in the representative amplitude sweep experiments (Figure 5).

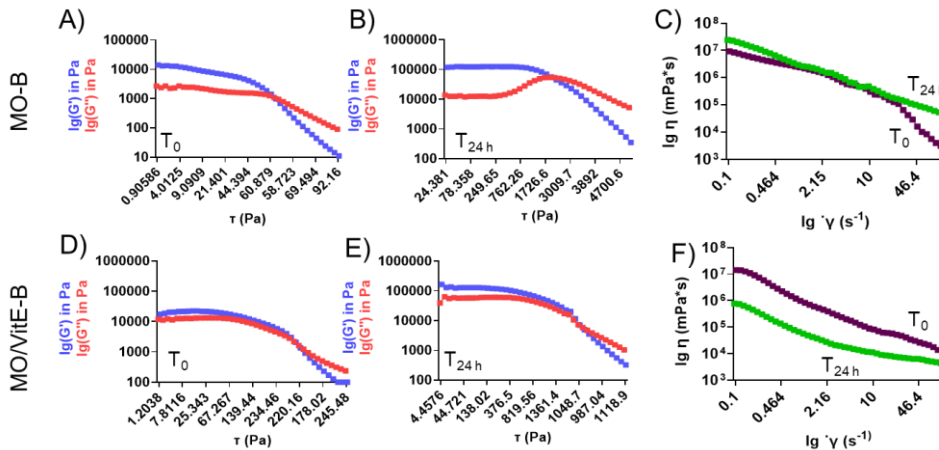


Figure 5. Rheology measurements on MO-B and MO/VitE-B.

Flow (τ_f) and yield point (τ_y) values, both related to the required force to be applied on the sample to induce flow, put in evidence that less hydrated beads (i.e. soon after their preparation) exhibit lower elasticity than the more hydrated ones, indicating that the beads are more easily injectable soon after their preparation (Figure 6).

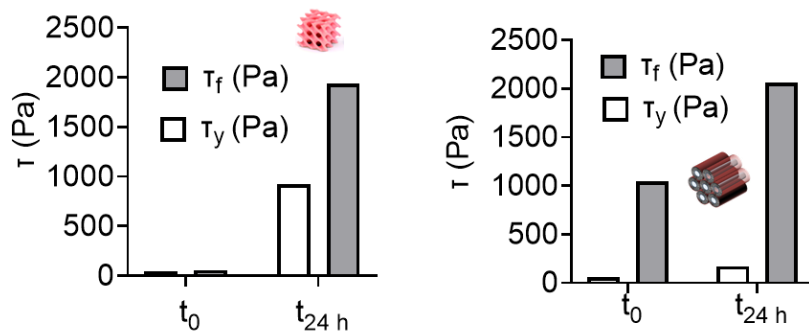


Figure 6. τ_f and τ_y values for MO-B (on the left) and MO/VitE-B (on the right) soon after their preparation (white bars) and after 24 h (grey bars).

More interestingly, considering that the shear during this process can affect the strength and the viscosity of the beads, thixotropy experiments (which refers to the time-dependent changes in viscosity or flow behavior of a material when subjected to repeated cycles of shear stress or deformation) were also conducted. The results demonstrate that soon after preparation MO-B exhibited a regeneration rate of 75%, whereas MO/VitE-B a regeneration rate of 17% (Figure7).

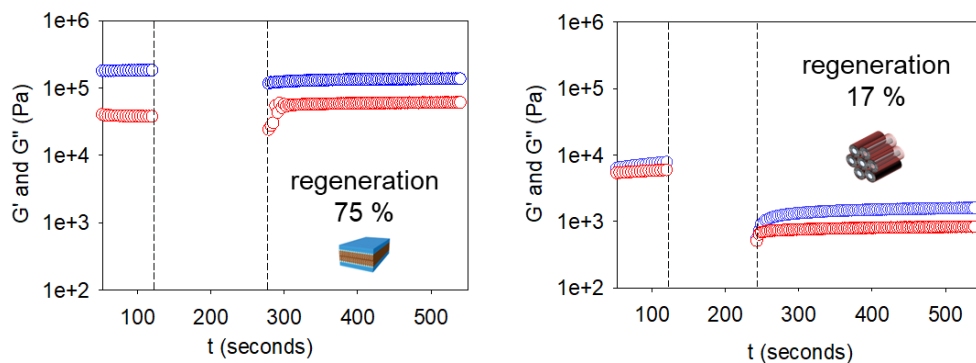


Figure 7. Thixotropy experiments on MO-B (on the left) and MO/VitE-B (on the right) soon after their preparation.

The underlying mechanism involves the reversible breakdown and reformation of structural elements within the material in the case of MO-B, while an important loss in regeneration was observed in the case of H_{II} beads. This information is critical for designing effective drug delivery systems that maintain their structural integrity, ensuring consistent and predictable drug release profiles: the injection of H_{II} beads could potentially result in the loss of their 3D structure, leading to a concurrent alteration in drug release dynamics.

8.2 Preparation and Characterization of Drug-loaded Beads

To assess the suitability of the beads as a drug delivery platform, we loaded four model drugs (TOFA, BUPI, GEFI and RAPA) with different polarity, physicochemical properties, mechanisms of action, and routes of administration at three distinct

initial ratios (0.1%, 1%, and 5% w/w with respect to MO). As expected, loaded beads maintained the same diameter of the unloaded ones (≈ 3 mm) and SAXS analysis (carried out after 24 h of hydration) put in evidence that the inclusion of TOFA, GEFI, and RAPA did not influence either the phase identity of the formulations (that remained all in Pn3m phase), or their structural parameters. As TOFA is a hydrophilic molecule and we anticipated a significant release rate from a cubic based-beads, we decided to load the drug into H_{II} beads as well: also in this case, TOFA did not induce any changes in the structure of the beads, as demonstrated with SAXS experiments.

Interestingly, when 5% (w/w) of drugs was loaded into the beads (Pn3m or H_{II}), SAXS patterns also showed a reflection at high q , that cannot be attributed to a Bragg's reflection. The presence of reflections in the WAXS spectra suggested indeed that this was due to the drug crystals (Figure 8).

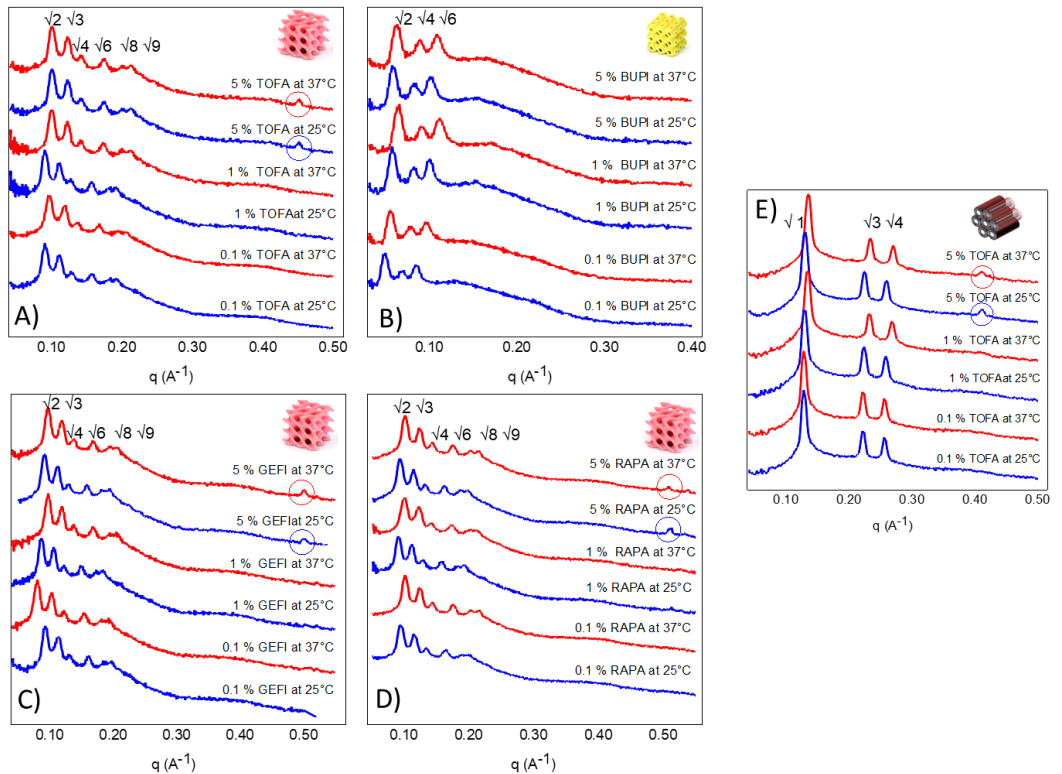


Figure 8. SAXS experiments on hydrated A) TOFA-, B) BUPI-, C) GEFI-, D) RAPA-loaded MO-B and E) TOFA-loaded MO/VitE-B at three different ratios at both 25 °C and 37 °C.

Differently, in the case of BUPI-loaded beads, a $Im\bar{3}m$ phase was obtained after 24 h of hydration for all three ratios (Figure 8B). We hypothesize that the amphiphilic nature and/or its highest polarity/water solubility caused its redistribution between the polar interface and the hydrophobic domains during hydration, with consequent formation of a primitive symmetry. Similarly, the loading of BUPI in glycerol monooleate systems caused a phase transition from $Pn\bar{3}m$ to H_{II} structures, as literature reports.²⁸ Structural parameters also varied: lattice reached 18 nm while d_w increased up to 8 nm, exceeding the value commonly observed in $Im\bar{3}m$ symmetry.²³ The absence of a reflection peak in the SAXS spectra at high q and in the WAXS spectra indicates that, differently from the other drugs, BUPI was in its amorphous state even when present at the highest ratio (5% w/w).

The topology of the mesophases (and their structural parameters) remains unaffected by temperature variations as evident from SAXS and WAXS analyses conducted at both 25 °C and 37 °C.

Our platform demonstrated the remarkable capacity to effectively vehiculate substantial quantities of drugs, achieving a remarkable entrapment efficiency exceeding 80% for both hydrophilic and hydrophobic drugs: starting from 0.1%, 1% or 5% formulations (1 mg, 10 mg, or 50 mg drug/1g of MO), each bead entrapped approximately 8 µg, 80 µg or 380 µg of the drug, respectively. Such high entrapment efficiency translates to a reduced requirement of formulation during administration and may result in a decrease in the frequency of administration, enhancing patient compliance.

DSC experiments allowed to determine the enthalpy changes associated to the phase transition and the temperatures at which it occurs. Before recording the heating thermograms, we incubated each sample below zero degrees to reduce the risk of undercooling of water in hydrated MO and to stabilize the L phase (when present).²⁹ Thermograms of MO-B (Figure 9) for each topology showed endothermic transitions between 10-15 °C.

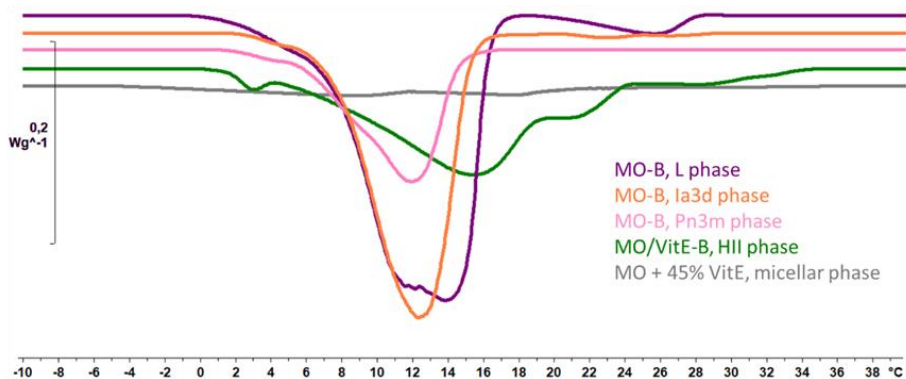


Figure 9. Thermograms of MO-B (Figure 9) for each topology.

The ΔH values associated with the observed peaks are reported in Table 1, and they are relatively small, as typically observed for these systems.^{29,30} In case of Pn3m phase (23 J/g), ΔH values were sensibly lower than the L (58 J/g) or Ia3d (46 J/g) phases. It is reasonable to hypothesize that the higher the curvature radius and the tortuosity of the aqueous channel network, the lower the strength of the interaction among lipids in the bilayer. As a consequence, despite the Pn3m phase is characterized by a high lipid packing, it features the lowest ΔH value, and the Ia3d phase an intermediate one. Upon adding 20% of VitE to the formulation (H_{II} phase), the peak broadens and the ΔH value becomes similar to that of the Pn3m phase (Table 1). When the percentage of VitE is further increased to 45%, the transition is completely abolished. This is not surprising, given that lipid organization is different in the corresponding micellar phase, leading to very weak interactions among lipid chains due to their low compaction.

DSC measurements on loaded beads were conducted to investigate the effect of the four drugs on lipid bilayer structure and its dependence on their percentage. In the presence of drugs, the shape of the peak in the DSC thermogram remained mostly unchanged, but variations in ΔH values (reported in Table 1) occurred.

Table 1. DSC parameters of MO-B and MO/VitE-B, loaded or not. ΔH values are expressed in J/g, while T_m values are expressed in °C. Error in the case of the obtained temperatures and ΔH are within 0.5 °C and 1.5 J/g, respectively (averaged over three measurements). * Averaged T_m value.

		L		Ia3d		Pn3m		Im3m		H _{II}	
		ΔH	T_m	ΔH	T_m	ΔH	T_m	ΔH	T_m	ΔH	T_m
MO-B		58.	12.8	45.	12.	23.	11.				
		8	*	9	3	0	8				
TOFA	0.1	23.	12.5			38.	12.				
	%	9				9	4				
	1%	49.	12.9			39.	11.				
		7				5	6				
	5%	20.	12.5			36.	11.				
		7				7	4				

BUPI	0.1	50.	12.7			37.	12.
	%	6				6	6
	1%	28.	12.1			38.	11.
		8				9	1
	5%	40.	10.5			36.	11.
		8				8	0
GEFI	0.1	40.	12.2	36.	11.		
	%	6		5	5		
	1%	44.	12.6	24.	11.		
		3		9	0		
	5%	19.	11.2	27.	10.		
		3		5	8		
RAPA	0.1	46.	11.6	39.	12.		
	%	9		4	7		
	1%	41.	12.3	40.	11.		
		6		1	2		
	5%	18.	11.7	33.	11.		
		2		7	6		
MO/Vit						38.	15.
E-B						8	5
TOFA	0.1					5.3	14.
	%						3
	1%					7.0	12.
							8
	5%					/	/

Specifically, when MO-B are in Pn3m phase (the most hydrated one), the ΔH value increases by at least 10 J/g (doubling with 0.1% and 1% of RAPA). The Im3m phase obtained in the presence of BUPI shows comparable results. These findings suggest that the presence of a drug in the most hydrated MO-B structure leads to lipid compaction regardless of their structure and polarity. However, when MO-B are in the L phase, the presence of drugs causes a reduction in ΔH values, which varies depending on their nature and amount. For instance, the presence of 5% of hydrophobic molecules such as RAPA and GEFI results in a three-fold decrease in ΔH values, indicating that these drugs, by penetrating the hydrophobic region of the mesophase in its L geometry, perturbed lipid packing and reduced their compaction. The hydrophilic drug TOFA, when present at 0.1% and 5%, caused a

50% decrease in ΔH values compared to the corresponding MO-B without drugs, whereas at 1% of TOFA the reduction was only 15%. The shape of the thermograms for 0.1% and 5% of the drug is remarkably similar to the split thermogram of empty MO-B. On the other hand, at 1%, the main peak of TOFA is centred at about 13 °C with a shoulder at lower temperatures ($\approx 8^\circ\text{C}$), indicating that this specific ratio induces a change in bilayer organization leading to a noticeable increase in lipid compaction (reflected in higher ΔH and T_m values). In the case of HII beads, TOFA abolished the phase transition even at low ratio, likely because the drug further hindered the weak interactions between lipid chains.

The presence of 0.1% of the other hydrophilic drug BUPI in L phase leads to the same reduction obtained in the presence of TOFA but, in this case, the lowest ΔH value was observed in the beads containing 1% of the drug.

The effect of BUPI on bilayer organization is contingent on its concentration in the beads: at 0.1%, it induces the least significant variations, evidenced by the smallest reduction in ΔH values compared to empty MO-B and beads loaded with the same amount of other drugs. When BUPI concentration reaches 1%, the ΔH value is halved compared to MO-B and is significantly lower than beads containing 1% of other drugs. At 5%, BUPI induces a unique bilayer organization (similar to TOFA): evident phase separation appears in the thermogram, a new main peak emerges at a lower temperature ($\approx 10.5^\circ\text{C}$), and the ΔH value is the highest compared to beads containing 5% of other molecules. It is possible that BUPI's non-crystalline behavior in the beads, unlike the other drugs, contributes to this anomalous behavior.

Overall, these results indicate that hydrophilic drugs interact differently with MO when it is in the L phase, likely because TOFA and BUPI, featuring distinct moieties and polarity, are localized in different portions of the lipid bilayer due to specific interactions between the functional groups of the drugs and the polar head of MO.

8.3 Release profile of drugs and injectability of the beads

Evaluating the release profiles of drugs is crucial to assess the efficacy of the beads as drug delivery platform. As explained, the diffusion coefficient (d) decreases with the dimensionality of the topology, with the cubic phases displaying the highest diffusion coefficients ($d=3$), the L and H_{II} phases showing an intermediate one ($d=2$ and $d=1$, respectively) and the inverse micellar cubic phases showing the lowest ($d=0$).²³

Immediately after the preparation of the beads, they were submerged in an excess of media and the release profiles of the four drugs were determined starting from the less hydrated beads (since rheology proved that they could be easily injected with respect to more hydrated phases) which intake water during the experiment. TOFA was quickly released (more than 85% after 7 h) in physiological conditions (PBS buffer, 150 mM, pH 7.4, Figure 10A). Therefore, to decrease the drug release rate, thus achieving a sustained release, we loaded TOFA in H_{II} beads, since this mesophase is characterized by a lower d with respect to Pn3m phase. In this case, as assumed, the percentage of drug release decreased: after an initial burst, 85% of release was achieved after six days instead of a few hours (Figure 10) despite a loss in regeneration was observed (see Figure 7). Thus, although these beads do not maintain their structural integrity, they ensure a consistent and predictable drug release profile.

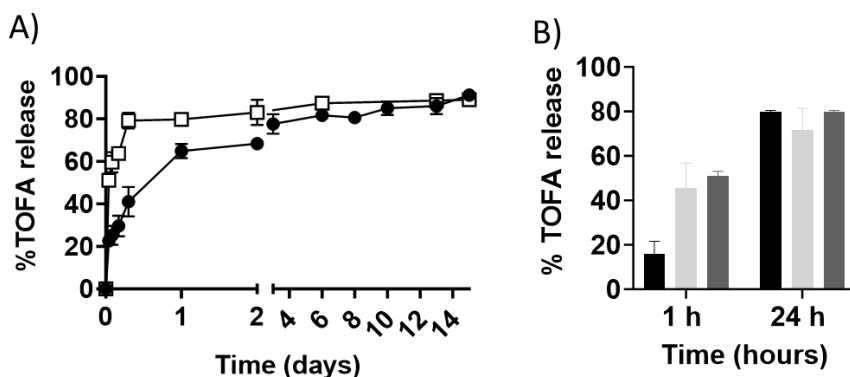


Figure 10. A) TOFA release profile from MO-B (white squares) and MO/VitE-B (black dots). B) Comparison of TOFA release from beads after preparation (black bars), after injection (light grey bars) and in their Pn3m phase (dark grey bars).

The injectability of the proposed MO-B was tested using a syringe and an 18G needle, both in aqueous solution and in an agarose gel system that mimic a subcutaneous injection:³¹ in both cases, they were extruded (Figure 11).

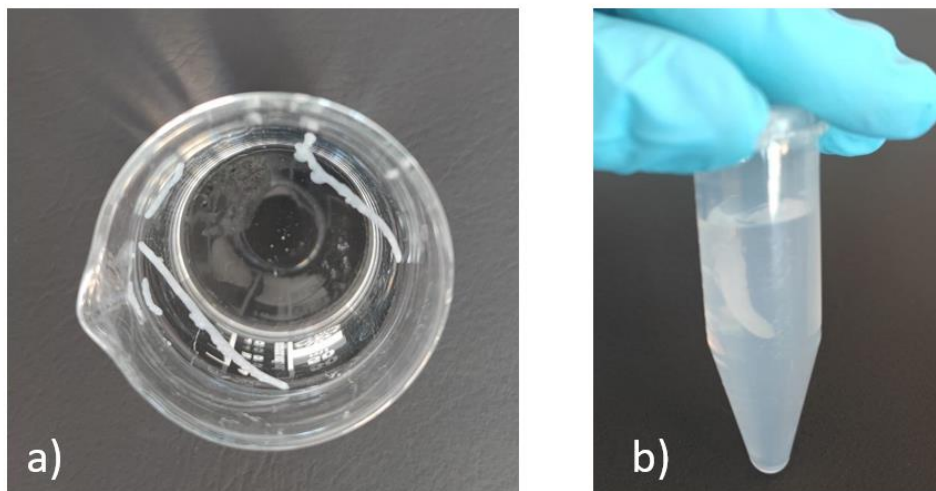


Figure 11. MO-B after injection in a) water and b) agarose gel using a syringe with a 18G needle.

In particular, we analysed MO-B soon after their injection in aqueous solution with SAXS, and it revealed that L phase changed to a la3d one. In order to study if this

phase changing could cause any variations in the release profile of a molecule, we tested it using TOFA as model drug. The release profile of TOFA from extruded beads (Ia3d phase, light grey bars in Figure 10B) after one h is quite different from the one obtained with beads soon after their preparation (L phase, black bars in Figure 10B). After one day, instead, the release profiles were similar. This result is not surprising since L phase display a lower d with respect to cubic phases. To prove this hypothesis, we investigated TOFA release from beads that remained 24 h in an aqueous solution saturated with the drug, which have a Pn3m symmetry (dark grey bars in Figure 10B). TOFA release from Pn3m beads after 1 h and 1 day is quite similar to the release from Ia3d beads, meaning that the extrusion process could have influenced the release profile of TOFA in the first hours.

The release profile of GEFI was also assessed, both in physiological conditions and in a simulated intraperitoneal fluid (20% of DMSO was added to bypass drug solubility limit). In the first case, GEFI was not released from the beads, even after 15 days, while in simulated intraperitoneal environment the percentage of drug released reached the 20% (Figure 11A). Both buffers enriched with DMSO did not affect the mesophase of the beads (Pn3m), as pointed out by SAXS experiments, but the presence of glucose in simulated fluid (SF) leads to 5 nm water channel. Sugar esters are usually added to lipids to enlarge water channels; probably glucose was incorporated into the beads during the swelling process and interacted with the polar heads of MO with consequent formation of expanded water channels. GEFI is a small molecule so it should pass through channels of 3 nm and should not need extended ones, but it is reasonable to think that their enlargement encourages its release because of the highest amount of water in the channels. MO exhibits partial solubility in DMSO, so the drug release can be influenced by both diffusion and erosion mechanisms. Hence, we assessed the percentage of erosion of the beads in the buffer enriched with the organic solvent during time

and it's lower than 5%: that means that GEFI release is mostly driven by diffusion processes and not by the erosion of the system (Figure 11A).

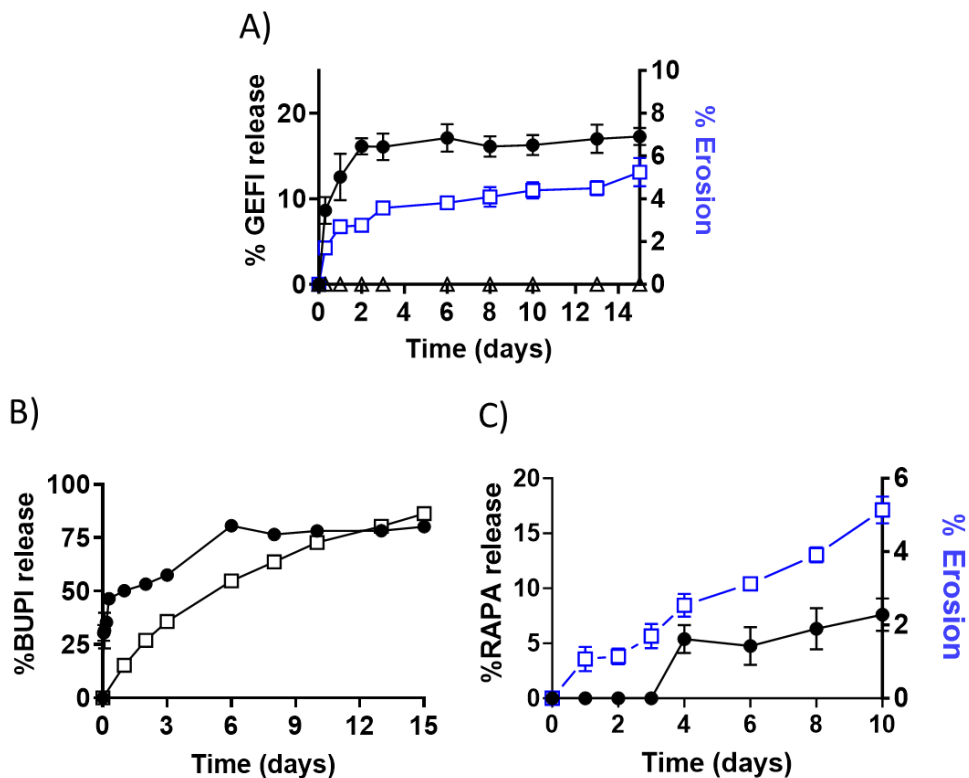


Figure 12. A) Release profile of GEFI in physiological conditions (white triangles), in SF (black dots) together with the erosion of the beads in the SF (squares; right axis). B) Release profile of BUPI in physiological conditions (black dots) and from agarose gel (white squares), e) release profile of RAPA in H₂O/EtOH 9/1 (black dots) together with the erosion of the beads in the same media (squares; right axis).

Despite the Im3m phase had a $d=3$ and BUPI was well soluble in water, its release profile in physiological conditions was sensitively slower than TOFA's (Figure 11B). Likely, non-covalent interactions between the drug and MO were established, as supported by the formation of an Im3m phase instead of a Pn3m one, reducing its ability to leave the aqueous channels. The release profile of BUPI was also assessed an agarose gel-based system, that mimics the subcutaneous environment³¹ where BUPI-loaded beads should be administered, limiting unnecessary animal

experimentation in the first stages of a study. Figure 11B points out the sustained and controlled release of BUPI over time in subcutaneous environment, indicating the good potentiality of the proposed delivery system.

On the other hand, RAPA release in physiological conditions (enriched with 10% of EtOH for solubility reasons) was mostly driven by erosion (Figure 11C): in this case release and erosion profiles were very similar and they reached about 15% release in 15 days. The presence of EtOH had no impact on the topology of the beads and they continued to maintain their Pn3m phase, while the presence of lipase (that mimic inflammation) in SF led to a H_{II} topology, as revealed by SAXS experiments. Moreover, macroscopically, RAPA-loaded beads had completely eroded after 8 h in SF, reasonably because lipases hydrolysed the ester bond of MO. Lipase, in fact, is an enzyme that catalyses the hydrolysis of triacylglycerols by breaking the ester bonds between the glycerol and the fatty acid molecules.³² The degradation of glyceryl monooleate, a LMPs precursor with a structural resemblance to MO, induced by lipase has previously been reported.³³

The release profile of RAPA in SF was evaluated using a vertical diffusion cell. We expected to achieve a complete release of the drug after 8 h since we observed the disruption of the beads, but no RAPA was detected in the acceptor compartment of the diffusion cells. To ensure that lipases did not degrade RAPA, obstructing its visibility in the HPLC chromatograms, we checked the stability of the drug in the presence of the enzyme over time. The UV-Vis spectra revealed a 5 nm redshift within one day, observed at both room temperature and 37 °C. Notably, this redshift persisted even in the absence of lipases, ruling out the enzyme as the cause. It is likely that the hydrophobic RAPA experienced aggregation or formed complexes with other molecules in a such polar environment (H₂O/EtOH 9/1), inducing alterations in the electronic structure and consequential spectral shifts. Over the course of two weeks, no changes were discerned, indicating that RAPA retained stability in the solution in the presence of the enzyme.

We also examined the ability of free RAPA to cross the membrane from the donor compartment to the acceptor compartment: after 24 h, nearly all the drug ($\approx 78\%$) was found in the acceptor compartment, meaning that no interactions with the membrane or the diffusion cell hindered the drug from being detected in the acceptor compartment. To further investigate, we analysed the content of the donor compartment tracking the species dissolved into the SF and, surprisingly, we discovered a predominant population of aggregates of 150 nm in diameter after one hour. Within one day, this population became heterogeneous, ranging from 150 to 400 nm in diameter. As shown in Figure 13A, the higher the erosion of the beads during time, the greater the number of aggregates they formed. These vesicles were probably composed of de-esterified MO that rearranged itself into spherical vesicles, encapsulating the hydrophobic RAPA.

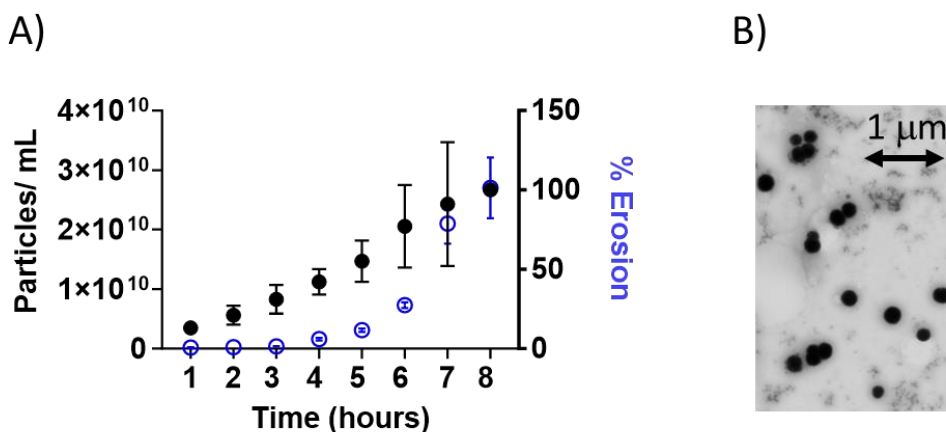


Figure 13. A) Erosion of RAPA-loaded beads in SF (blue frame circles; left axis) and formation of de-esterified MO aggregates (black circles; right axis) during time. B) STEM images of aggregates composed of de-esterified MO.

STEM images of the aggregates found in the donor compartment after 8 h are reported in 13B. Despite the complete erosion of the beads, the aggregates they form act as a sustained DDSs. We monitored the vesicle size in SF for two weeks, observing gradual aggregation that led to the formation of different populations

with sizes ranging from 150 to 900 nm. The aggregation was also confirmed by assessing the vesicle concentration in the dispersion, revealing a gradual decrease in the number of particles per millilitres over time within 10 days. After this time, the concentration remained stable, as the distribution of the vesicles.

8.4 Conclusion

In this investigation we reported, for the first time, the preparation of LMPs-based beads as a new platform for the local and sustained release of drugs. Ranging from hydrophilic to hydrophobic compounds, we demonstrated that excellent loading efficiency can be obtained, and that a sustained release profile for the four distinct drugs we tested could be achieved. Following comprehensive physicochemical characterization, we showed that, despite the complete erosion of the beads in the presence of lipase - typically present in cells and tissues of patients with inflammatory diseases - the degradation product of MO can reorganize and create spherical aggregates that continue to function as DDS.

Our LMP-based beads hold great promises as an injectable DDS and, by means of future in vivo studies, we plan to fully harness their therapeutic potential.

8.5 Bibliography

1. Carone, M. *et al.* Temperature-triggered in situ forming lipid mesophase gel for local treatment of ulcerative colitis. *Nat Commun* **14**, (2023).
2. Martiel, I. *et al.* Oil and drug control the release rate from lyotropic liquid crystals. *Journal of Controlled Release* **204**, 78–84 (2015).
3. Sagalowicz, L. *et al.* Influence of vitamin e acetate and other lipids on the phase behavior of mesophases based on unsaturated monoglycerides. *Langmuir* **29**, 8222–8232 (2013).
4. Mezzenga, R. *et al.* Shear rheology of lyotropic liquid crystals: A case study. *Langmuir* **21**, 3322–3333 (2005).
5. Dong, Y. Da, Larson, I., Hanley, T. & Boyd, B. J. Bulk and dispersed aqueous phase behavior of phytantriol: Effect of vitamin E acetate and F127 polymer on liquid crystal nanostructure. *Langmuir* **22**, 9512–9518 (2006).
6. Bitan-Cherbakovsky, L., Yuli-Amar, I., Aserin, A. & Garti, N. Structural Rearrangements and Interaction within H(II) Mesophase Induced by Cosolubilization of Vitamin E and Ascorbic Acid. *Langmuir* **25**, 13106–13113 (2009).
7. Montalvo, G., Valiente, M. & Rodenas, E. Rheological properties of the L phase and the hexagonal, lamellar, and cubic liquid crystals of the CTAB/benzyl alcohol/water system. *Langmuir* **12**, 5202–5208 (1996).
8. Bandarra, N. M., Campos, R. M., Batista, I., Nunes, M. L. & Empis, J. M. Antioxidant synergy of α -tocopherol and phospholipids. *JAOCS, Journal of the American Oil Chemists' Society* **76**, 905–913 (1999).
9. Clogston, J. & Caffrey, M. Controlling release from the lipidic cubic phase. Amino acids, peptides, proteins and nucleic acids. *Journal of Controlled Release* **107**, 97–111 (2005).
10. Zhao, J., Guo, B. & Ma, P. X. Injectable alginate microsphere/PLGA-PEG-PLGA composite hydrogels for sustained drug release. *RSC Adv* **4**, 17736–17742 (2014).
11. Huang, Y. & Gui, S. Factors affecting the structure of lyotropic liquid crystals and the correlation between structure and drug diffusion. *RSC Advances* vol. 8 6978–6987 Preprint at <https://doi.org/10.1039/c7ra12008g> (2018).

12. Cohen, R., Kanaan, H., Grant, G. J. & Barenholz, Y. Prolonged analgesia from Bupisome and Bupigel formulations: From design and fabrication to improved stability. *Journal of Controlled Release* **160**, 346–352 (2012).
13. Disease, I. B. ADVANCES IN IBD Update on Tofacitinib for Inflammatory Bowel Disease. *Gastroenterol Hepatol (N Y)* **12**, 572–574 (2016).
14. Molander, V. *et al.* Venous thromboembolism with JAK inhibitors and other immune-modulatory drugs: A Swedish comparative safety study among patients with rheumatoid arthritis. *Ann Rheum Dis* **82**, 189–197 (2022).
15. Migita, K. *et al.* The effects of the immunosuppressant rapamycin on the growth of rheumatoid arthritis (RA) synovial fibroblast. *Clin Exp Immunol* **104**, 86–91 (1996).
16. Perl, A. Activation of mTOR (mechanistic target of rapamycin) in rheumatic diseases. *Nat Rev Rheumatol* **12**, 169–182 (2016).
17. Bordon, G., Berenbaum, F., Distler, O. & Luciani, P. Harnessing the multifunctionality of lipid-based drug delivery systems for the local treatment of osteoarthritis. *Biomedicine and Pharmacotherapy* **168**, 115819 (2023).
18. Cersosimo, R. J. Gefitinib: An adverse effects profile. *Expert Opin Drug Saf* **5**, 469–479 (2006).
19. Cho, C. D., Fisher, G. A., Halsey, J. & Sikic, B. I. Phase I study of gefitinib, oxaliplatin, 5-fluorouracil, and leucovorin (IFOX) in patients with advanced solid malignancies. *Invest New Drugs* **24**, 117–123 (2006).
20. Moore, P. A. Bupivacaine: A long-lasting local anesthetic for dentistry. *Oral Surgery, Oral Medicine, Oral Pathology* **58**, 369–374 (1984).
21. Paganelli, M. A. & Popescu, G. K. Actions of bupivacaine, a widely used local anesthetic, on NMDA receptor responses. *Journal of Neuroscience* **35**, 831–842 (2015).
22. Aleandri, S. *et al.* Development and in vivo validation of phospholipid-based depots for the sustained release of bupivacaine. *European Journal of Pharmaceutics and Biopharmaceutics* **181**, 300–309 (2022).
23. Aleandri, S. & Mezzenga, R. The physics of lipidic mesophase delivery systems. *Phys Today* **73**, 38–44 (2020).

24. Bitan-Cherbakovsky, L., Yuli-Amar, I., Aserin, A. & Garti, N. Solubilization of vitamin e into HII LLC mesophase in the presence and in the absence of vitamin C. *Langmuir* **26**, 3648–3653 (2010).
25. Sagalowicz, L. *et al.* Influence of vitamin e acetate and other lipids on the phase behavior of mesophases based on unsaturated monoglycerides. *Langmuir* **29**, 8222–8232 (2013).
26. Kulkarni, C. V., Wachter, W., Iglesias-Salto, G., Engelskirchen, S. & Ahualli, S. Monoolein: A magic lipid? *Physical Chemistry Chemical Physics* **13**, 3004–3021 (2011).
27. Kumar, M. & Kumaraswamy, G. Phase behaviour of the ternary system: Monoolein-water-branched polyethylenimine. *Soft Matter* **11**, 5705–5711 (2015).
28. Angelova, A. *et al.* Advances in structural design of lipid-based nanoparticle carriers for delivery of macromolecular drugs, phytochemicals and anti-tumor agents. *Adv Colloid Interface Sci* **249**, 331–345 (2017).
29. Qiu, H. & Caffrey, M. The phase diagram of the monoolein/water system: Metastability and equilibrium aspects. *Biomaterials* **21**, 223–234 (2000).
30. Reese, C. W., Strango, Z. I., Dell, Z. R., Tristram-Nagle, S. & Harper, P. E. Structural insights into the cubic-hexagonal phase transition kinetics of monoolein modulated by sucrose solutions. *Physical Chemistry Chemical Physics* **17**, 9194–9204 (2015).
31. Bassand, C., Verin, J., Lamatsch, M., Siepmann, F. & Siepmann, J. How agarose gels surrounding PLGA implants limit swelling and slow down drug release. *Journal of Controlled Release* **343**, 255–266 (2022).
32. Hou, C. T. & Shimada, Y. Lipases. *Encyclopedia of Microbiology, Third Edition* 385–392 (2009) doi:10.1016/B978-012373944-5.00153-X.
33. Mei, L. *et al.* Self-assembled lyotropic liquid crystal gel for osteoarthritis treatment: Via anti-inflammation and cartilage protection. *Biomater Sci* **9**, 7205–7218 (2021).

Chapter 9: Magnetoliposomes for Water Remediation

9. Magnetoliposomes against APEOs: a promising solution for tackling water pollution from textile industries

The fundamental need for access to clean water underscores the importance of prioritizing research on contaminant removal from aquatic systems. This emphasis is essential not only to restore the balance within ecosystems but also to ensure a more sustainable future. Given the indispensable role that water plays in supporting life, understanding and addressing the challenges related to water contamination become imperative for safeguarding environmental health and fostering long-term viability. Various technologies for water remediation are currently available, encompassing precipitation, membrane technology, coagulation/flocculation, biological processes, and advanced oxidation processes.¹⁻

³ Each method presents its own set of advantages and drawbacks: chemical precipitation proves cost-effective, although it generates sludge and is sensitive to pH;⁴ membrane technology is adaptable for various pollutants, but comes with high energy consumption and is susceptible to membrane fouling;⁵ coagulation/flocculation effectively removes suspended solids, yet necessitates additional chemicals and results in sludge generation;⁶ biological processes are considered environmentally friendly and cost-effective, but exhibit a lengthy treatment time;⁷ oxidation processes demonstrate effectiveness against refractory pollutants, yet demand high energy consumption and lead to the production of toxic by-products;⁸ adsorption is highly versatile, but encounters challenges related to saturation and regeneration.^{9,10} Briefly, they encounter challenges such as high operating costs, the generation of secondary pollutants, and, notably, an inability to entirely eliminate the contamination in wastewater. The use of porous materials for the adsorption of pollutants presents a viable alternative for efficiently

eliminating contaminants from water ecosystems. Mesoporous clay materials, zeolites, bio adsorbents, and polymeric resins have shown promising performances to some degree against various contaminants found in aqueous media.¹¹ Nevertheless, their primary limitation lies in the absence of synthetic methods that would empower materials scientists to precisely customize their structures and pores, on their high production costs, and on their difficult scalability.^{11,12} Achieving precise control over adsorption kinetics, capacity, and selectivity for pollutants becomes challenging, but it is crucial for enhancing the performance of adsorbents and implementing effective water reclamation protocols. Thus, the need to find an alternative approach that is versatile, cost-effective, recyclable, ensures prompt pollutant removal, and avoids secondary pollution is crucial.

Magnetic core-shell liposomes (MLs) are an interesting type of nanocomposite that combines liposomes with magnetic nanoparticles (MNPs). To obtain this kind of system, MNPs could be covered with a lipid bilayer (solid MLs), entrapped in the aqueous core of liposomes as suspension (aqueous MLs) or they could be non-covalently functionalized with a lipophilic coating in order to be embedded in the lipid bilayer of common liposomes.¹³ Despite the growing interest in MLs in the biomedical field (such as contrast agents for imaging,^{14,15} in targeted drug delivery,¹⁶⁻¹⁸ and for hyperthermia therapy¹⁹⁻²¹), their potential in water remediation, as well as the role of lipid components in determining their effectiveness, at the best of our knowledge, has not been explored yet.

In this study, for the first time, MLs composed of superparamagnetic iron oxide nanoparticles (SPIONs) enclosed within a lipid bilayer were employed as a tool to remove a common class of organic pollutants, alkylphenol ethoxylates (APEOs), from water. Once pollutants partition in the lipid phase of MLs, and thus in the designed system, MLs and APEOs can be easily removed from the aqueous environment using a magnet. Here, APEOs are employed as a proof of concept for common organic pollutants to assess the validity of the proposed approach as a

broad and general strategy for water remediation. APEOs are low-cost surfactants largely employed as industrial process aids and in cleaning formulations,²² and are commonly discharged into municipal and industrial wastewaters. APEOs, along with their persistent, bio accumulative, and harmful degradation products such as octylphenol and nonylphenol (OP and NP, respectively, Scheme 1), have sparked considerable environmental and health concerns. These substances, in fact, are classified as endocrine-disrupting chemicals^{23,24} and are found in elevated concentrations in the food chain.²⁵ The European Union's REACH regulation (Registration, Evaluation, Authorization, and Restriction of Chemicals) restricts the use of OPEO and NPEO as they are classified as substances of very high concern and are included in the candidate list for authorization. According to REACH, as of February 2021, textile articles containing more than 100 ppm of APEOs shall not be placed on the market. Unfortunately, APEOs are extensively used in the rest of the world, and REACH regulations do not apply to the placement of second-hand textile and recycled articles on the market.

For the preparation of the examined MLs, which exhibit a lipid bilayer with varying charge and/or organization, we used a primary component comprising a mixture of phospholipids with different chain lengths and degrees of unsaturation extracted from soybeans (SPC, Scheme 1), in the absence or in the presence of different

surfactants (the cationic dihexadecyldimethylammonium bromide, DHDAB, or the anionic stearic acid, SA, Scheme 1).

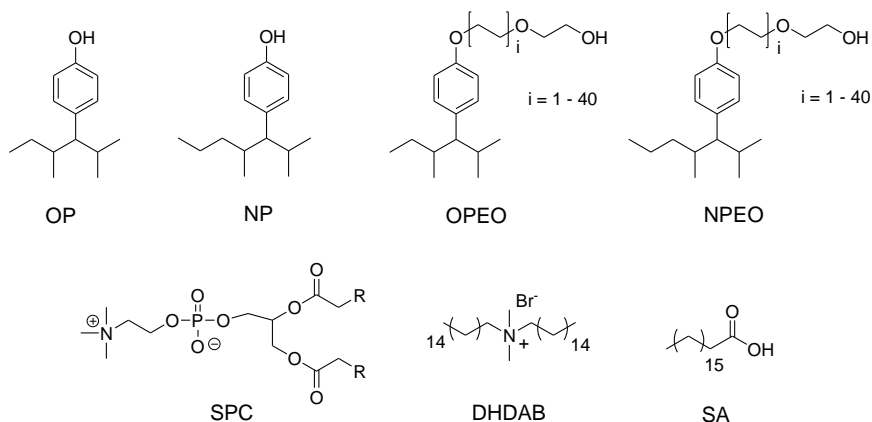


Chart 1. Structures of pollutants and lipids.

SPIONs were prepared following two synthetic routes, as well as MLs, to examine how the used procedure could affect MLs properties and, as a consequence, their ability to remove APEOs. To better understand the interaction mechanisms between our SPIONs and the different lipid polar-heads, theoretical calculations based on molecular dynamics (MD) simulations were performed.

Both SPIONs and MLs were characterized using a full set of different techniques: ATR-FTIR and fluorescence spectroscopy, scanning transmission electron microscopy (STEM), XRD, XPS, N_2 absorption studies (BET surface area), thermogravimetric (TGA) and AGFM analysis. Their ability to entrap and remove NPEO and OPEO (Chart 1) from standard solutions was assessed, as well as the recyclability of the system.

The key element of this investigation is the systematic and reasoned variation of SPIONs and MLs preparation, and MLs composition to evaluate their effect on their physicochemical properties and on their effectiveness in APEOs removal. The final aim of this research is to determine which parameters are crucial for the interaction

of MLs with the pollutants to modify their composition in a controlled manner and optimize their efficacy in the treatment of industrial wastewater.

9.1 SPIONs Synthesis and Characterization

SPIONs were prepared following two different synthetic routes based on co-precipitation (SR1 and SR2) reported in literature.^{26,27} In both cases, two fine dark powders were obtained. A complete analysis of their physical and magnetic properties was performed using a full set of characterization techniques. ATR-FTIR spectroscopy confirmed the formation of Fe-O bond (551 cm^{-1} , Figure 1) and XRD (Figure 2) revealed a composition of approximately 20% maghemite ($\gamma\text{-Fe}_2\text{O}_3$) and 80% magnetite (Fe_3O_4) in samples prepared according to SR1. However, the observed ratio maghemite/magnetite is not always reproducible. On the contrary, all SR2 samples showed the typical pattern of magnetite.

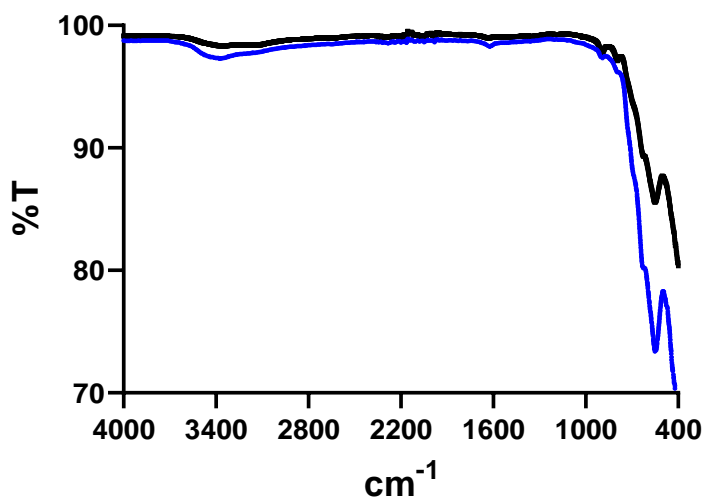


Figure 1. SPIONs characterization by ATR-FTIR. Blue lines refers to SR1, while black line refers to SR2.

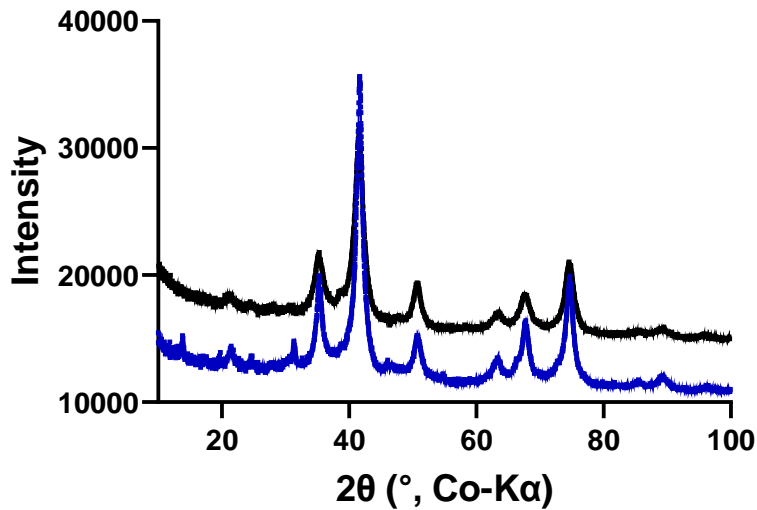


Figure 2. SPIONs characterization by XRD. Blue lines refers to SR1, while black line refers to SR2.

This outcome can be explained a controlled generation of iron oxyhydroxides, leading to high reproducibility and the absence of maghemite. The discrimination of the two magnetic iron oxides using by considering that the nucleation and growth of SPIONs are significantly influenced by the pH of the reaction environment: the formation of these nanoparticles arises from the conversion of iron oxy-hydroxides and hydroxides, which readily undergo oxidation when exposed to air, rather than from the direct reaction of Fe^{2+} and Fe^{3+} salts.²⁸ pH and O_2 significantly influence the structural features of the end product, as these intermediates may continue to exist within it.^{29–32} In the SR2 procedure, the initial pH is acidic (which prevents the formation of iron hydroxides) and then it is gradually adjusted to alkaline levels. Differently, in the SR1 method, ammonia is introduced after the solubilization of the iron salts, which occur at neutral pH. This distinction results in XRD could be tough since they share the same spinel crystal structure (they differ for the distribution of the iron ions: in maghemite, they occupy the octahedral sites of the lattice, while in magnetite they occupy both

tetrahedral and octahedral sites).³³ A fitting program was used to match the obtained diffractograms with reference structures.

XPS, a powerful technique that can discriminate between different oxidation states of metals,³⁴ was employed to confirm XRD results. For SR1, the presence of two peaks centered at 710.9 and 724.7 eV is evident, aligning well with reported shifts for maghemite or hematite. This is further supported by the confirmation of satellite peaks at 719.3 and 733.5, corresponding to Fe2p_{3/2} and Fe2p_{1/2}. It is noteworthy that these peaks can sometimes be influenced by the measurement, leading to transitions between magnetite and maghemite due to the impact of energetic electrons, causing localized alterations in composition.³⁵ In contrast, for SR2, only the primary peaks related to spin-orbit coupling are observed, with the absence of any satellite peaks, suggesting that the composition is predominantly magnetite, a finding consistent with results from XRD and other techniques.³⁵

AGFM also confirms the different composition of SR1 and SR2: the second shows a higher magnetization compared to the first one, as expected (Figure 3). Magnetite, in fact, is generally more magnetic than maghemite³⁶ and is considered one of the most magnetic minerals naturally occurring.³⁷ Considering that SR1 consists of ≈20% of maghemite, it was anticipated that its magnetization would be comparatively reduced. In any case, the lack of, or extremely reduced, hysteresis supported the confirmation of superparamagnetic. Examination of the magnetization curves also unveiled the presence of nanoparticles with an average diameter of 8.5 nm for SR1 and about 9.5 nm for SR2.

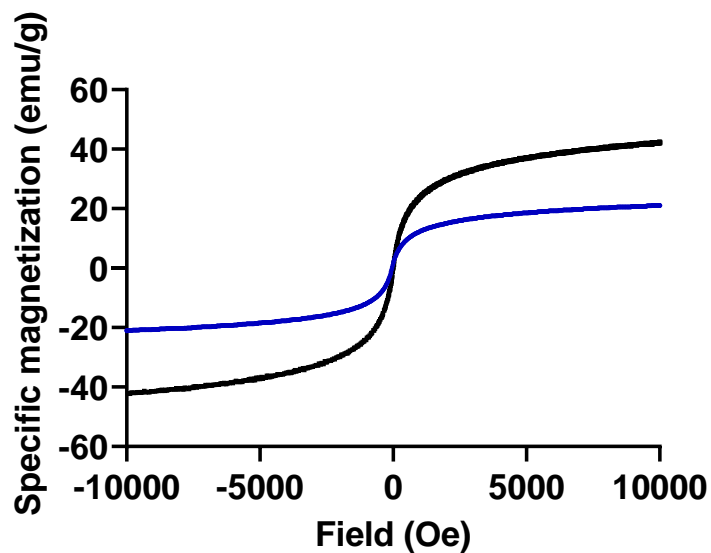


Figure 3. SPIONs characterization by AGFM. Blue line refers to SR1, while black line refers to SR2.

The size and morphology of both samples were further explored using electron microscopy techniques: STEM observations indicated a notable uniformity in the samples, with an average diameter of about 8 nm for both SR1 and SR2. In Figure 4, an image of SR2 is reported as example.

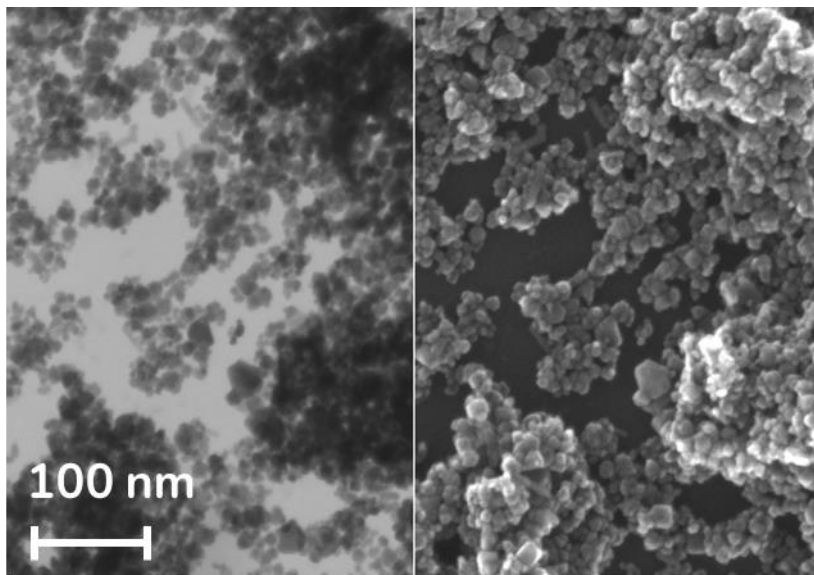


Figure 4. STEM measurement of SR2, reported as example.

These findings align well with the results obtained from the analysis of magnetization curves. No significant differences in morphology and dimensions were found, meaning that these parameters are not affected by the preparation technique.

9.2 MLs Preparation and Characterization

Once obtained the magnetic core, SPIONs were covered with a lipid bilayer adapting two procedures found in literature.^{38,39} In thin film hydration (TFH) method, MLs could be prepared in one step as a result of hydrophobic interactions established between lipids and water in presence of SPIONs. In solvent injection (SI) process, two different steps are required: in the first one, performed in chloroform, interactions between the magnetic core and the polar head of lipids are established and the first layer is obtained. In the following step, performed in water after the removal of chloroform, the second layer is attached to the first (due to hydrophobic interactions between lipids and the solvent) to form the lipid bilayer.

For the first test, MLs composed of SPC (a mixture of unsaturated phospholipids extracted from soybean) were prepared following both methodologies and employing both SR1 and SR2. The easiest and most rapid technique to verify the formation of the lipid bilayer upon SPIONs was ATR-FTIR: in the obtained spectra, all the characteristic signals of phospholipids were visible (peaks at 2940 cm^{-1} and 2850 cm^{-1} are attributed to symmetric and asymmetric methylene and methyl vibrations, peaks at 1245 cm^{-1} and 1070 cm^{-1} are attributed to PO_2^- headgroup vibrations, while peaks at 1740 cm^{-1} and 970 cm^{-1} are attributed to carbonyl vibrations and quaternary ammonium asymmetric vibration, respectively), in addition to the one related to the Fe-O bond (Figure 5), indicating that SPC was successfully attached to the magnetic core.

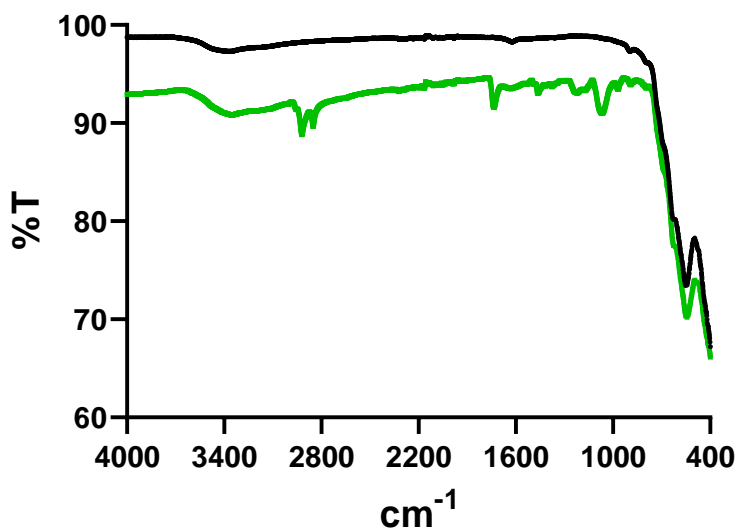


Figure 5. ATR-FTIR spectra of SR2 (black line) and MLs composed of SPC prepared by TFH technique (green line, reported as an example).

During the initial phase of characterization, no distinctions were observed among the four distinct samples. However, we decided to exclusively employ SR2 as magnetic core considering that SR2 (pure magnetite) exhibits superior magnetization and reproducibility in comparison to SR1, which could offer

substantial advantages in industrial applications. We also attempted to synthesize MLs using commercially available magnetite nanoparticles (50-100 nm), but we were unable to achieve the desired product, as confirmed by the absence of phospholipid signals in IR spectra. Probably, the big dimensions of nanoparticles (and thus a reduced surface area) hampered their coating.

While we successfully obtained MLs containing SPC through both TFH and SI approaches, the scenario changed when our focus shifted to producing charged formulations involving cationic and anionic lipids and using SR2 as magnetic core. The attempts to produce cationic MLs composed of DHDAB were unsuccessful using both the TFH and SI methods (as indicated by the lack of lipid signals in the IR spectra), while they were both effective in producing anionic MLs composed of SA. Our hypothesis is that magnetite exhibits minimal interaction with the ammonium head of DHDAB, whereas it demonstrates a strong affinity for the carbonyl group of SA. The situation diverged also when attempting to prepare mixed cationic and anionic formulations, using SPC and 50% of DHDAB or SA. Mixed cationic MLs were exclusively obtained using the solvent injection technique, probably because in the presence of chloroform the interaction between Fe_3O_4 and DHDAB and SPC (in the first step of the procedure) is stronger than in water and reasonably the first lipid layer is composed predominantly of SPC. On the other hand, mixed anionic MLs were successfully prepared through both methods without any complications.

Another interesting result is that we expected the formation of asymmetric bilayer through the solvent injection approach, using SPC in the initial step and DHDAB or SA in the subsequent step. This outcome was observed for asymmetric cationic MLs, but not for the asymmetric anionic counterparts. In the latter case, the IR spectra indicated the presence of carbonyl vibration (1740 cm^{-1}), but the signals associated with the phosphate headgroup (expected at 1070 and 1245 cm^{-1}) were absent. Consequently, we conducted two distinct IR spectra, one following each step of the process, to clarify this result. We observed the phosphate signals, after

the initial step (involving SPC), whereas only the carbonyl-associated signal was evident after the subsequent step (involving SA). Our results demonstrated that the strong interactions between magnetite and SA were able to undermine the first layer of SPC.

STEM and fluorescence microscopy analyses were performed on representative samples to confirm MLs formation. From STEM observation it is possible to notice a coating layer on the magnetic core (Figure 6B). Furthermore, we estimated an average diameter of 10 nm. To prove that the coating layer consisted of a lipid bilayer, some initial fluorescence microscopy experiments were conducted on ML prepared using the SI technique. A lipophilic fluorescent dye (1,1'-dioctadecyl-3,3,3',3'-tetramethylindocarbocyanine perchlorate, DiI) was included in the bilayer. In these tests, we introduced DiI during the first step of the procedure, enabling observation of fluorescence emission and thus the formation of a layer. Subsequently, in another experiment, DiI was added only during the second step of the procedure (required for obtaining the second layer), resulting in observed fluorescence emission. In conventional liposomes (comprising an aqueous core enveloped by a lipid bilayer), flip-flop movements (lipids exchanging between layers) are rare (approximately 1 occurrence per month), thus it is reasonable to believe that the formation of the lipid bilayer occurred. In the case of samples prepared using the TFH methodology, it wasn't possible to create one layer at a time, as TFH is a one-step process. Anyway, the exposure of these samples to a FITC filter for fluorescence spectroscopy (excitation/emission wavelength respectively at 467-498 nm / 513-556 nm) always resulted in fluorescence emission (Figure 6A),

confirming the presence of fluorescent lipids and consequently the coating of SPIONs.

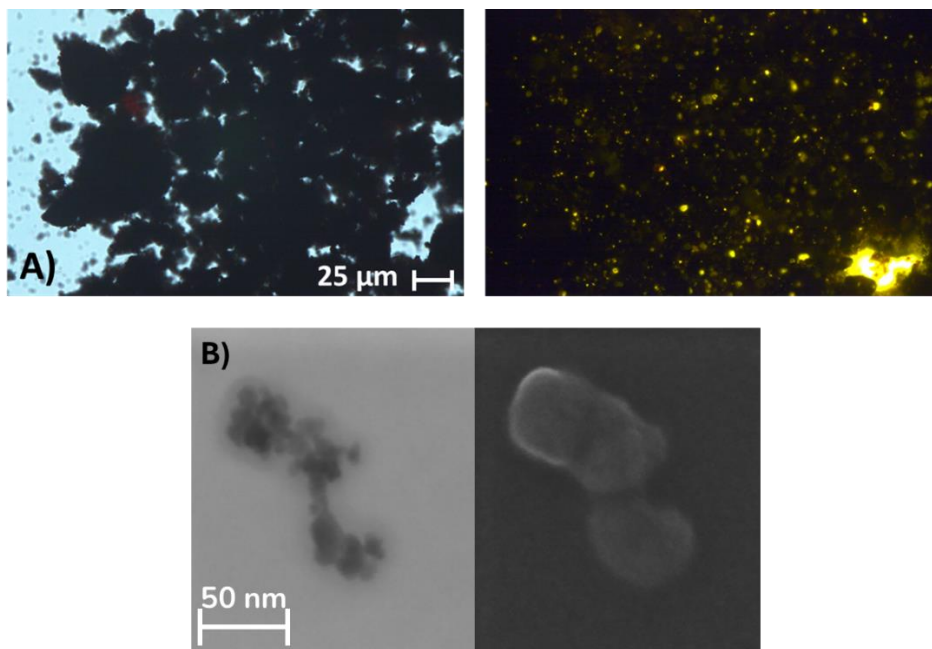


Figure 6. MLs characterization by A) fluorescence microscopy and B) STEM. In Figure 6A, bright field image (on the left) and fluorescent image (on the right) of ML composed of SPC (prepared by TFH) are reported as an example. In Figure 6A, the morphology of ML composed of SPC (prepared by TFH) is reported as an example.

XRD analyses were conducted on all MLs formulations, revealing no discernible distinction between the diffractograms of SR2 and the MLs (Figure 2C); this evidence suggests that the crystal phase of magnetite remained unaffected during the coating process, as expected.

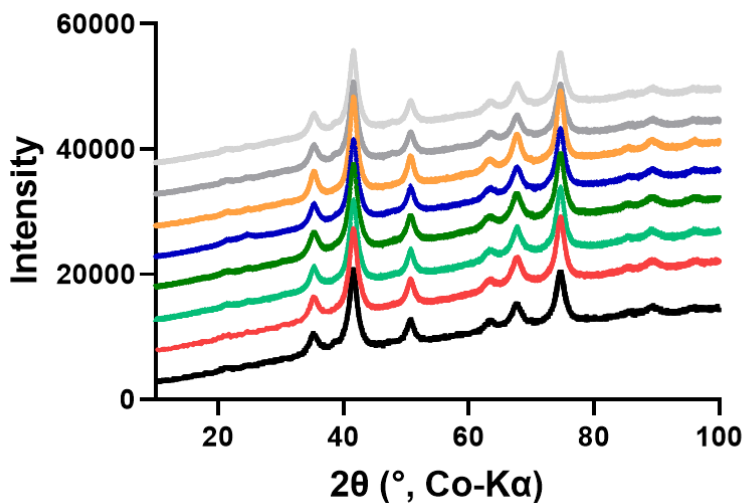


Figure 7. MLs characterization by XRD. From top to bottom: neutral ML (TFH), neutral ML (SI), mixed cationic ML, asymmetric cationic ML, mixed anionic ML (TFH), mixed anionic ML (SI), anionic ML (TFH), anionic ML (SI), SR2.

MLs are also superparamagnetic, as pointed out by AGFM, and as expected, the coating process did not particularly affect the specific magnetization of the SPIONs (Figure 8). That means that MLs possess significant magnetic properties due to their magnetic core which are enough to enable their separation from solutions through the application of an external magnetic field. Analysis of the curves revealed that MLs have diameters between 9.2 and 9.7 nm, in good agreement with STEM results.

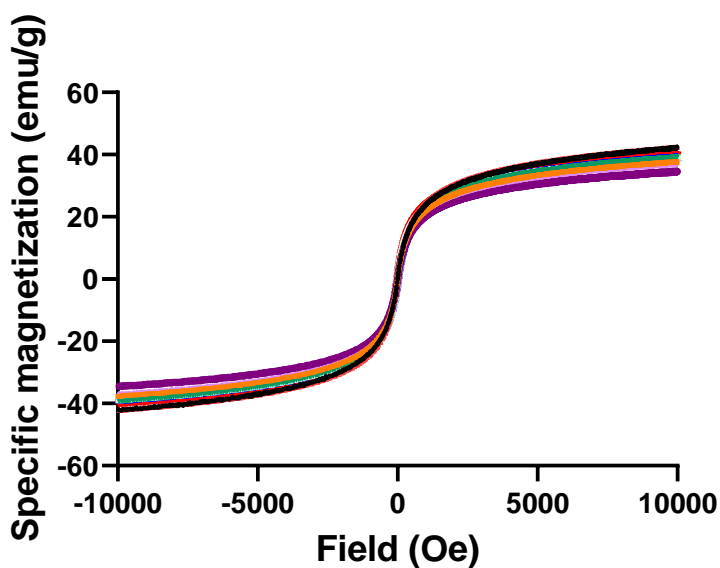


Figure 8. MLs characterization by AGFM. From top to bottom: SR2, neutral ML (TFH), neutral ML (SI), anionic ML (SI), mixed anionic ML (TFH), anionic ML (TFH), mixed cationic ML, mixed anionic ML (SI), asymmetric cationic ML.

The surface area of all the set of samples was determined via N₂ adsorption experiments. This technique is particularly valuable in characterizing materials such as catalysts, adsorbents, and nanoparticles where the surface area plays a crucial role in their performance. Our results reveal that neutral, mixed cationic and asymmetric cationic MLs have a surface area of ≈ 120 m²/g. In case of mixed anionic and anionic formulations, the surface area diminished to lower values (40 – 80 m²/g). The decrease of BET area with respect to the one of SPIONs (135 m²/g, result perfectly in line with others for similar systems)^{40–42} is due to the increasing coverage of the magnetic core by the lipid bilayer, which prevents the entry of nitrogen probe molecules.^{26,43} In Figure 9, a desorption-absorption graph of SR2 is reported as example. This hypothesis is supported by the strong interaction between SA and magnetite, that resulted evident in anionic MLs formation.

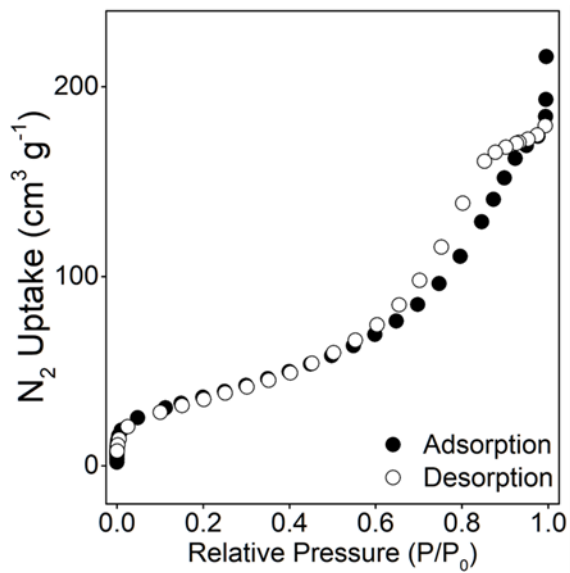


Figure 9. The desorption-adsorption graph of SR2, reported as example.

The thermal behavior of MLS and the corresponding SPIONs between 25 - 400 °C exhibits two distinct jumps: the first weight loss is attributed to the evaporation of physically adsorbed water on the surface of SPIONs and MLs ($T < 100$ °C). The second weight loss can be ascribed to the dehydroxylation of lepidocrocite (γ -FeO(OH)) from SPIONs surface within the temperature range of 200 - 300 °C.⁴⁴ The presence of iron hydroxides on SPIONs surface is confirmed by an alkaline pH when SPIONs powder is added to water ($\text{pH} \approx 9$). In the case of MLs the second peak can be also related to removal of lipid bilayer that occurs in the same range of temperature. An example of TGA is reported in Figure 10. Similar results were observed investigating liposomes and MLs with the same technique.^{45,46}

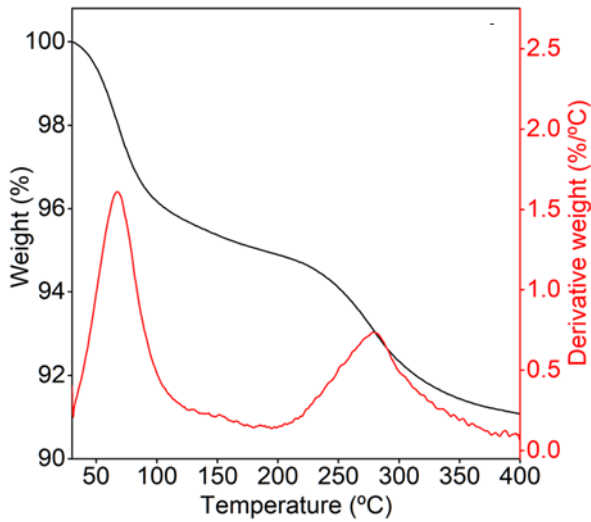


Figure 10. TGA measurement of SR2, reported as example.

To estimate the two distinct contributions in the case of MLs, we calculated the difference between the percentage of lepidocrocite obtained for SPIONs and the values observed for each ML formulation (Figure 11).

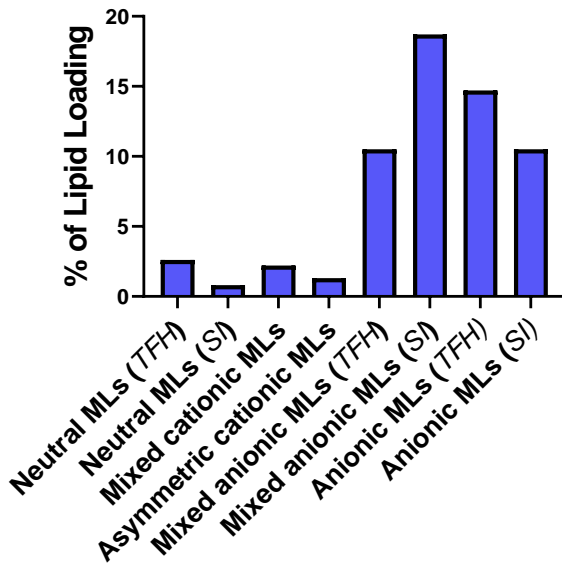


Figure 11. % of lipid coating, estimated through TGA experiments.

In the case of anionic MLs, the loss of lipid is significantly greater compared to cationic and neutral formulations using both techniques. This observation suggests that the strong interaction between SA and SPIONs results in a high loading of anionic lipids on the magnetic nanoparticle, consistent with findings observed using other techniques.

Our results put in evidence that the molecular structure of lipids and their distribution in the bilayer, affecting their interaction with the magnetic core of the aggregates, play a pivotal role in determining the properties of the functionalized SPIONs. Moreover, our findings clearly show that, besides the choice of the lipid components, the methodology used for MLs preparation (factor often neglected) has been crucial in influencing lipid organization and the effectiveness of SPIONs functionalization.

9.3 Molecular Dynamics Simulation Studies

In order to gain deeper understandings into the interactions between magnetite and lipids and to validate our hypotheses, theoretical calculations were conducted. The computational modeling of the investigated processes is an extremely challenging issue, essentially for two reasons. First of all, the size of the system (including nanoparticles, solvent, and surfactants) is beyond the possibilities of whatever computational tool at electronic level, e.g. quantum-chemical calculations. At the same time the alternative use of atomistic MD simulations, even using suitable force-fields, could be probably unable of modeling the (probably covalent, see below) interactions between some of the surfactants and the nanoparticle surface. Secondly, and somewhat related to the previous point, the chemical nature of the nanoparticle surface is not only an extremely complicated issue in itself⁴⁷ but, in the present case, is not even uniquely defined, hence preventing the design of a well-defined simulation setup. Nevertheless, we decided to address a simplified modeling our experimental observations with the specific

aim of supporting, with qualitative arguments, the physical hypothesis concerning nanoparticles first-layer coverage.

First of all, we carried out a series of density functional theory (DFT) calculations on simple model systems in order to shed a somewhat more quantitative light on the nature of the intimate interactions between the surfactants and the nanoparticle surface. For this purpose, we evaluated the bond-energies between a penta-coordinated iron-aquo-complex, a very simplified model of the nanoparticle octahedral termination (representing the most dense monolayer)^{48,49}, and a series of simple ligands: (i) OH⁻ ion; (ii) water molecule; (iii) acetic acid/acetate ion, mimicking the stearic/stearate surfactant; (iv) ammonium-methyl-phosphonate mimicking the lipidic surfactant and, finally, (v) tetramethyl ammonium mimicking the cationic surfactant. Note that, because of their semi-quantitative purpose, the calculations were not repeated in the case of the possible tetrahedral nanoparticle termination as they are conceivably supposed to provide binding energies of the same order of magnitude of the octahedral sites.

Excluding the tetramethyl ammonium, for which – as expected – we couldn't find any bound state, the resulting picture, is reported in the Figure 3A. The reported values indicate that all the ligands plausibly present in the system, excluding the cationic surfactant, are able to bind to the octahedral iron through an interaction of the order of 102-103 kJ/mol hence well beyond the thermal, i.e. semiclassical, interactions. Notably, also the solvent molecules involved in this study, i.e. water and chloroform, are expected to show a binding energy much higher than the thermal energy. This means that the specific formation of the bonds at the basis of the first surfactant layer and also at the basis of the absorption of the solvent molecules resemble chemical bonds more than semiclassical electrostatic interactions.

In other words, our results, although qualitatively, support the idea that the first layer of surfactants present on the nanoparticle surface, should be formed upon

chemisorption rather than upon a physisorption process. Among the ligands potentially present in the investigated systems, it is possible to delineate this order of affinity to the octahedral surface iron: $\text{OH}^- > \text{stearate} > \text{lipid} > \text{stearic acid} > \text{water} > \text{chloroform}$.

This could help to hypothesize plausible situations present on the magnetite surface that the various surfactants may encounter. In fact, on the basis of the previous data and also in the light of the alkaline pH observed upon nanoparticle dissolution in water, it can be supposed that the surface of the nanoparticles, before their interaction with the surfactants and not taking into account possible defects, are primarily covered by basic hydroxyl ions or by water molecules: both of which are capable of easily displacing the chloroform molecules (when present). These surface models are hereafter termed as Model 1 and Model 2, respectively. Consequently, in the second step of our computational modeling, we decided, through MD simulations, to address the study of the physical interaction of all the surfactants, for some of which preparatory to the formation of the (chemical) bond with the surface, using the two surface models above outlined. In particular, we calculated the free energy of the whole system as a function of the distance between the polar heads of the solvated surfactant and the nanoparticle. From these curves we then evaluated the equilibrium radial distribution of the surfactant species with respect to the nanoparticle surface. Additional details about these simulations, in particular the adopted force fields and the approximations utilized, are reported in the Supplementary Information.

The results suggest, again, that the cationic surfactant can hardly approach the nanoparticle surface even upon physical (electrostatic and /or hydrogen-bond) interactions. On the other hand, the sufficiently high concentration, observed in the proximity of the nanoparticle surface for (in particular) the stearate and the lipid surfactants, suggest that according to our model these two surfactants, although

well solvated by water, are able to reach the surface and – possibly – undertake the bonding with the surface.

In conclusion, our computational model, although only qualitatively, supports the idea that the formation of the first layer on the nanoparticle surface is more similar to a chemical bond rather than to a physical (weaker) interaction. The role of the latter interaction is however of primary importance for ensuring a sufficiently high surfactant concentration able (through the mass-action-law effect) to displace strongly interacting species such as hydroxyl ions, and even water, conceivably present on the nanoparticle surface.

9.4 APEOs Removal from Standard Solutions

The ability of MLs to remove OPEO and NPEO from standard solutions was tested. In a first test, MLs were dispersed into the standard solutions (0.03 mg/mL) upon sonication. After three days, we could remove 50-75% of pollutant. This approach, despite proved that APEOs partitioned in the lipid bilayer and thus they could be removed from water, took a very long time (especially if we think about an industrial process). In addition, sonication it is not suitable for large volumes and a centrifuge is necessary for an effective separation of the system from wastewater. For these reasons, we decided to add MLs powder to OPEO and NPEO standard solutions, even if it involves the use of nanoparticles in their aggregate forms, which results in a limited exposure of the lipid bilayer to the aqueous solution. We started from an initial concentration of MLs of 1.25 mg/mL, arriving to the optimal one of 0.125 mg/mL: interestingly, we observed that, even upon reducing the concentration of the system, we could obtain the same results in terms of APEOs removal. This behavior could be explained by the tendency of MLs to aggregate at higher concentrations, consequently diminishing the available surface for interaction with molecules in solution.

In the experimental procedure, we introduced MLs powder into the standard aqueous solution, allowing a 10-minute interval before utilizing an external magnet to remove the designed system. Subsequently, we analyzed the solution, and if the results were not satisfactory, we introduced a new aliquot of MLs powders. This process was iterated until no differences in APEOs removal were observed. We obtained the best results ($\approx 80\%$ of removal) after two additions of neutral formulation and twenty minutes in total (Figure 12). Mixed and asymmetric cationic formulations led to $\approx 60\%$ of OPEO and NPEO removal after three and two additions, respectively, while lower percentages were obtained using anionic and mixed anionic formulations (between 40% and 60%) and three additions of MLs powder.

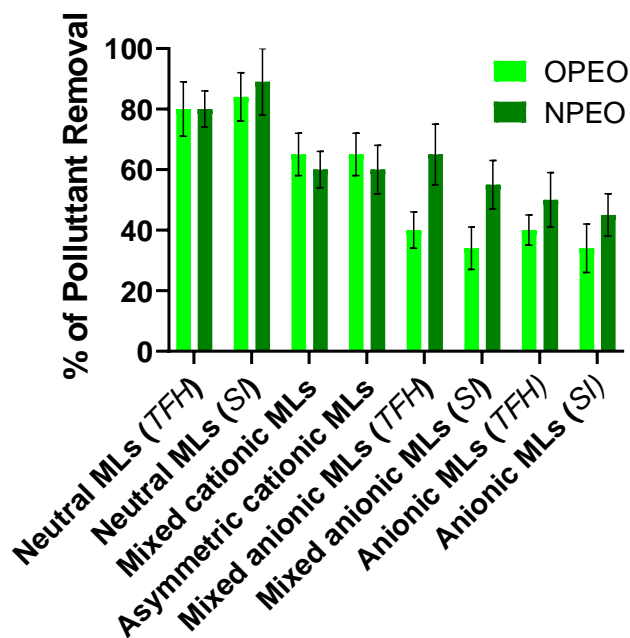


Figure 12. % of OPEO and NPEO removed from standard solutions using different formulations of MLs.

Our targeted analytes are not charged at pH of 7, so they could not establish electrostatic strong interactions with charged lipid bilayers: despite the great coating of anionic formulations, as pointed out by N_2 adsorption and TGA

experiments, their interaction with the pollutants (and thus their removal from water) was the smallest one. Mixed and asymmetric cationic formulations probably established cation- π interactions with the aromatic ring of OPEO and NPEO, increasing their removal with respect to anionic ones. Neutral formulation, instead, was the most effective one: the lack of charge probably favored the repartition of pollutants into the lipid bilayer. No differences in APEOs deletion were observed between pairs of MLs prepared following TFH or SI techniques.

APEO are surfactant having detergent properties,⁵⁰ so we conducted some analyses to evaluate if an higher concentration of APEOs (above their critical micellar concentration, cmc) could disrupt the lipid bilayer. We conducted ATR-FTIR and fluorescence microscopy analyses on ML that were in contact with an aqueous solution containing OPEO and NPEO above their cmc. In particular, the fluorescence microscopy analyses were conducted on MLs prepared using both TFH and SI techniques. In the latter case, the Dil was added separately in the first and second layer of ML. ATR-FTIR showed the typical signals of phospholipids, and the exposure of MLs samples to a FITC filter for fluorescence spectroscopy (excitation/emission wavelength respectively at 467-498 nm / 513-556 nm) always resulted in fluorescence emission. Thus, detergent surfactants do not disrupt the lipid bilayer. Despite these findings, we would like to emphasize that these results are purely qualitative and not quantitative.

Activated carbon, sludge, photocatalysis, ozonation, and ultrafiltration or nanofiltration are current methods for APEOs removal from water.⁵¹ However, activated carbon and sludge disposal poses environmental concerns, while advanced oxidation processes are energy-intensive and costly, potentially generating harmful byproducts.⁵² Membranes require frequent cleaning,⁵³ escalating operational expenses. Combining multiple techniques enhances removal but adds complexity and costs. In contrast, our system efficiently removes APEOs from water, minimizing energy consumption and preventing secondary pollution.

Additionally, in comparison to other nano systems reported in literature, MLs achieve higher removal percentages in shorter timeframes and maintains performance over multiple cycles. For instance, while *Laccase* immobilized on metal-organic frameworks effectively removes APEOs,⁵⁴ it is cost-prohibitive and loses efficacy over four cycles. A natural zeolite was then proposed for the removal of APEOs from aqueous media.⁵⁵ Nevertheless, the hydrophobic nature of the pollutants resulted in foam formation, creating a barrier on the adsorbent material, limiting pollutant removal. Finally, cyclodextrin polymers exhibit variable efficiency based on pollutant size:⁵⁶ in fact, the removal efficiency of NP was three times higher than the removal efficiency of NPEO.

The promising results obtained with neutral MLs in APEOs removal indicate that this formulation has very good potential in wastewater treatment. Our findings demonstrate that lipid molecular structure and organization are essential for the efficacy of the proposed system and that the proposed approach based on the systematic variation of MLs composition and on its correlation with their properties has paid off in optimizing the formulation of MLs for removal of APEOs and, potentially, of other pollutants from industrial wastewaters.

9.5 MLs Recycle

In the perspective of reuse the proposed system after the removal of pollutants, we decide to set up a recycle procedure. Initially, our strategy was desorbing the pollutant using an organic solvent in which OPEO and NPEO are soluble (ethyl ether, ethanol, or isopropanol). We conducted IR analysis of dry MLs powders after the contact with different organic solvents (ethanol, isopropanol, ethyl ether, chloroform, hexane, dimethyl sulfoxide, ethyl acetate and tetrahydrofuran), and we always observed the presence of lipid signals.

These findings are consistent with theoretical calculations, indicating a strong bond between Fe_3O_4 and SPC/SA that does not break in the presence of organic solvents.

Unfortunately, we have reasons to suspect that the second layer (or at least a part of it) might detach because of lipids solubility in these solvents. Subsequently, we explored an alternative approach: MLs were calcinated in order to remove the lipid coating and to reuse the calcinated magnetic nanoparticles (cal-MNPs) as core for preparing new MLs. We observed that ramp rate, temperature, and time of calcination played an important role in the composition of nanoparticles: if the calcination occurred at 10 °C/min, temperature higher than 550 °C, or for times exceeding 4 hours, the IR spectra of cal-MNPs showed a splitting of the peak related to the Fe-O bond. The best conditions of calcination that we could find for achieving the loss of lipids and no change in nanoparticles composition are: 400 °C, 30 min, ramp rate of 5 °C/min. With these conditions, IR spectra of cal-MNPs did not show any differences between cal-MNPs and SR2, while XRD indicated a change in the composition: a small percentage of magnetite transformed into goethite, indicated by the appearance of small peaks at 27.93, 38.65, 48.1 and 58.5 degrees starting from the third cycle and whose intensities increased until the fifth cycle (Figure 13).

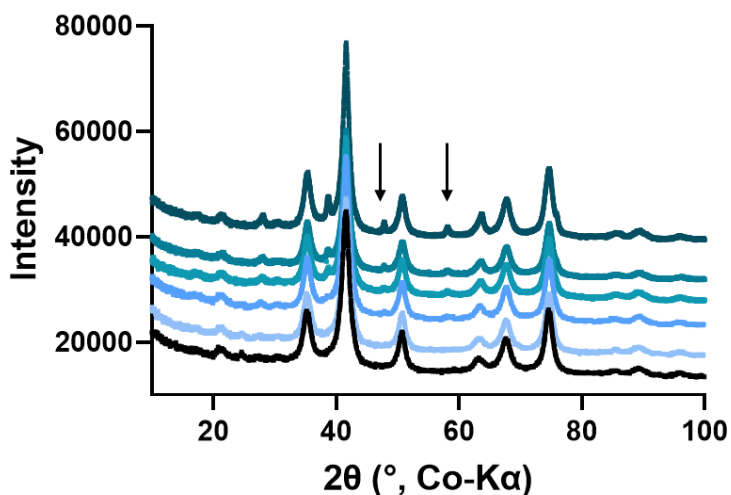


Figure 13. Comparison between XRD analysis performed on SR2 and Cal-MNPs (black line is referred to SR2, and from bottom to top: Cal1-MNPs to Cal5-MNPs). The two arrows indicate the main peaks associated with goethite.

Consequentially, the specific magnetization slightly decreased after 5 cycles (Figure 14). Upon close examination of the magnetization curve, the result of the fitting using multiple Langevin functions shows a slight progressive increase in the average particle size and, simultaneously, a decrease in the linear (paramagnetic) contribution at high fields. This is consistent with the hypothesis of progressive aggregation of the smaller particles due to the calcination process. The average diameter reaches 9.9 nm after the fifth cycle, to be compared with the initial 9.3 nm diameter.

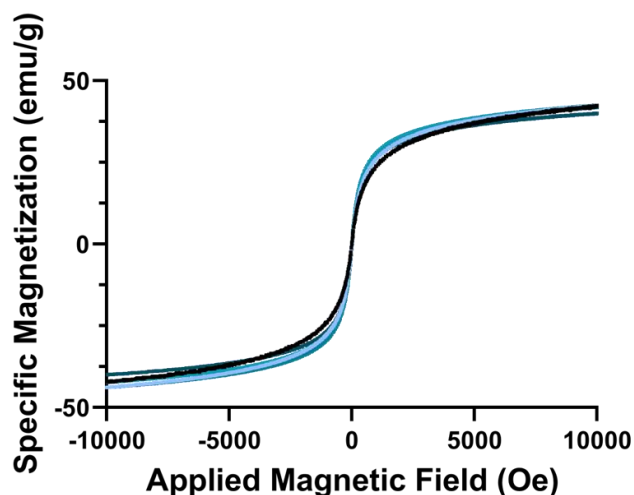


Figure 14. Comparison between specific magnetization of SR2 and Cal-MNPs (black line is referred to SR2, and from bottom to top: Cal5-MNPs – Cal1-MNPs).

The BET area after 5 calcination cycles diminished from 135 to 120 m²/g and proved the previous hypothesis regarding the aggregation process. Cal5-MNPs showed enhanced thermal stability (up to 400 °C) if compared to SR2, as revealed by TGA analysis: evidently, calcination process caused the loss of iron hydroxides that were present on the surface of SR2 samples.

These small changes in the composition of the magnetic core during calcination cycles did not hamper their coating process: we used the recycled nanoparticles for preparing new neutral MLs (the formulation that gave the best results) following

the TFH approach (which is simpler, quicker and require less amount of chloroform if compared to the SI one). Results in terms of OPEO and NPEO removal are slightly lower if compared to non-recycled analogous formulation (60% versus 80%, respectively, with two additions of MLs in both cases). The observed differences could be attributed to the aggregation process of magnetic nanoparticles, wherein a reduced surface/volume ratio may result in a diminished available surface for coating.

The good results obtained in assessing the recyclability of MLs further strengthen the potentiality of the proposed methodology as a simple, rapid, and cheap system for the treatment of wastewater and the removal of APEOs and reasonably of other persistent organic pollutants.

9.6 Conclusion

Considering the challenges associated with polluted wastewater, we conducted, for the first time, an examination of the potential of MLs for water remediation. Our approach aims to leverage the lipid bilayer of MLs as a preferred microenvironment that facilitates the partitioning of organic pollutants, while the magnetic core enables their easy and rapid removal from the aqueous environment. Furthermore, we thoroughly examined both the role of the methodology used for SPIONs and MLs preparation and the lipid composition (along with the potential synergy of these features) in influencing the performance of the functionalized nanoparticles. These distinctive aspects are often neglected or underestimated, but they may be critical in determining the properties and potential of the aggregates. ML demonstrated promise in removing common organic pollutants such as APEOs from aqueous solutions, with the bilayer charge playing a fundamental role in their removal efficiency. Theoretical calculations highlight that cationic surfactants do not effectively interact with the nanoparticle surface, even with supramolecular interactions. In contrast, the bond between SPIONs and neutral or anionic lipids is

comparable to a covalent bond, particularly in the latter scenario. Despite this strong bond, MLs can be recycled for at least five cycles, showing only a small decline in efficacy.

The main advantages of our system, compared to the main techniques used nowadays and reported in the introduction section, include that it does not require additional chemicals, is environmentally friendly, does not produce toxic by-products or sludge, offers a short treatment time, and is suitable for different lipophilic pollutants. However, potential disadvantages may include the saturation of the lipid bilayer of MLs in highly polluted wastewater, requiring additional MLs additions. The pH of the wastewater may play a pivotal role in the removal of pollutants, as these molecules may be neutral or protonated, varying their affinity for the lipid bilayer.

The simplicity of MLs preparation not only makes the scaling up of MLs production a relatively straightforward task, but also enhances the cost-effectiveness of the raw materials used, thus increasing the potential for real-world applications. The promising results obtained from this approach will be extended to the removal of other common organic pollutants such as polycyclic aromatic hydrocarbons and polychlorinated biphenyls from aqueous matrices. To deepen our understanding of the key parameters influencing the success of this technology in water remediation, we will evaluate the impact of varying lipid composition. This includes assessing the effects of adding cholesterol or using different anionic surfactants and/or saturated phospholipids. These further investigations could strengthen the robustness and the dependability of the proposed approach as a general solution for wastewater treatment.

9.7 Bibliography

1. Crini, G. & Lichtfouse, E. Advantages and disadvantages of techniques used for wastewater treatment. *Environmental Chemistry Letters* vol. 17 145–155 Preprint at <https://doi.org/10.1007/s10311-018-0785-9> (2019).
2. Wee, T., Kim, C. & Hanif, M. Review on Wastewater Treatment Technologies. *International Journal of Applied Environmental Sciences* **11**, 111–126 (2016).
3. El-Sayed Abdel-Raouf, M. *et al.* Wastewater Treatment Methodologies, Review Article. *International Journal of Environment & Agricultural Science* **3**, 18 (2019).
4. Bradl, H. B., Bradl, H. & Xenidis, A. *Heavy Metals in the Environment Remediation Techniques*.
5. Ezugbe, E. O. & Rathilal, S. Membrane technologies in wastewater treatment: A review. *Membranes* vol. 10 Preprint at <https://doi.org/10.3390/membranes10050089> (2020).
6. Iwuozor, K. O. *Prospects and Challenges of Using Coagulation-Flocculation Method in the Treatment of Effluents*. *Advanced Journal of Chemistry-Section A* vol. 2 <http://ajchem-a.com> (2019).
7. Benner, J. *et al.* Is biological treatment a viable alternative for micropollutant removal in drinking water treatment processes? *Water Research* vol. 47 5955–5976 Preprint at <https://doi.org/10.1016/j.watres.2013.07.015> (2013).
8. Tufail, A., Price, W. E., Mohseni, M., Pramanik, B. K. & Hai, F. I. A critical review of advanced oxidation processes for emerging trace organic contaminant degradation: Mechanisms, factors, degradation products, and effluent toxicity. *Journal of Water Process Engineering* **40**, (2021).
9. Rashid, R. *et al.* A state-of-the-art review on wastewater treatment techniques: the effectiveness of adsorption method. doi:10.1007/s11356-021-12395-x/Published.
10. Ahmed, M. B., Zhou, J. L., Ngo, H. H. & Guo, W. Adsorptive removal of antibiotics from water and wastewater: Progress and challenges. *Science of the Total Environment* vol. 532 112–126 Preprint at <https://doi.org/10.1016/j.scitotenv.2015.05.130> (2015).

11. Mon, M., Bruno, R., Ferrando-Soria, J., Armentano, D. & Pardo, E. Metal-organic framework technologies for water remediation: Towards a sustainable ecosystem. *Journal of Materials Chemistry A* vol. 6 4912–4947 Preprint at <https://doi.org/10.1039/c8ta00264a> (2018).
12. Liu, Z. M. *et al.* Novel hematite nanorods and magnetite nanoparticles prepared from MIL-100(Fe) template for the removal of As(V). *Mater Lett* **132**, 8–10 (2014).
13. Veloso, S. R. S., Andrade, R. G. D. & Castanheira, E. M. S. Magnetoliposomes: recent advances in the field of controlled drug delivery. *Expert Opin Drug Deliv* **18**, 1323–1334 (2021).
14. Soenen, S. J., Velde, G. Vande, Ketkar-Atre, A., Himmelreich, U. & De Cuyper, M. Magnetoliposomes as magnetic resonance imaging contrast agents. *Wiley Interdisciplinary Reviews: Nanomedicine and Nanobiotechnology* vol. 3 197–211 Preprint at <https://doi.org/10.1002/wnan.122> (2011).
15. Fortin-Ripoche, J. P. *et al.* Magnetic targeting of magnetoliposomes to solid tumors with MR imaging monitoring in mice: Feasibility. *Radiology* **239**, 415–424 (2006).
16. Nappini, S., Bombelli, F. B., Bonini, M., Nordèn, B. & Baglioni, P. Magnetoliposomes for controlled drug release in the presence of low-frequency magnetic field. *Soft Matter* **6**, 154–162 (2009).
17. Nappini, S. *et al.* Controlled drug release under a low frequency magnetic field: Effect of the citrate coating on magnetoliposomes stability. *Soft Matter* **7**, 1025–1037 (2011).
18. Babincová, N. *et al.* Applications of magnetoliposomes with encapsulated doxorubicin for integrated chemotherapy and hyperthermia of rat C6 glioma. *Zeitschrift fur Naturforschung - Section C Journal of Biosciences* **73**, 265–271 (2018).
19. Le, B. *et al.* Preparation of Tumor-Specific Magnetoliposomes and Their Application for Hyperthermia. *Journal of Chemical Engineering of Japan* vol. 34 (2001).
20. Shinkai, M. *et al.* Targeting Hyperthermia for Renal Cell Carcinoma Using Human MN Antigen-Specific Magnetoliposomes. *Jpn. J. Cancer Res* vol. 92 (2001).

21. Hamaguchi, S. *et al.* Selective hyperthermia using magnetoliposomes to target cervical lymph node metastasis in a rabbit tongue tumor model. *Cancer Sci* **94**, 834–839 (2003).
22. Thiele, B., Günther, K. & Schwuger, M. J. *Alkylphenol Ethoxylates: Trace Analysis and Environmental Behavior.* (1994).
23. Iwata, M., Eshima, Y., Kagechika, H. & Miyaura, H. The endocrine disruptors nonylphenol and octylphenol exert direct effects on T cells to suppress Th1 development and enhance Th2 development. *Immunol Lett* **94**, 135–139 (2004).
24. Priac, A. *et al.* Alkylphenol and alkylphenol polyethoxylates in water and wastewater: A review of options for their elimination. *Arabian Journal of Chemistry* vol. 10 S3749–S3773 Preprint at <https://doi.org/10.1016/j.arabjc.2014.05.011> (2017).
25. Acir, I. H. & Guenther, K. Endocrine-disrupting metabolites of alkylphenol ethoxylates – A critical review of analytical methods, environmental occurrences, toxicity, and regulation. *Science of the Total Environment* vol. 635 1530–1546 Preprint at <https://doi.org/10.1016/j.scitotenv.2018.04.079> (2018).
26. Lazzarini, A. *et al.* Investigation of physico-chemical and catalytic properties of the coating layer of silica-coated iron oxide magnetic nanoparticles. *Journal of Physics and Chemistry of Solids* **153**, 110003 (2021).
27. Kang, Y. S., Subhash Risbud, Rabolt, J. F. & Stroeve, P. Synthesis and Characterization of Nanometer-Size Fe₃O₄ and γ -Fe₂O₃ Particles. *Chem. Mater.* **8**, 2209–2211 (1996).
28. Smolkova, I. S. *et al.* Correlation between coprecipitation reaction course and magneto-structural properties of iron oxide nanoparticles. *Mater Chem Phys* **155**, 178–190 (2015).
29. Lagrow, A. P. *et al.* Unravelling the growth mechanism of the co-precipitation of iron oxide nanoparticles with the aid of synchrotron X-Ray diffraction in solution. *Nanoscale* **11**, 6620–6628 (2019).
30. Besenhard, M. O. *et al.* Co-precipitation synthesis of stable iron oxide nanoparticles with NaOH: New insights and continuous production via flow chemistry. *Chemical Engineering Journal* **399**, 125740 (2020).

31. Suppiah, D. D. & Johan, M. R. Influence of solution pH on the formation of iron oxide nanoparticles. *Mater Res Express* **6**, (2019).
32. Alp, E. & Aydogan, N. A comparative study: Synthesis of superparamagnetic iron oxide nanoparticles in air and N₂ atmosphere. *Colloids Surf A Physicochem Eng Asp* **510**, 205–212 (2016).
33. Winsett, J. *et al.* Quantitative determination of magnetite and maghemite in iron oxide nanoparticles using Mössbauer spectroscopy. *SN Appl Sci* **1**, 1–8 (2019).
34. Bagus, P. S., Nelin, C. J., Al-Salik, Y., Ilton, E. S. & Idriss, H. Multiplet splitting for the XPS of heavy elements: Dependence on oxidation state. *Surf Sci* **643**, 142–149 (2016).
35. Radu, T., Iacovita, C., Benea, D. & Turcu, R. X-Ray Photoelectron Spectroscopic Characterization of Iron Oxide Nanoparticles. *Appl Surf Sci* **405**, 337–343 (2017).
36. Shokrollahi, H. A review of the magnetic properties, synthesis methods and applications of maghemite. *J Magn Magn Mater* **426**, 74–81 (2017).
37. Dunlop, D. J. & Arkani-Hamed, J. Magnetic minerals in the Martian crust. *J Geophys Res Planets* **110**, 1–11 (2005).
38. Pereira, D. S. M. *et al.* Magnetoliposomes containing calcium ferrite nanoparticles for applications in breast cancer therapy. *Pharmaceutics* **11**, (2019).
39. Zhang, S. *et al.* Biocompatible phosphatidylcholine bilayer coated on magnetic nanoparticles and their application in the extraction of several polycyclic aromatic hydrocarbons from environmental water and milk samples. *J Chromatogr A* **1238**, 38–45 (2012).
40. Iconaru, S. L. *et al.* Magnetite (Fe₃O₄) nanoparticles as adsorbents for As and Cu removal. *Appl Clay Sci* **134**, 128–135 (2016).
41. Liu, Z. M. *et al.* Novel hematite nanorods and magnetite nanoparticles prepared from MIL-100(Fe) template for the removal of As(V). *Mater Lett* **132**, 8–10 (2014).
42. Khan, U. S., Khattak, N. S., Rahman, A. & Khan, F. Optimal method for preparation of magnetite nanoparticles. *Journal of the Chemical Society of Pakistan* **33**, 628–633 (2011).

43. Pozan, G. S., Isleyen, M. & Gokcen, S. Transition metal coated TiO₂ nanoparticles: Synthesis, characterization and their photocatalytic activity. *Appl Catal B* **140–141**, 537–545 (2013).
44. Mikhaylova, M. *et al.* BSA immobilization on amine-functionalized superparamagnetic iron oxide nanoparticles. *Chemistry of Materials* **16**, 2344–2354 (2004).
45. Elgharbawy, H. & Morsy, R. Preparation and Physicochemical Evaluation of Magnetoliposomes as Drug Carriers for 5-Fluorouracil Preparation and Physicochemical Evaluation of Magnetoliposomes as Drug Carriers for 5-Fluorouracil. (2018).
46. Aljihani, S. A. *et al.* Saudi Journal of Biological Sciences Enhancing azithromycin antibacterial activity by encapsulation in liposomes / liposomal-N-acetylcysteine formulations against resistant clinical strains of Escherichia coli. *Saudi J Biol Sci* **27**, 3065–3071 (2020).
47. Liu, H. & Valentin, C. Di. Shaping Magnetite Nanoparticles from First Principles. *Phys Rev Lett* **123**, 186101 (2019).
48. Arndt, B. *et al.* Surface Science Atomic structure and stability of magnetite Fe₃O₄ (001): An X-ray view. *Surf Sci* **653**, 76–81 (2016).
49. Noh, J., Osman, O. I., Aziz, S. G., Winget, P. & Bre, J. Magnetite Fe₃O₄ (111) Surfaces : Impact of Defects on Structure , Stability , and Electronic Properties. **4**, (2015).
50. Divya, B. & V.K., T. Laundry Detergents: An Overview. *J Oleo Sci* **56**, 327–340 (2007).
51. Palmer, M. & Hatley, H. The role of surfactants in wastewater treatment: Impact, removal and future techniques: A critical review. *Water Research* vol. 147 60–72 Preprint at <https://doi.org/10.1016/j.watres.2018.09.039> (2018).
52. Gautam, P., Kumar, S. & Lokhandwala, S. Advanced oxidation processes for treatment of leachate from hazardous waste landfill: A critical review. *Journal of Cleaner Production* vol. 237 Preprint at <https://doi.org/10.1016/j.jclepro.2019.117639> (2019).
53. She, Q., Wang, R., Fane, A. G. & Tang, C. Y. Membrane fouling in osmotically driven membrane processes: A review. *Journal of Membrane*

Science vol. 499 201–233 Preprint at
<https://doi.org/10.1016/j.memsci.2015.10.040> (2016).

54. Wang, D. *et al.* Laccase immobilization on core-shell magnetic metal-organic framework microspheres for alkylphenol ethoxylate compound removal. *J Environ Chem Eng* **9**, (2021).
55. Ucán, C. A. *et al.* Removal of an ethoxylated alkylphenol by adsorption on zeolites and photocatalysis with TiO₂/Ag. *Processes* **7**, (2019).
56. Bonenfant, D., Niquette, P., Mimeault, M., Furtos-Matei, A. & Hausler, R. UV-VIS and FTIR spectroscopic analyses of inclusion complexes of nonylphenol and nonylphenol ethoxylate with β -cyclodextrin. *Water Res* **43**, 3575–3581 (2009).

Chapter 10: Liposomes in the Process of Wool Dyeing

10. Exploring Liposomes to Enhance Sustainability in Wool

Dyeing

The process of wool dyeing can have significant environmental impacts, primarily due to the use of synthetic dyes and chemicals. The discharge of dyes into water bodies poses a threat to aquatic ecosystems, as these chemicals can be toxic to aquatic life and may lead to water pollution.¹ Additionally, the energy-intensive nature of dyeing processes and the consumption of large volumes of water contribute to the overall environmental footprint of wool dyeing,¹ emphasizing the need for sustainable and eco-friendly dyeing practices in the textile industry.

Recently, liposomes have been used in the wool dyeing process to enhance dye penetration, improve color uniformity, and minimize environmental impact through controlled release and reduced chemical usage.

Wool fibers are primarily composed of keratin, a protein that contains amino and carboxyl groups in the molecular structure.² These functional groups can ionize, leading to the development of a charged surface. At neutral pH, wool fibers have amphoteric properties.

Structurally, a wool fiber comprises cuticle and cortical cells bound by the Cell Membrane Complex (CMC, Figure 1).³

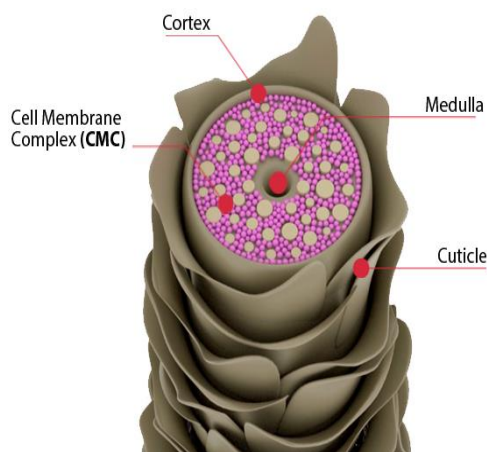


Figure 1. A schematic representation of the internal wool fiber.

This membranous structure is composed of internal wool lipids, constituting approximately 1.5% of the total fiber weight. These lipids consist of three main classes: sterols, free fatty acids, and polar lipids, including ceramides, cholesterol sulfate, and glycosphingolipids.⁴ Advances in characterizing the wool lipid composition and understanding the structure, arrangement, and thermotropic behavior of these lipid components have been made: internal wool lipids, demonstrated to form stable liposomes, and are believed to be arranged as lipid bilayers within the wool fiber.^{5,6} The existence of phospholipids in these bilayers might influence the permeability characteristics of dyes within the wool fiber. Typically, in the exhaustion method of dyeing a textile substrate, the dyeing process unfolds in three key stages:⁷

- diffusion of dye through the aqueous dyebath to the fiber surface;
- transfer of dye across the fiber surface;
- diffusion of dye from the surface throughout the entire fiber.

Achieving satisfactory shade development and fastness properties necessitates the complete penetration of dye into the fiber. The rate at which this occurs is regulated by the rate of dye diffusion across the fiber surface and subsequently throughout its entire internal structure.

The use of liposomes in the dyeing process of wool has showcased improved quality, energy efficiency, and reduced environmental impacts. Liposomes have the potential to decrease the quantity of dyes required for coloration⁸⁻¹⁰ and the working temperatures,^{9,11-13} resulting in substantial energy cost savings. Beyond sustainability considerations, incorporating liposomes into the dyeing process results in an improved final product quality. The fabric becomes more durable, exhibits a more vibrant color, and possesses increased brightness, elasticity, and softness.^{14,15}

Liposomes can impact the dyeing process by interacting with both the wool fibers and simultaneously with the dyestuffs.^{5,6,16} Dyes loaded-liposomes can adhere to the surface of wool fibers due to electrostatic forces or other attractive interactions; the lipid bilayer structure of liposomes may also absorb onto the wool fiber surface. This interaction leads to a deeper penetration of the loaded dye to wool fiber and can be influenced by the size and composition of the liposomes.

Based on these premises, we formulated various liposome formulations with the goal of reducing dye amounts in the dye bath and operating at lower temperatures. The results of these preliminary experiments were used to investigate how and to what extent the structure of lipids/surfactants influences the efficacy of the formulations in facilitating fibers dyeing. The final aim is to identify the essential characteristics of liposomes that grant an optimized wool dyeing thanks to these aggregates.

Commercial anionic or cationic surfactants (sodium lauryl sulfate, SLS, and cetyltrimethylammonium bromide, CTAB, respectively) were introduced at two molar ratios (20% or 30%) to a mixture of phospholipids with different chain length and degree of saturations extracted from soybean (SPC). This was done in the presence or absence of 30% cholesterol extracted from sheep wool to enhance the affinity between the wool fiber and the dye. Specifically, experiments

were conducted using two distinct water-soluble anionic metal complexes linked to azo groups, commonly employed as red and blue dyes (Chart 1). The major concerns associated with these compounds include: *i*) the presence of Cr (a heavy metal that is toxic to humans, animals, and the environment),¹⁷ and *ii*) the presence of azo groups, as they show resistance to biological oxidation¹⁸ and tend to decompose into carcinogenic aromatic amines.¹⁹

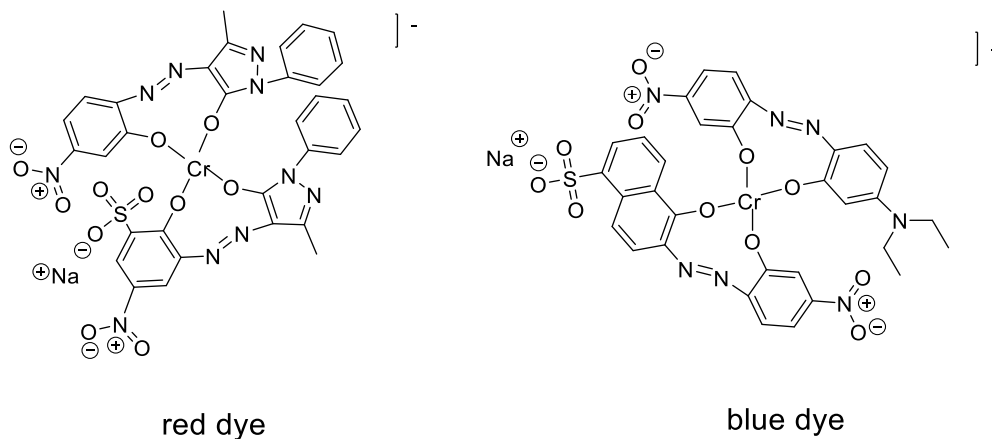


Chart 1. Red and blue dyes structures.

In this study, we recreated, on a reduced scale, a wool dyeing procedure conducted by an Italian textile company (Marchi & Fildi S.p.a., Biella, Italy). With the aim of enhancing the sustainability of the dyeing process, we employed two different approaches. The first one was based on pre-treating the wool samples with various empty liposomal formulations before the dyeing process. This was done as the absorption of liposomes by the wool is expected to enhance the diffusion of the dye within the fiber.²⁰ The second approach employed the use of dye-loaded liposomes, as liposomes can enhance the affinity between dyes and wool fibers and they may facilitate the penetration of dyes into the wool fibers.²⁰

We assessed the effectiveness of wool dyeing using liposomes by comparing the results with wool fibers obtained from the textile industry source. Our ultimate goal was to achieve wool samples with the same coloration as those dyed by the industry.

10.1 Liposome Preparation and Transition Temperature

Liposome formulations were prepared according to the Bangham methodology. It is well known that liposomes produced using this techniques exhibit heterogeneity in terms of size and the number of lipid bilayers.²¹ Consequently, we did not assess the size distribution of the prepared vesicles as we anticipated multiple populations with varying dimensions, ranging from approximately 200 nm to 1 μm . The size and lamellarity of liposomes are crucial for *in vivo* applications but not for a wool dyeing process. Therefore, we opted not to sonicate or extrude our formulations, aiming for a simple and rapid procedure that avoids the need for expensive instruments, streamlining the entire liposome production process.

DSC analysis performed on all formulations revealed the absence of peaks within the range of $-70\text{ }^{\circ}\text{C}$ to $100\text{ }^{\circ}\text{C}$. Using a mixture of phospholipids with a purity of 95% implies the presence of additional substances that may abolish the T_m , and this indicates that lipids maintain a fluid state throughout the entire dyeing process, with no alterations in the compactness of the double layer. As consequence, the dye release is easier when lipids are not tightly packed.

10.2 Dyes Entrapment

The red and the blue dyes were incorporated, separately, during the formation of liposomes through passive loading. The encapsulation efficiencies (EEs) of both dyes in mixed formulations are presented in Figure 2.

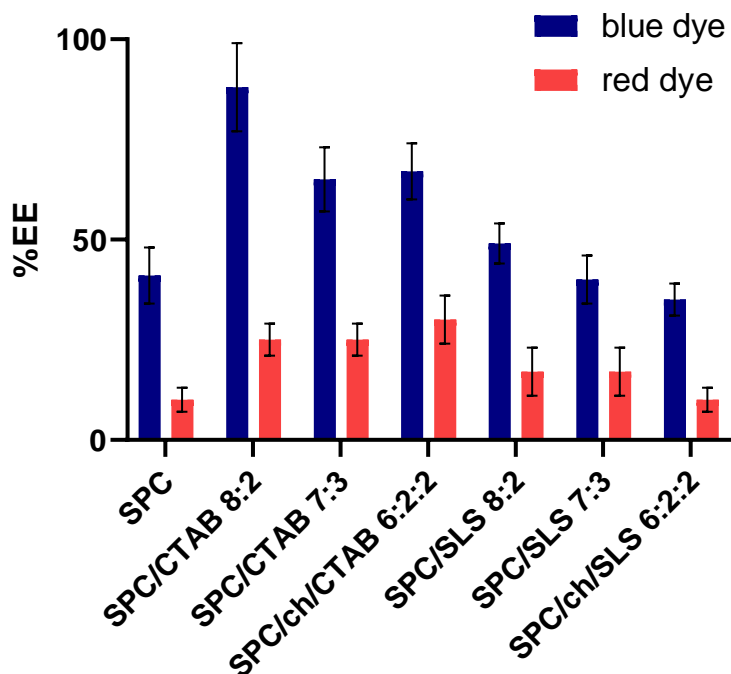


Figure 2. %EE of red and blue dyes in different liposome formulations.

Generally, higher percentages of EEs are observed for the blue dye compared to the red one. The reason is probably due to the facts that the blue dye exhibits lower water solubility compared to the red dye (5.7 g/L versus 135 g/L at 20 °C, respectively) and demonstrates a higher affinity for hydrophobic phases. This is evident in the partition coefficient values (LogK_{ow}): the LogK_{ow} of the blue dye is -0.95, while the LogK_{ow} of the red dye is -0.75.

In both cases, the highest EE values are observed in the presence of formulations containing CTAB, likely due to the establishment of electrostatic interactions between the negative charged dyes and the positively charged bilayer.

10.3 Pre-treatment of Wool Using Empty Liposomes

Wool was pre-treated by immersing it in a dispersion of each empty liposomal formulation (5% w/w relative to the wool sample) for one hour at room temperature.

At the end of the treatment, the wool sample was taken out from the liposomal dispersion and placed into a dye bath containing either red or blue dye, with concentrations of 0.8 mg/mL or 1.3 mg/mL, respectively. These amounts are reduced by half compared to the quantities utilized by the textile company. As in the industrial procedure, the dyeing process started at room temperature and was gradually increased at a rate of 2 °C/min until reaching 98 °C. The sample was then held at 98 °C for 40 minutes before being cooled to room temperature. Subsequently, the samples were washed with ultrapure water and they were air-dried.

To assess the colorimetric variations among the wool samples, various analyses were conducted using a portable colorimeter. The color difference (ΔE^*) between the samples was computed using the following formula:

$$\Delta E^* = \sqrt{\Delta L^2 + \Delta a^2 + \Delta b^2}$$

Here, ΔL^* , Δa^* , and Δb^* denote the differences in each chromatic coordinate between the samples dyed in the presence of liposomes and those provided by the textile industry (thus dyed in the absence of liposomes but with twice the amount of dyes). ΔE^* values exceeding 5 indicate perceptible colorimetric differences to the human eye. Conversely, ΔE^* values below 5 imply that there are no colorimetric differences detectable by the human eye between the two objects.^{22,23}

We also dyed a piece of wool that had not undergone pre-treatment with vesicles (control sample); this was done to determine whether the noted colorimetric

differences between the fabrics were truly attributed to the presence of liposomes.

In case of the red dye, all the fabrics exhibited colorimetric differences easily noticeable to the naked eye compared to the sample obtained from the textile industry (Figure 3).

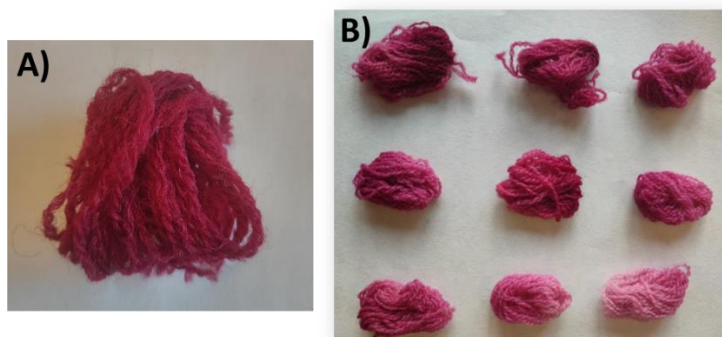


Figure 3. A) wool sample dyed by the textile industry with the red dye, and B) wool samples dyed using different liposome formulations.

We did not report the ΔE^* values observed between our samples and the one dyed by the textile industries: the lack of uniform coloration led to a very high standard deviation associated with the colorimetric measurements. In case of the blue dye, the ΔE^* values were around 8 units for all the samples, including the control sample that was not pre-treated with the vesicles. No significant differences were observed among the samples, indicating that the pre-treatment with different liposome formulations did not impact the final color of the fabrics.

Through spectrophotometric measurements, we evaluated the % of dye exhaustion at the end of the dyeing process. It represents a measure of the amount of dye absorbed by a textile material relative to the total amount of dye initially present in the dye bath, and was evaluated through spectrophotometric measurements. Specifically, we evaluated the ratio between the concentration of

the dye remaining in the dye bath after the dyeing process is complete and the concentration of the dye in the dye bath before the dyeing process begins.

This parameter provides information about the efficiency of the dyeing process (intended as the extent to which the textile material has absorbed the dye). Higher percentage of dye exhaustion values indicate more effective dyeing of the material. In case of the red dye, the percentage of dye exhaustion for all samples was approximately 100%, suggesting a complete absorption of the dye on the surface of the wool sample. Despite that, the coloration of the fabric was not uniform. We hypothesized that liposomes absorb, at some extent, on wool surface, preventing the dye from reaching the sample.

In case of blue dye, the percentage of dye exhaustion for the control sample was 85%, whereas it was almost quantitative for samples pre-treated with liposomes. Although no significant colorimetric differences were observed between the control sample and the samples pre-treated with liposomes, higher dye exhaustion implies lower quantities of dyes discharged into water basins at the end of the dyeing process. This result also indicates that the absorption of the dye on the fiber is not the only parameter to take into account, but also the depth of its penetration and its uniformity within the wool fiber.

10.4 Treatment of Wool Using Dye-loaded Liposomes

In this approach, wool samples were dyed by directly incorporating liposomes into the dye bath. The samples underwent dyeing in a bath containing both free dye and dye-loaded liposomes, without the separation of untrapped dye from the loaded vesicles. The dyeing process was conducted at 98°C and 78°C, allowing us to assess whether the presence of liposomes indeed enables an effective dyeing process and whether this advantage is maintained at a lower temperature. We also dyed a piece of wool in the absence of vesicles, as control sample.

The results obtained from these measurements highlight a noticeable difference between red and blue samples: it can be observed with the naked eye that the blue samples exhibit a much more uniform coloration compared to the red ones (Figure 3 and 4).



Figure 4. Wool samples dyed with the blue dye in the presence of liposomes.

Similar to the previous experiments with the red dye, an unsatisfactory coloration was achieved (visible by naked eye); in addition, a very high standard deviation was associated with the ΔE^* values (data not shown). In case of the blue dye, ΔE^* values between our samples and the one dyed by textile industry (with twice the amount of dye we used) are reported in Table 1.

Table 1. ΔE^* values between samples dyed in the presence of dye-loaded liposomes and the one dyed by textile industry (in the absence of liposomes but with twice the amount of dye we used).

Formulation	ΔE^*
Control Sample	8.2 ± 1.8
SPC	5.6 ± 2.7
SPC/CTAB 8:2	12.7 ± 1.9
SPC/CTAB 7:3	15.5 ± 3.5
SPC/ch/CTAB 6:2:2	12.9 ± 2.0
SPC/SLS 8:2	3.7 ± 1.0
SPC/SLS 7:3	4.7 ± 1.7
SPC/ch/SLS 6:2:2	4.4 ± 1.8

The dyeing process in the presence of loaded cationic formulations resulted in samples exhibiting worse coloration compared to the control sample, as indicated by colorimetric measurements and ΔE^* values. On the contrary, in the presence of loaded anionic formulations, the wool samples exhibited significantly improved coloration with respect to the control sample. In particular, the ΔE^* obtained by dyeing the wool in the presence of SPC/SLS 8:2 loaded vesicles was lower than 5 units. This indicates that no colorimetric difference with the sample dyed by the textile industry (treated using twice the amount of blue dye) could be observed. This result indicates that SLS interacts with the wool surface enhancing the dye penetration.

We repeated the dyeing process at a maximum temperature of 78 °C. In this case, the presence of liposomes led, in all instances, to samples having higher ΔE^*

values compared to the control sample. Probably, at low temperatures, the interaction between lipid vesicles and wool is weaker than at higher temperatures and no advantages in terms of coloration were obtained.

In this case as well, we assessed the % of dye exhaustion at the end of the dyeing process for both dyes and at both temperatures. Results for red and blue dyes are reported in Table 2 and Table 3, respectively.

Table 2. % of dye exhaustion for the red dye, at both 98 °C and 78 °C. Error, in all cases, is lower than 5%.

Formulation	% of dye exhaustion (98°C)	% of dye exhaustion (78 °C)
Control Sample	100%	100%
SPC	70%	50%
SPC/CTAB 8:2	43%	33%
SPC/CTAB 7:3	24%	10%
SPC/ch/CTAB 6:2:2	23%	39%
SPC/SLS 8:2	58%	65%
SPC/SLS 7:3	66%	67%
SPC/ch/SLS 6:2:2	63%	57%

Table 3. % of dye exhaustion for the blue dye, at both 98 °C and 78 °C. Error, in all cases, is lower than 5%.

Formulation	% of dye exhaustion (98 °C)	% of dye exhaustion (78 °C)
Control Sample	75%	82%
SPC	79%	72%
SPC/CTAB 8:2	35%	54%
SPC/CTAB 7:3	45%	44%
SPC/ch/CTAB 6:2:2	53%	49%
SPC/SLS 8:2	70%	62%
SPC/SLS 7:3	80%	67%
SPC/ch/SLS 6:2:2	70%	72%

For the red dye, at both 98 °C and 78 °C, the % of dye exhaustion in samples dyed in the presence of liposomes is consistently lower compared to the control sample, which had a complete dye exhaustion. This indicates that liposomes do not facilitate the interaction between wool and the dye but, on the contrary, their presence hinders the dyeing process. These results are consistent with the colorimetric measurements: the coloration is not uniform and we registered high ΔE^* and standard deviation values.

For the blue dye at 98 °C, the percentage of dye exhaustion in samples dyed with loaded cationic liposomes is lower compared to the control sample, whereas samples dyed in the presence of loaded anionic liposomes showed no significant differences in the percentage of dye exhaustion compared to the control sample. These findings align well with the colorimetric results: samples treated with loaded anionic formulations in the dye bath exhibited enhanced coloration compared to the control sample. In case of dyeing process at reduced

temperature, the % of dye exhaustion in samples dyed in the presence of all liposome formulations is consistently lower compared to the control sample, in good agreement with colorimetric results.

10.5 Interactions Between Liposomes and Wool

Following the dyeing process and the obtained results, we sought a deeper understanding of the interaction between wool fibers and liposomes. To delve into this, we conducted STEM analysis on various pieces of wool dyed with or without vesicles. As depicted in Figure 5, it becomes evident that the SPC95/SLS 8:2 formulation, which gave the best colorimetric results, exhibits interaction with the wool fiber. Notably, spherical aggregates are visible on the fiber's surface, indicating that liposomes do not remain in solution but tend to adhere to the fabric. Conversely, the wool fiber dyed without liposomes displayed distinct shapes; in contrast, the piece dyed in the presence of vesicles lacks well-defined shapes and exhibits a gel-like structure.

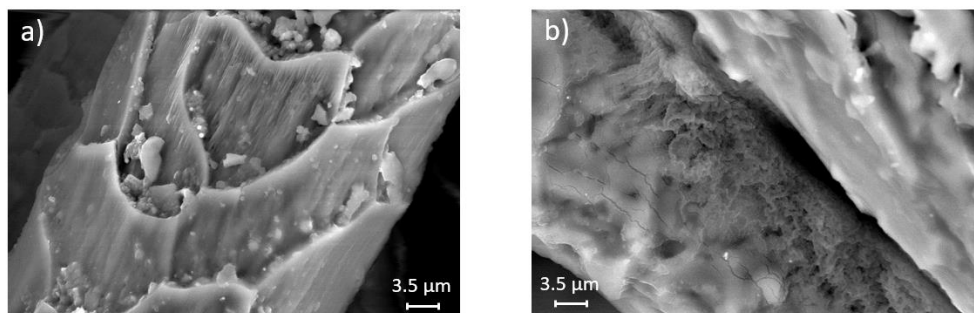


Figure 5. STEM analysis performed on a wool sample a) dyed in the absence of vesicles or b) in the presence of them.

10.6 Dyes Removal from Wastewater Using MLs

Loaded anionic formulation gave promising results in terms of wool coloration using the blue dye: we were able to achieve a wool sample with no discernible colorimetric differences compared to a sample dyed in the presence of twice the

amount of dye we used. Despite this outcome, the % of dye exhaustion - even in the presence of these formulations - indicates that a substantial amount of dye remains in solution. Given that, in the industrial process, the dye that remains in solution is typically discharged into water basins, we conducted tests with the ML formulations to address this type of pollutant in pursuit of a fully sustainable dyeing process. The procedure for the removal of the red and blue dye from aqueous solutions is the same described in [Chapter X](#) for the removal of APEOs. Results are shown in Figure 6.

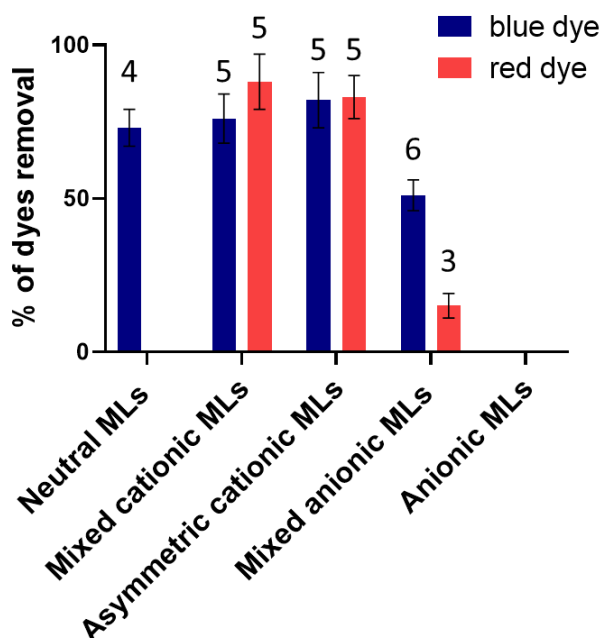


Figure 6. % of red or blue dye removed from aqueous solution using different ML formulations. The number above the bar is related to the total aliquots of MLs added to the aqueous solutions containing the dyes.

As expected, mixed or asymmetric cationic MLs proved to be effective in removing both red and blue dyes, achieving removal percentages exceeding 80% after the addition of five aliquots. Electrostatic interactions between the anionic

dyes and the cationic bilayers were likely established, and despite the water solubility of the pollutants, they partitioned into the lipid bilayer of MLs. Anionic MLs were unable to remove either red or blue dyes, which was an expected outcome, given the unfavorable electrostatic interactions between MLs and the dyes. On the other hand, mixed anionic MLs could remove approximately 50% of the blue dye with six aliquots and less than 20% of the red dye with three aliquots. The distinction between the two dyes is likely attributed to the lower water solubility of the blue dye compared to the red dye and its higher affinity for hydrophobic phases. Neutral MLs, instead, could remove only the 70% of blue dye after the adding of four aliquots.

10.7 Conclusion

In this study, various liposome formulations were employed in a wool dyeing process with the aim of reducing the required amount of dye and lowering working temperatures. Our preliminary experiments aimed to identify the parameters controlling the interaction between liposomes, dyes, and wool, as well as to determine the essential liposomal characteristics for an effective dyeing process using liposomes.

We observed that liposomal formulations proved effective for the blue dye yielding unfavorable results when applied with the red dye. At the same time, all the cationic formulations consistently resulted in poor coloration and unevenness of the sample, whether using red or blue dyes. Anyway, using anionic liposomes we managed to halve the blue dye quantity while achieving comparable colorimetric outcomes to those obtained by a textile industry using double the amount of the same dye. Thus, the effectiveness of liposomes in the dyeing process is clearly linked to their composition and our results put in evidence the importance of a systematic approach that correlates process efficiency with formulation properties. Anyway the obtained preliminary results demonstrated that liposomes have a great potential to reduce the environmental impact of the

textile industry, even if additional experiments are required to further our understanding of the process and optimize liposomes composition for even better results.

Additionally, we demonstrated that MLs are a promising resource for removing these two dyes from wastewater. Despite the hydrophilic nature of the dyes, they could be removed from the aqueous solutions. In this case, with the dyes being anionic, the charge of MLs played a pivotal role in their removal from aqueous solutions.

10.8 Bibliography

1. Madhav, S., Ahamad, A., Singh, P. & Mishra, P. K. A review of textile industry: Wet processing, environmental impacts, and effluent treatment methods. *Environmental Quality Management* **27**, 31–41 (2018).
2. Hassan, M. M. & Carr, C. M. A review of the sustainable methods in imparting shrink resistance to wool fabrics. *Journal of Advanced Research* vol. 18 39–60 Preprint at <https://doi.org/10.1016/j.jare.2019.01.014> (2019).
3. Rippon, J. A. *The Structure of Wool*. (2013).
4. Ramírez, R. *et al.* Liposome formation with wool lipid extracts rich in ceramides. *J Liposome Res* **19**, 77–83 (2009).
5. Ramírez, R. *et al.* Liposome formation with wool lipid extracts rich in ceramides. *J Liposome Res* **19**, 77–83 (2009).
6. Martí, M., Parra, J. L. & Coderch, L. *Lipid Role in Wool Dyeing*. www.intechopen.com.
7. Drumond Chequer, F. M. *et al.* Textile Dyes: Dyeing Process and Environmental Impact. in *Eco-Friendly Textile Dyeing and Finishing* (InTech, 2013). doi:10.5772/53659.
8. de la Maza, A., Parra, J. L., Bosch, P. & Coderch, L. Large Unilamellar Vesicle Liposomes for Wool Dyeing: Stability of Dye-Liposome Systems and Their Application on Untreated Wool. *Textile Research Journal* **62**, 406–413 (1992).
9. Montazer, M., Validi, M. & Toliyat, T. Influence of temperature on stability of multilamellar liposomes in wool dyeing. *J Liposome Res* **16**, 81–89 (2006).
10. El-Zawahry, M. M., El-Shami, S. & El-Mallah, M. H. Optimizing a wool dyeing process with reactive dye by liposome microencapsulation. *Dyes and Pigments* **74**, 684–691 (2007).
11. Montazer, M., Zolfaghari, A., Toliyat, T. & Moghadam, M. B. Modification of wool surface by liposomes for dyeing with weld. *J Liposome Res* **19**, 173–179 (2009).
12. Montazer, M., Taghavi, F., Toliyat, T. & Fallahpour, S. MLV Liposomes in Dyeing of Wool with Madder.

13. Martí, M., Coderch, L., de la Maza, A. & Parra, J. L. Liposomes of phosphatidylcholine: A biological natural surfactant as a dispersing agent. *Coloration Technology* **123**, 237–241 (2007).
14. Ru, J., Qian, X. & Wang, Y. Low-Salt or Salt-Free Dyeing of Cotton Fibers with Reactive Dyes using Liposomes as Dyeing/Level-Dyeing Promotors. *Sci Rep* **8**, 1–9 (2018).
15. Kartal, G. E., Sark, A. M., Erkan, G., Öztürk, E. A. & Öztürk, B. Effects of Phosphatidylcholine/Cholesterol Liposome-Assisted Dyeing on Woolen Fabric Properties. *Journal of Natural Fibers* **18**, 937–953 (2021).
16. Martí, M. *et al.* Physicochemical Aspects of the Liposome-Wool Interaction in Wool Dyeing. (2004) doi:10.1021/la030385.
17. Basha, S. A. & Rajaganesh, K. *Microbial Bioremediation of Heavy Metals From Textile Industry Dye Effluents Using Isolated Bacterial Strains.* *Int.J.Curr.Microbiol.App.Sci* vol. 3 <http://www.ijcmas.com> (2014).
18. Gottlieb, A., Shaw, C., Smith, A., Wheatley, A. & Forsythe, S. *The Toxicity of Textile Reactive Azo Dyes after Hydrolysis and Decolourisation.* www.elsevier.com/locate/jbiotec.
19. Berradi, M. *et al.* Textile finishing dyes and their impact on aquatic environs. *Heliyon* vol. 5 Preprint at <https://doi.org/10.1016/j.heliyon.2019.e02711> (2019).
20. Martí, M., Parra, J. L. & Coderch, L. *Lipid Role in Wool Dyeing.* www.intechopen.com.
21. Liu, G., Hou, S., Tong, P. & Li, J. Liposomes: Preparation, Characteristics, and Application Strategies in Analytical Chemistry. *Critical Reviews in Analytical Chemistry* vol. 52 392–412 Preprint at <https://doi.org/10.1080/10408347.2020.1805293> (2022).
22. Gabriele, F. *et al.* New oxidative alginate-biocide hydrogels against stone biodeterioration. *Int Biodeterior Biodegradation* **163**, (2021).
23. Nogueira, A. D. & Della Bona, A. The effect of a coupling medium on color and translucency of CAD-CAM ceramics. *J Dent* **41**, (2013).

11. General Conclusion

Lipid aggregates have garnered significant attention for their promising roles in drug delivery and environmental applications, a recognition well-supported by existing literature. Nevertheless, this thesis underscores a critical nuance: while lipid-based systems exhibit vast potential, their universal applicability across specific contexts is not guaranteed. To address this, we employed a systematic approach, sought to identify the crucial parameters and structural components that determine the success of a formulation within a designated application.

The analysis of the physicochemical properties of various formulations revealed that even slight modifications in molecular structure play a crucial role in governing the arrangement of components within lipid-based aggregates, influencing their effectiveness in practical applications.

In summary, the outcomes presented in this doctoral thesis support the methodology of linking molecular structure to the physicochemical behavior of aggregates and, consequently, their efficacy in their intended applications. Furthermore, the results obtained enable a partial rationalization of certain parameters influencing the interactions between the studied lipid aggregates and their intended targets, whether biological or not.

12. Experimental Procedures

1. Preparation of Samples

1.1 Preparation of Liposomes According to the Bangham Method

Liposomes were prepared according to the Bangham method (also called Thin Film Hydration method, TFH).

A proper amount of lipids was dissolved in one mixture of chloroform/ methanol in a round-bottom flask. The solvent was evaporated to obtain lipid films, that were stored under reduced pressure (0.4 mbar) for at least 6 h. The lipid films were hydrated with PBS solution (150 mM, pH 7.4, that may contain the hydrophilic drug), then were heated and vortex-mixed, obtaining MLVs. SUVs were obtained after sonication in ice-water bath of the MLVs suspension (10 min, 72 W, cycles 0.5 s).

The final concentration of the dispersion was 5 mM in lipid content, the final concentration of LD was 1.5 mg/mL, the final concentration of AA was 0,3 mg/mL, the final concentration of Qu was 0.25 mg/mL.

1.2 Preparation of Liposomes According to the Reverse Phase Evaporation Technique

A proper amount of lipids was solubilized in one mixture of chloroform/ methanol in a round-bottom flash, and then the solvent was removed using a rotavapor. Then, lipids were solubilized again in an organic solvent, and PBS buffer (150 mM, pH 7,4, that may contain the hydrophilic drug) was added. This two-phase solution was emulsinated using a bath sonicator for 5 min at room temperature and the organic solvent was slowly removed using a rotavapor. The

temperature was set to 25 °C and the pressure was reduced to 50 mbar every 5 min, starting from 550 mbar until 130 mbar. At this point, PBS 150 mM was added, and the dispersion was vortex-mixed. After that, it was returned to rotavapor at 150 mbar until the suspension was homogeneous. The final concentration of the liposomal dispersion was 10 mM in lipid content. The dispersion was then sonicated using a tip sonicator for 10 min (72 W, circles 0.5 s). The final concentration of the dispersion was 10 mM in lipid content, the final concentration of VAN was 3 mg/mL.

1.3 Preparation of LMPs-based beads

MO was transferred in sealed glass vials and molten at 50 °C. Subsequently, the molten lipid was loaded in a 1 mL Hamilton syringe and then dispensed into cold ultrapure water at approximately 2 °C maintaining magnetic stirring at 200 rpm as described in Figure 1. For beads enriched with VitE, the molten MO was blended with either 20% (w/w) or 45% (w/w) of VitE, and the beads were prepared as previously described. In the case of drug-loaded beads, the molten MO was combined with TOFA, BUPI, RAPA, or GEFI at three different percentages: 0.1% w/w (equivalent to 1 mg per 1 g), 1% w/w (equivalent to 10 mg per 1 g), and 5% w/w (equivalent to 50 mg per 1 g). This mixture was stirred for 30 min at 200 rpm and then sonicated for 10 minutes. The resulting molten dispersion was used to create the drug-loaded beads following the previously explained procedure (Figure 1).

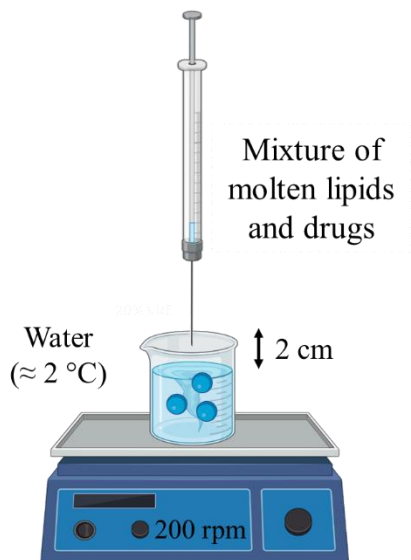


Figure 1. A schematic representation of LMPs-based beads preparation.

1.4 Preparation of SPIONs

SPIONs were prepared following two different procedures, based on co-precipitation, adapted from literature.^{1,2}

Briefly, in the first methodology, 0.0043 moles of $\text{FeCl}_2 \cdot 4\text{H}_2\text{O}$ and 0.0086 moles of $\text{FeCl}_3 \cdot 6\text{H}_2\text{O}$ were dissolved in 40 mL of ultrapure water and were left under stirring at 85 °C for one hour. Then 2.5 mL of NH_3 (30% v/v in H_2O) were added to the solution, which was continuously stirred for an additional 20 minutes while maintaining the same temperature. Subsequently, the solution was allowed to cool down to room temperature. The entire process took place within an atmosphere of nitrogen gas. The liquid phase containing the freshly synthesized SPIONs was isolated through centrifugation at 5000 (RPM) for 20 minutes. The supernatant was removed, leaving behind the nanoparticles. To further purify the SPIONs, they were subjected to three washing cycles using a NaOH solution adjusted to a pH of 9. Subsequently, SPIONs underwent to an additional washing

step using a solution containing 0.02 M NaCl and, finally, they were dried in air at 150 °C for 15 hours.

In the second methodology, a mixture was prepared by combining 0.85 mL of HCl 12.1 M with 25 mL of purified water that had been deoxygenated through nitrogen gas bubbling for 30 minutes. Successively, 0.02 moles of FeCl₃·6H₂O and 0.01 moles of FeCl₂·4H₂O were added under stirring. The resultant solution was then carefully added drop by drop to 250 mL of a 1.5 M NaOH solution under intense stirring. The precipitate was separated from the liquid supernatant through centrifugation (5000 RPM, 20 minutes) and it was washed three times with ultrapure deoxygenated water. A final washing cycle using HCl 0.01 M was performed, then SPIONs were air-dried under pressure (0.4 bar) at room temperature.

1.5 Preparation of MLs According to the Thin Film Hydration Technique

Briefly, 100 mg of SPIONs were washed with methanol to remove water traces, and then they were dispersed in chloroform through sonication. 5·10⁻⁵ moles of lipid were added to the obtained dispersion, which was evaporated under reduced pressure to obtain a dry film. 4 mL of ultrapure water were added, and the film was dispersed upon sonication. After 12 hours, the supernatant was discharged, and the precipitate (MLs) was washed three times with ultrapure water, and they were dried under pressure (0.4 bar) at room temperature.³

Fluorescent MLs were prepared using a mixture of SPC and DII (40:1 molar ratio), mixed anionic or cationic MLs were prepared using a mixture of SPC and SA or DDAB, respectively (5/5 molar ratio), and, finally, anionic, or cationic MLs were prepared using SA or DDAB, respectively.

1.6 Preparation of MLs According to the Solvent Injection Technique

MLs were also prepared following a two-steps procedure adapted from literature.⁴ Briefly, a dispersion of SPIONs in chloroform (40 mg in 40 mL) was prepared upon sonication. 0.0003 moles of lipid in methanolic solution were added under vigorous stirring to form the first lipid layer. Coated SPIONs were collected after centrifuge (5000 RPM, 1 hour) and were washed three times with ultrapure water. Then they were dispersed in ultrapure water (40 mg in 40 mL) upon sonication, and the second layer was attached following the injection of 0.0003 moles of lipid in methanolic solution. The resulting MLs were collected after centrifuge (5000 RPM, 1 hour) and washed three times using ultrapure water, and they were dried under pressure (0.4 bar) at room temperature.

Fluorescent MLs were prepared using a mixture of SPC and DII (40:1 molar ratio), mixed anionic or cationic MLs were prepared using a mixture of SPC and SA or DDAB, respectively (5/5 molar ratio), asymmetric anionic or cationic MLs were prepared using SPC for the first layer and SA or DDAB, respectively, for the second layer and, finally, anionic, or cationic MLs were prepared using SA or DDAB, respectively.

DSC measurements were conducted on a Mettler Toledo DSC 3 calorimeter (Mettler-Toledo International Inc., Columbus, OH, USA)

In case of liposomes, we analyzed MLVs 150 mM. Two heating scans were recorded at a rate of 5 °C/min followed by two heating scans at a rate of 1 °C/min. An pan containing PBS (150 mM, pH 7.4) was used as reference. Temperatures were determined with an accuracy of ± 0.1 °C and ΔH values with an accuracy of ± 0.5 kJ/mol.

In case of LMPs-based beads, samples were rapidly cooled from room temperature to -10 °C, maintaining this temperature for 10 minutes, and followed by gradual heating to 40 °C (rate of 2 °C/min).⁵ An empty pan was used as reference. Temperatures were determined with an accuracy of ± 0.5 °C and ΔH values with an accuracy of ± 0.5 kJ/mol.

In all cases, 40 μ L aluminum pans were used. These experiments were performed in triplicate, obtaining three reproducible thermograms each time.

2.2 ATR-IR analysis

FT-IR analyses were carried out on dry powders using a PerkinElmer Spectrum Two device, which was equipped with an atmospheric UATR Two accessory and a DTGS detector. Each spectrum was generated by averaging 16 scans, employing a resolution of 1 cm^{-1} within the 4000–400 cm^{-1} range.

2.3 Fluorescence Microscopy Analysis

A small amount of dried MLs was observed with a Nikon T1-U inverted microscope, equipped with a FITC filter (excitation 467 nm - 498 nm /emission 513 nm - 556 nm) useful for the carbocyanine containing dye present in the

sample); images were recorded with a Basler camera and managed with ImageJ 1.53t.

2.4 X-ray Diffraction (XRD) Measurements

Measurements were run on a PANalytical X'Pert PRO MPD θ/θ , Bragg-Brentano powder diffractometer, using Fe filtered Co-K α ($\lambda=1.7903$ Å) radiation, performing $2\theta/\theta$ scans from 7 to 100° 2θ . Samples powders were loaded in silicon zero background sample holders. Fittings were performed using X'Pert HighScore Plus, to match them with the reference structures from Crystallographic Open Database (COD) of magnetite (96-900-5813), maghemite (96-900-6317) and goethite (96-901-6407).

2.5 X-ray Photoelectron Spectroscopy (XPS) Measurements

X-ray photoelectron spectroscopy (XPS) data were collected with a PHI ESCA-5500 photoelectron spectroscope (X-ray source Al 1486.6 eV mono at 300.0 W). All the spectra were referenced using C1s reference at 284.8 eV.

2.6 Scanning Transmission Electron Microscopy (STEM)

Analysis

Samples were dispersed in ultrapure water upon sonication, then 2/3 drops were placed on a copper grid (200 mesh) with an amorphous carbon film. After solvent evaporation, samples were analyzed using a Zeiss Gemini SEM 500 microscope equipped with an aSTEM detector.

2.7 N₂ Adsorption-Desorption Measurements

The measurements were run on a ASAP Micromeritics Tristar 3000. 10 mg of each sample were subjected to heating at 100 °C and 10⁻⁶ Torr for 16h prior to the measurements.

2.8 Thermogravimetric Analysis (TGA)

TGA was performed on a Mettler-Toledo TGA-851e thermobalance. The samples were loaded under an atmosphere of dry nitrogen with a 50 mL/min flow.

2.9 Alternating Gradient Field Magnetometry (AGFM) Analysis

Magnetization profiles were acquired using a PMC Micromag MicroMag 2900 Alternating Gradient Field Magnetometer (AGFM) provided by Lakeshore Cryotronics. Sample powders were carefully weighed and positioned encapsulated within a hand-homemade sample holder. Measurements were executed at room temperature, involving the manipulation of the magnetic field up to a maximum magnetic field of 12 kOe.

2.10 Small-Angle X-ray Scattering (SAXS) and Wide-Angle X-ray Scattering (WAXS)

Measurements were performed on a Bruker AXS Micro, with a microfocused X-ray source, operating at voltage and filament current of 50 kV and 1000 μ A, respectively. The Cu K α radiation ($\lambda_{\text{Cu K}\alpha} = 1.5418 \text{ \AA}$) was collimated by a 2D Kratky collimator, and the data were collected by a 2D Pilatus 100K detector (or 1D VÅNTEC-1 detector in case of WAXS). The scattering vector $Q = (4\pi/\lambda)\sin\theta$, with 2θ being the scattering angle, was calibrated using silver behenate. Data were collected and azimuthally averaged using the Saxsgui software to yield 1D intensity vs. scattering vector Q , with a Q range from 0.001 to 0.5 \AA^{-1} (and from

13 to 20 nm⁻¹ for WAXS). For all measurements, a bead was placed inside a stainless-steel cell between two thin replaceable mica sheets and sealed by an O-ring. Samples were equilibrated for 30 min before measurement, whereas scattered intensity was collected over 30 min. Measurements were performed at 25 and 37°C. To determine the structural parameters such as the size of the water channels (d_w), SAXS data about the lattice (a) were combined with the composition of the samples.⁶

2.11 Rheology Experiments

A stress-controlled rheometer (Modular Compact Rheometer MCR 72 from Anton Paar, Graz, Austria) was used in cone-plate geometry, 1.001° angle, and 24.967 mm diameter. The temperature control was set at 25 °C. A strain sweep was performed at 10 s⁻¹ between 0.001 and 100% shear strain to determine the linear viscoelastic regime, and the yield (τ_y) and flow (τ_f) points. τ_y is exceeded at the point where the shear stress starts to deviate from linearity, while τ_f is represented by the shear stress value at the crossover point where G' equals G'' . Both values are extrapolated from amplitude sweep graphs.

Thixotropy properties of the beads were determined by using hysteresis experiments which consisted of a three-step operation: upward curve (1% shear strain, frequency of 1 Hz), plateau curve (shear rate of 1000 s⁻¹) and downward curve (1% shear strain, frequency of 1 Hz). The percentage of regeneration of MO-B and MO/VitE-B soon after their preparation was determined using the following equation:

$$\% \text{ of regeneration} = \frac{G' \text{ at rest}}{G' \text{ after stress}} \cdot 100$$

where the values of G' at rest and G' after stress were extrapolated from the thixotropy graphs.

3. HPLC methods

3.1 Levodopa

LD was detected by reverse-phase liquid chromatography using a Macherey-Nagel Nucleosil 100-5 C18 (4.0 x 250 mm; 5.0 μm particle size) column, kept at 25 °C. The mobile phase consisted of water/acetonitrile 80:20 v/v (each solvent was acidified with 0.01% phosphoric acid) at a flow rate of 0.7 mL/minutes, and UV detection at $\lambda = 280 \text{ nm}$. Data were collected and analyzed using the software Chromeleon 7 (Thermo Fisher).

The detection limit of LD is 10 $\mu\text{g/mL}$.

3.2 Tofacitinib citrate

TOFA was detected by reverse-phase liquid chromatography using a Macherey-Nagel Nucleosil 100-5 C18 (4.0 x 250 mm; 5.0 μm particle size) column, kept at 25 °C. The mobile phase consisted of water/acetonitrile/methanol 74:13:13 v/v (each solvent was acidified with 0.1% trifluoroacetic acid) at a flow rate of 1 mL/minutes, and UV detection at $\lambda = 278 \text{ nm}$. Caffeine at 20 $\mu\text{g/mL}$ was used as internal standard and added to each sample (UV detection at $\lambda = 278 \text{ nm}$). Data were collected and analyzed using the software Chromeleon 7 (Thermo Fisher).

The detection limit of TOFA is 10 $\mu\text{g/mL}$.

3.3 Bupivacaine

BUPI was detected by reverse-phase liquid chromatography using a Macherey-Nagel Nucleosil 100-5 C18 (4.0 x 250 mm; 5.0 μm particle size) column, kept at 50 °C. The mobile phase consisted of water/acetonitrile + 0.1% (v/v) trifluoroacetic acid at a flow rate of 1 mL/minutes. The method started with 75% of water, changing to an equal mixture after 15 min. Afterwards, the composition was changed to 99% acetonitrile. After 20 min, the initial composition of the mobile phase was reached. The UV detection was fixed at $\lambda = 220 \text{ nm}$. Lidocaine hydrochloride at 200 $\mu\text{g/mL}$ was used as internal standard and added to each

sample (UV detection at $\lambda = 220$ nm). Data were collected and analyzed using the software Chromeleon 7 (Thermo Fisher).

The detection limit of BUPI is 85 $\mu\text{g/mL}$.

3.4 Rapamycin

RAPA was detected by reverse-phase liquid chromatography using a Macherey-Nagel Nucleosil 100-5 C18 (4.0 x 250 mm; 5.0 μm particle size) column, kept at 50 °C. The mobile phase consisted of water/methanol 10:90 v/v + 0.1% trifluoroacetic acid at a flow rate of 1 mL/minutes. UV detection was fixed at $\lambda = 278$ nm. Ketoconazole at 200 $\mu\text{g/mL}$ was used as internal standard and added to each sample (UV detection at $\lambda = 278$ nm). Data were collected and analyzed using the software Chromeleon 7 (Thermo Fisher).

The detection limit of RAPA is 0.3 $\mu\text{g/mL}$.

4. Bibliography

1. Lazzarini, A. *et al.* Investigation of physico-chemical and catalytic properties of the coating layer of silica-coated iron oxide magnetic nanoparticles. *Journal of Physics and Chemistry of Solids* **153**, 110003 (2021).
2. Kang, Y. S., Subhash Risbud, Rabolt, J. F. & Stroeve, P. Synthesis and Characterization of Nanometer-Size Fe₃O₄ and γ -Fe₂O₃ Particles. *Chem. Mater.* **8**, 2209–2211 (1996).
3. Zhang, S. *et al.* Biocompatible phosphatidylcholine bilayer coated on magnetic nanoparticles and their application in the extraction of several polycyclic aromatic hydrocarbons from environmental water and milk samples. *J Chromatogr A* **1238**, 38–45 (2012).
4. Pereira, D. S. M. *et al.* Magnetoliposomes containing calcium ferrite nanoparticles for applications in breast cancer therapy. *Pharmaceutics* **11**, (2019).
5. Efrat, R., Kesselman, E., Aserin, A., Garti, N. & Danino, D. Solubilization of hydrophobic guest molecules in the monoolein discontinuous QL cubic mesophase and its soft nanoparticles. *Langmuir* **25**, 1316–1326 (2009).
6. Mezzenga, R. *et al.* Shear rheology of lyotropic liquid crystals: A case study. *Langmuir* **21**, 3322–3333 (2005).

Curriculum Vitae

Education

- **PhD in Physical and Chemical Sciences (CHIM/06)**

University of L'Aquila

Expected Graduation Date: May 2024

Project: Lipid-Based Systems: Multifunctional Platforms for Biomedical and Environmental Applications

Tutor: Prof. Luisa Giansanti

- **Master Degree in Chemical Sciences (LM-54)**

University of L'Aquila | 25/07/2020 | 110/110 *cum laude*

Thesis: Levodopa-loaded liposomes as potential drug delivery system for Parkinson's disease

Tutors: Prof. Luisa Giansanti, Prof. María Luisa González Rodríguez

- **Erasmus+ Traineeship**

January 2020 - March 2020

Project: Levodopa-loaded liposomes as potential drug delivery system for Parkinson's disease

Tutor: Prof. María Luisa González Rodríguez

- **Bachelor Degree in Chemistry and Materials Science (L-27)**

University of L'Aquila | 15/12/2018 | 110/110 *cum laude*

Thesis: Synthesis of different surfactants to be included in lipid-based sensors.

Tutors: Prof. Luisa Giansanti, Prof. Armando Carlone

- **High School Diploma in Chemistry and Materials**

ITIS E. Majorana, Avezzano (AQ) | 2015 | 100/100

Activities carried out during the doctoral course

Courses:

- General Microbiology (BIO/19, 6 CFU, 60 h)
- Pharmacology and Clinical Toxicology (BIO/14, 6 CFU, 54 h)

English courses:

- English for Scientific Writing (C1 level, 28 h)
- English speaking class (12 h)

Seminars and Training Courses:

- Introduzione alla valorizzazione dei risultati della ricerca e della proprietà intellettuale/industriale (online, 4 h)
- Brevetti per invenzione e modello di utilità: introduzione e regolamento UnivAQ (online, 6 h)
- Brevetti per invenzione e modello di utilità: approfondimenti sulle modalità di analisi dello stato dell'arte e di redazione della domanda (online, 6 h)
- Tutela del design, della forma, ... (compresi progetti ingegneria civile/architettura) (online, 6 h)
- Tutela del diritto di autore (compreso del sw) (incluso il tema della "proprietà" del diritto oggetto di tutela) (online, 6 h)
- Start-up & spin-off Introduzione e regolamento UnivAQ (online, 6 h)
- Start-up & spin-off: Dalla business idea al business plan (online, 6 h)
- Fondamenti della tecnica GC-MS – PerkinElmer (online, 4 h)
- Fondamenti della tecnica FT-IR – PerkinElmer (online, 4 h)
- Creazione di un metodo con calcoli UV – PerkinElmer (online, 4 h)

- A chemical database designed by chemists – Reaxys (online, 2 h)
- 3D Printing in Pharmaceuticals and Personalized Medicine, online, MDPI, October 5th, 2022
- Reaxys – Training (UnivAQ, 2 h)

Attended Schools:

- VI National School of Chemical Teaching “Giuseppe Del Re” (Online, November 17-30, 2021)
- XIII School of Educational Research and Chemical Teaching “Ulderico Segre” (Online, November 17-30, 2021)
- CHESS 2022, Conventional and High-Energy Spectroscopies for Inorganic, Organic and Biomolecular Surfaces and Interfaces (Online, February 21-25, 2022)

Teaching and Tutoring experiences:

- Grant for a tutoring fellowship for biology students (L-13, University of L’Aquila): Inorganic (75 h) and Organic (75 h) Chemistry
- Thesis Supervisor for bachelor’s and master’s students (Francesca Cerratti, L-27, “Liposomi come ausiliari nella tintura della lana”; Cristiana Palumbo, LM-54, “Applicazione di aggregati lipidici nell’industria tessile”; Francesca Commito, LM-54, “Applicazione di magnetoliposomi per il recupero di farmaci dalle acque reflue”)
- Assistance in educational laboratories (EPC, 12 h; Organic Chemistry, 16 h)

Professional Qualifications: Professional Habilitation in Chemistry, University of Camerino (47/50)

International Experience: Visiting PhD Student at Universität Bern (Bern, Switzerland), September 2022 - March 2023, Tutors: Prof. Dr. Paola Luciani, Dr. Simone Aleandri

Participation in Scientific Conferences with Oral Contributions:

- Novel Liposomes as Levodopa Nanocarriers for the Treatment of Parkinson's Disease (Merck Young Chemists' Symposium 2021, Rimini, November 21-23, 2021)
- Magnetic Liposomes Based on Iron Oxide Nanoparticles for Industrial Applications (First Symposium for YouNg Chemists: Innovation and Sustainability (SYNC2022), Rome, June 20-23, 2022)
- Iron Oxide Magnetic Nanoparticles Coated with Lipid Bilayer as Tools in Waste-water Treatment (XV Italian Conference on Supramolecular Chemistry (SupraMol2022) | Salerno | June 28th - July 1st, 2022)
- Tackling Water Pollution Due to Textile Industry: The Potential of Magnetic Liposomes (6th EuChemS Conference on Green and Sustainable Chemistry, Salerno, 3-6 September, 2023)
- Lipid Mesophases-based Beads as New Platform for Sustained Release of TOFA (Autumn Meeting for Young Chemists in Biomedical Sciences (AMYC-BIOMED), Florence, 16-18 October 2023)

Participation in Scientific Conference with Poster Contribution:

- Optimizing a Wool Dyeing Process Using Different Liposomal Formulations (Interregional Meeting of the Italian Chemical Society – Section Toscana, Umbria, Marche and Abruzzo (TUMA), Perugia, September 1-2, 2022)

Published Articles:

- UV Properties and Loading into Liposomes of Quinoline Derivatives; Sara Battista, Vincenzo Marsicano, Antonio Arcadi, Luciano Galantini, Massimiliano Aschi, Elena Allegritti, Alessandra Del Giudice, Luisa Giansanti, *Colloids and Interfaces* **2021**, 5(2), 28;

- Structurally Related Liposomes Containing *N*-Oxide Surfactants: Physicochemical Properties and Evaluation of Antimicrobial Activity in Combination with Therapeutically Available Antibiotics; Sara Battista, Pierangelo Bellio, Lorenza Fagnani, Elena Allegritti, Lisaurora Nazzicone, Luciano Galantini, Giuseppe Celenza, Luisa Giansanti | *Molecular Pharmaceutics* **2022**, 19 (3), 788-797;
- Organocatalytic Synthesis of γ -Amino Acid Precursors via Masked Acetaldehyde under Micellar Catalysis; Maria Edith Casacchia, Giuliana Giorgianni, Elena Allegritti, Luisa Giansanti, Armando Carlone, Fabio Pesciaioli | *SynOpen* **2023**, 7, 29–32;
- Novel Liposomal Formulations for Protection and Delivery of Levodopa: Structure-properties Correlation; Elena Allegritti, Sara Battista, Maria Anna Maggi, Claudia Marconi, Luciano Galantini, Luisa Giansanti | *International Journal of Pharmaceutics* **2023**, 643, 123230;
- Influence of Lipid Composition on Physicochemical and Antibacterial Properties of Vancomycin-Loaded Nanoscale Liposomes; Sara Battista, Elena Allegritti, Claudia Marconi, Pierangelo Bellio, Luciano Galantini, Alessandra del Giudice, Giuseppe Celenza, Lorenza Fagnani, Luisa Giansanti | *ACS Applied Nano Materials* **2023**, 7 (1), 1348 – 1356;
- Unlocking New Dimensions in Long-acting Injectables Using Lipid Mesophase-based Beads; Elena Allegritti, Luisa Giansanti, Gregor Bordon, Anna Maria Maggi, Paola Luciani, Simone Aleandri | *Journal of Colloid and Interface Science* **2024**, 664, 1031 – 1041

Under-Review Articles:

- Addressing Water Contamination by Exploring the Potential of Magnetic Core-Shell Liposomes and the Role of Their Composition; Elena Allegritti, Cristiana Palumbo, Sara Battista, Franco D’Orazio, Massimiliano Aschi,

Michele Mattera, Barbara Cravello, Luisa Giansanti; under revision on *Journal of Colloid and Interface Science*

- Using Liposomes in a Wool Dyeing Process: A Sustainable Approach; Elena Allegritti, Cristiana Palumbo, Sara Battista, Barbara Cravello, Luisa Giansanti; under revision on *ACS Sustainable Chemistry & Engineering*